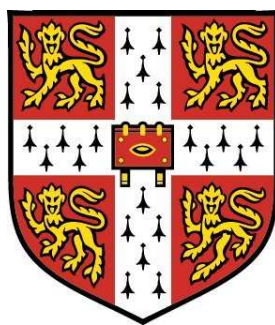


A Lattice Boltzmann Model for Diffusion of Binary
Gas Mixtures



University of Cambridge
Department of Engineering

This dissertation is submitted for the degree of

Doctor of Philosophy

by:

Sam Bennett

King's College

2010

A Lattice Boltzmann Model for Diffusion of Binary Gas Mixtures

Sam Bennett

This thesis describes the development of a Lattice Boltzmann (LB) model for a binary gas mixture. Specifically, channel flow driven by a density gradient with diffusion slip occurring at the wall is studied in depth.

The first part of this thesis sets the foundation for the multi-component model used in the subsequent chapters. Commonly used single component LB methods use a non-physical equation of state, in which the relationship between pressure and density varies according to the scaling used. This is fundamentally unsuitable for extension to multi-component systems containing gases of differing molecular masses that are modelled with the ideal gas equation of state. Also, existing methods for implementing boundary conditions are unsuitable for extending to novel boundary conditions, such as diffusion slip. Therefore, a new single component LB derivation and a new method for implementing boundary conditions are developed, and validated against Poiseuille flow. However, including a physical equation of state reduces stability and time accuracy, leading to longer computational times, compared with ‘incompressible’ LB methods. The new method of analysing LB boundary conditions successfully explains observations from other commonly used schemes, such as the slip velocity associated with ‘bounce-back’.

The new model developed for multi-component gases avoids the pitfalls of some other LB models, a single computational grid is shared by all the species and the diffusivity is independent of the viscosity. The Navier-Stokes equation for the mixture and the Stefan-Maxwell diffusion equation are both recovered by the model. However, the species momentum equations are not recovered correctly and this can lead to instability. Diffusion slip, the non-zero velocity of a gas mixture at a wall parallel to a concentration gradient, is successfully modelled and validated against a simple one-dimensional model for channel flow. To increase the accuracy of the scheme a second order numerical implementation is needed. This can be achieved using a variable transformation method which does not result in an increase in computational time.

Simulations were carried out on hydrogen and water diffusion through a narrow channel, with varying total pressure and concentration gradients. For a given value of the species mass flux ratio, the total pressure gradient was dependent on the species concentration gradients. These results may be applicable to fuel cells where the species mass flux ratio is determined by a chemical reaction and the species have opposing velocities. In this case the total pressure gradient is low and the cross-channel average mass flux of hydrogen is independent of the channel width.

Finally, solutions for a binary Stefan tube problem were investigated, in which the boundary at one end of a channel is permeable to hydrogen but not water. The water has no total mass flux along the channel but circulates due to the slip velocity at the wall. The cross-channel average mass flux of the hydrogen along the channel increases with larger channel widths. A fuel cell using a mixture of gases, one being inert, will experience similar circulation phenomena and, importantly, the width of the pores will affect performance.

This thesis essentially proves the viability of LB models to simulate multi-component gases with diffusion slip boundaries, and identifies the many areas in which improvements could be made.

Declaration

This dissertation is my own work and contains nothing which is the outcome of work done in collaboration with others, except as specified in the text and Acknowledgements. This dissertation contains approximately 31,000 words and 43 figures. This dissertation has not been submitted for a degree or diploma or other qualification at any other University.

Sam Bennett

Hopkinson Laboratory, Cambridge

21st of July, 2010

Acknowledgements

I'm not sure how, or if, I would have completed the work presented in this thesis without two people, Pietro Asinari of Politecnico di Torino and Paul Dellar of the University of Oxford. They both recognised a student out of his depth in the quagmire of Lattice Boltzmann literature and tossed him a lifeline, for which I am profoundly grateful. They invested their time and energy in me and my work, their reward is only this small paragraph. I would also like to thank their respective deputies, Salvador Izquierdo and Tim Reis, for ensuring that every spare moment of my time in Turin and Oxford (and China) was spent eating delicious food and having fun.

Whenever I have needed reminding that there is more to engineering than Chapman-Enskog, Joy Ward and everyone involved in outreach (too numerous to mention) were there; thank you all for cheering me up.

Without Peter Benie coaxing my computer, 'Ortley', through its old age I would never have finished this thesis, thank you for that and a million other small things.

I would like to thank my supervisor and advisor, John Young and Graham Pullan, and also Nick Collings.

Antonios Triantafyllidis, Andy Garmory and Robert Gordon all tried their best to answer my impossible questions, thank you, and stick with the CFD. Cathy Elks kindly pointed out the parts of this thesis which were unnecessarily obfuscated.

Finally I thank Rolls Royce Fuel Cells Ltd. and the EPSRC for their generous financial support in exchange for the very occasional one page report.

Contents

Contents	v
List of Symbols	ix
1 Introduction	1
1.1 Notes on style	3
2 An Introduction to LB Methods	5
2.1 A one-dimensional scheme (D1Q2)	5
2.2 D1Q2 example code	8
2.3 Analysing the D1Q2 scheme	11
2.4 One dimension, three velocity (D1Q3) scheme	12
2.5 Concluding remarks on the 1D examples	14
3 Literature Review	17
3.1 Lattice Boltzmann Methods (LBM)	17
3.1.1 Lattice Boltzmann from the Lattice Gas Automaton	17
3.1.2 The scope of Lattice Boltzmann	19
3.1.3 The rise of Lattice BGK	20
3.1.4 Boundaries for LBM	21
3.1.5 Improvements on LBGK	23
3.1.6 LBM for multi-component fluids	24
3.1.7 LBM in porous media and solid oxide fuel cells	26

3.2	Diffusion slip	27
3.2.1	Origin of diffusion slip	29
4	Single-Component Lattice Boltzmann	32
4.1	The D2Q9 grid and the Boltzmann equation	33
4.1.1	The D2Q9 grid	33
4.1.2	Scaling	34
4.1.3	The truncated nine moment system	35
4.1.4	The scaled evolution equation	37
4.1.5	Moments of the evolution equation	38
4.1.6	The equation of state	39
4.2	The equilibrium distribution	39
4.2.1	Mass conservation	40
4.2.2	Momentum conservation	40
4.2.3	Higher moments	41
4.2.4	Recovering the equilibrium distribution function	42
4.3	The MRT collision operator	43
4.3.1	Evolution of moments	45
4.3.2	The momentum flux density tensor (Π_{XX}, Π_{XY} and Π_{YY})	46
4.3.3	The momentum equation	48
4.4	Conclusions	51
5	Boundary Conditions and Numerical Implementation	52
5.1	Boundary conditions for LB	52
5.1.1	Kinetic style boundaries	52
5.1.2	Moment grouping	53
5.1.3	Analysis of Zou and He boundary conditions	55
5.1.4	Analysis of ‘bounce-back’, specular and diffusive boundary conditions	58
5.1.5	Treatment of corner nodes	60

5.2	Numerical implementation	62
6	Solution of Poiseuille Flow	66
6.1	Theoretical solution	66
6.1.1	Moment based boundary conditions for Poiseuille Flow	68
6.2	Non-dimensional results for Poiseuille flow	71
6.2.1	Higher moment relaxation frequencies	76
6.3	A dimensional problem	76
6.4	Conclusions	78
7	LB for Multi-Component Gases	80
7.1	Multi-component nomenclature	81
7.2	Binary channel flow theory	81
7.3	Multi-component Lattice Boltzmann scheme	84
7.4	Mass conservation equation	85
7.5	Momentum equation	86
7.5.1	Mixture Centred Equilibrium (MCE)	87
7.5.2	Species Centred Equilibrium (SCE)	90
7.5.3	Corrected Species Centred Equilibrium (CSCE)	92
7.6	Expressions for diffusion slip	93
7.6.1	Implementing diffusion slip in the LB method	94
7.6.2	Intersections between walls and open boundaries	96
7.7	Modified relaxation times	98
7.8	Self-diffusion test case	98
7.9	A dimensional test case	104
7.9.1	Alternative boundary conditions	107
7.10	Conclusions	109
8	Improvements to Multi-component Methods	110
8.1	Second order scheme	110

8.1.1	Crank-Nicolson integration	110
8.1.2	Diffusion slip boundary	112
8.1.3	Other boundaries	114
8.1.4	Intersection between a wall and another boundary	115
8.1.5	Binary channel flow results	117
8.2	Pre-conditioning	117
8.3	Conclusions	120
9	Calculations of Binary Flow	121
9.1	Fully developed binary channel flow	122
9.2	Binary flow with one inert component	130
9.2.1	The Stefan tube problem	130
9.2.2	A LB model of a Stefan tube type problem	131
9.2.3	The effect of channel width	136
9.3	Conclusions	139
10	Conclusions	141
10.1	Summary of results from this work	141
10.2	Suggestions for future research	143
	References	146

List of Symbols

The page on which the following symbols are first used is listed.

A	4	H	68	M_σ	28	ς	4
\mathbf{A}	111	i	4	m_σ	82	$S(M_\sigma)$	93
α	4	k	89	n_σ	28	t	6
B	4	κ_σ	95	ν	50	t_f	34
β	4	$\ddot{\kappa}_\sigma$	113	N_x	105	Θ_σ	97
$B_{\sigma,\varsigma}$	82	L	34	Ω	7	$\ddot{\Theta}_\sigma$	116
c	33	λ	7	p	13	U	34
$D_{\sigma,\varsigma}$	28	$\mathbf{\Lambda}$	44	Φ_σ	112	u	6
e	11	λ^δ	86	Π	36	\ddot{u}	111
ϵ_{Kn}	35	λ^ν	44	ρ	6	x	4
ϵ_{Ma}	35	λ^ξ	44	ρ_0	35	ξ	50
f	6	M	81	RT	39	X_σ	81
g_σ	111	m	6	R_0	81	y	4
γ	118	\mathbf{M}	6	σ	4	Y_σ	81

Chapter 1

Introduction

Solid Oxide Fuel Cells (SOFCs) are being developed by Rolls Royce Fuel Cells, with the hope that they will replace gas turbines in stationary power applications. The study of fuel cells involves many engineering problems which are not yet well understood, one of which is the diffusion of the fuel through the electrodes of the cell. The porous electrodes have irregular geometries, and currently no satisfactory method exists for modelling the gas flow through them. This work is the first step towards developing a Lattice Boltzmann (LB) model suitable for that task.

The origin of the Lattice Boltzmann method is the work in the 19th century by Maxwell and Boltzmann on the kinetic theory of gases. The first success of the kinetic theory was Maxwell's prediction that the viscosity of a gas was independent of its density, which was later experimentally confirmed. Chapman and Enskog, working independently in 1916, obtained a class of slowly varying or 'normal' solutions (see Grad (1963)) to the Boltzmann equation and found expressions for the transport coefficients which again showed good agreement with experiments. The work of Bhatnagar, Gross and Krook significantly simplified the Boltzmann Equation, yet key results could still be obtained with sufficient accuracy. However most of kinetic theory remains unconfirmed, as measurements of the velocity of individual molecules of a gas are currently infeasible. It is also a subject which is particularly labour intensive to study, Chapman reportedly described reading his own

book as ‘like chewing glass’ (According to Brush (1976) citing the Observer newspaper from 1957).

The concept that lies behind Lattice Boltzmann (and before that the Lattice Gas Automaton) is to store the velocity of every particle that makes up a gas, and track the particles as they collide with each other. Of course, to store every particle would be far too computationally expensive, and so simplifications are made. This is where the two ideologies of Lattice Boltzmann split. On the one hand, efforts can be made to ensure the computational particles behave as closely as possible to the behaviour predicted by the kinetic theory. On the other hand, the particle’s behaviour is not of concern, as long as the behaviour of certain averages (called ‘moments’) such as density and momentum agree with the results from kinetic theory. Both viewpoints have merit, but they often get confused and mixed together, as the discussions on boundary conditions in Section 5.1.1 and mixture collision integrals in Section 3.1.6 will show. This work considers only the behaviour of the moments, and the particles in the computational scheme do not behave like real particles. An introduction to the way Lattice Boltzmann models are constructed is given in Chapter 2, and then a review of the Lattice Boltzmann literature relevant to this work is in Chapter 3.

Aside from Lattice Boltzmann this work also covers the implementation of a diffusive slip boundary condition for a binary gas mixture. Diffusion slip has an interesting history, but one which has mostly been ignored. There is a very simple reason for this, in most applications diffusion slip itself can be safely ignored. However in fuel cells and some other applications this is not the case as the flow through the porous material is driven by concentration gradients not total pressure gradients, and diffusion slip becomes a key factor. The story of diffusion slip, and some more details about its kinetic origin, are in Chapter 3.

The main difficulty in extending the standard Lattice Boltzmann model to multi-component gas mixtures is the non-physical equation of state commonly used. Therefore, in Chapter 4, a model for a compressible single component fluid with a barotropic equation of state is developed. This method can easily be extended to gas mixtures, but is not the

most efficient tool for single component gases. The boundary conditions commonly used are based on specifying the behaviour of the particles, and not the moments. However, for diffusion slip boundary conditions to be implemented a set of conditions on the moments must be imposed. Therefore, a general new approach to boundaries is conceived in Chapter 5. This approach is not specific to any problem and represents a significant shift in the way boundary conditions for Lattice Boltzmann are considered, and sheds new light on established boundary condition methods. Both the new equation of state and new boundary treatment are validated in Chapter 6 by simulating Poiseuille flow through a channel.

The extension to multi-component gases, building on the foundations of the preceding chapters, is described in Chapter 7. A key capability of the model developed is the separation of diffusive and viscous effects, allowing flow with any Schmidt number (the ratio of viscous diffusion to mass diffusion, $\nu/D_{\sigma,\varsigma}$) to be modelled. Diffusive slip boundary conditions are developed, and binary channel flow is simulated and validated against a simple one-dimensional scheme for solving the macroscopic flow equations. To obtain accurate results in reasonable computational time improvements to the numerical scheme are required, as described in Chapter 8.

Finally, in Chapter 9 two binary problems are investigated, channel flow and the Stefan tube, and some interesting behaviour of binary gases is revealed. These problems highlight the capability of the method and its potential future applications.

1.1 Notes on style

The principle complaint amongst engineers reading the LB literature is the use of non-dimensional variables. In this work there are two scales by which variables may be non-dimensionalised, indicated with a $\tilde{}$ or a $\hat{}$ over the variable. However, for clarity in Chapters 2 and 5 the $\tilde{}$ is dropped, so that a variable without a $\tilde{}$ in those chapters is assumed to be non-dimensional.

Another feature common to LBM is the use of the momentum flux density tensor,

following the approach of Landau and Lifshitz (1959). The symbol Π is used for all moments of the velocity distribution function \mathbf{f} , see Section 4.1.3. $\Pi_{\alpha\beta}$ (i.e. Π with two subscripts) is the momentum flux density tensor, and consists of the second order moments of \mathbf{f} . The momentum flux density tensor is composed of its equilibrium values minus the viscous stress tensor. In this work the viscous stress tensor is $-\Pi_{\alpha\beta}^{(neq)}$, and so $\Pi_{\alpha\beta} = \Pi_{\alpha\beta}^{(eq)} + \Pi_{\alpha\beta}^{(neq)}$.

The subscript i indicates an element of a vector. For example f_i is element number i of \mathbf{f} where the use of bold font indicates a vector. Matrices are represented by the use of a bold capital letter, for example \mathbf{M} .

The subscript σ is used to identify any species in a mixture, then ς identifies the other species. These are replaced by the subscripts A and B when the expression would not be true for any species, but applies only to specific species.

Similarly, the subscript α represents any Cartesian direction, and β represents the other direction. All examples are two dimensional. The subscripts x and y are used when referring to a direction in particular.

The superscript (eq) is used to indicate the variable is evaluated at equilibrium, the superscript (neq) indicates the non-equilibrium component of that value, for example $f^{(neq)} = f - f^{(eq)}$.

The superscript \dagger is used to indicate a variable after the collision step, while the superscript $+$ indicates a variable after the collision and streaming step.

The \prime superscript indicates that the value of the variable has been corrected to include certain numerical effects, as described in Section 5.2. The γ superscript indicates the variables used in conjunction with pre-conditioning, described in Section 8.2. The $*$ superscript is used to describe multi-component collision operators in Section 3.1.6, and is not used again.

Double dots, like \ddot{g} , indicate a variable derived from the variable g , introduced and explained in Chapter 8.

Chapter 2

An Introduction to LB Methods

This section is intended as an introduction to general LB methods. In order to keep the chapter concise the example chosen is particularly basic. The solution to a one-dimensional problem will be examined, a fluid subject to a ‘square wave’ initial density profile in an infinite domain. As time progresses the fluid in the region of initially high density disperses, until the density of the fluid everywhere is the same and the velocity is zero. A periodic problem was chosen so that boundary conditions need not be considered.

For ease of explanation all variables in this chapter are non-dimensional.

2.1 A one-dimensional scheme (D1Q2)

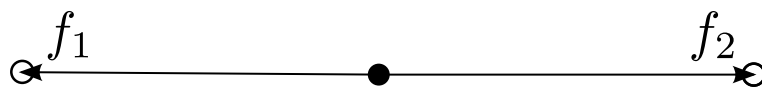


Figure 2.1: The D1Q2 grid. The arrows show the velocities associated with each element of f .

If the variables of interest are the density and velocity of the fluid, at least two values must be stored at each grid point. To use a LB method the situation can be considered in this way: At any grid point let the mass of particles per unit volume having unit velocity to the left be f_1 and the mass of particles per unit volume having unit velocity to the

right be f_2 . Then, the mass density is $(f_1 + f_2)$ and the net mass flux to the right is $(f_2 - f_1)$. If an equal number of particles are travelling in each direction then the net mass flux (equivalently, momentum) is zero. The mass density of particles is represented as the variable $\mathbf{f}(i, x, t)$, where i is a directional index, in this example $i = 1$ points left and $i = 2$ points right as shown in Figure 2.1. x is the spatial position of the node and t is time. At each grid point the particle mass density can be expressed in vector form, and a vector of the macroscopic variables, \mathbf{m} , is defined as,

$$\mathbf{f}^{D1Q2} = \begin{bmatrix} f_1 \\ f_2 \end{bmatrix} \quad \mathbf{m}^{D1Q2} = \begin{bmatrix} \rho \\ \rho u \end{bmatrix} \quad (2.1)$$

where the subscript of the scalar f is the directional index i . The mass density is ρ and the macroscopic net velocity is u . The shorthand ‘DaQb’ is used for describing a Lattice Boltzmann scheme, where ‘a’ is the number of dimensions and ‘b’ is the number of discrete velocities. The vector \mathbf{m} contains the moments (weighted summation) of \mathbf{f} , and this relationship can be expressed mathematically using a transform matrix, \mathbf{M} , as follows,

$$\mathbf{m}^{D1Q2} = \begin{bmatrix} 1 & 1 \\ -1 & 1 \end{bmatrix} \begin{bmatrix} f_1 \\ f_2 \end{bmatrix} = \mathbf{M}^{D1Q2} \mathbf{f}^{D1Q2} \quad (2.2)$$

There are two different bases in which information about the fluid can be expressed. The ‘moment’ basis contains quantities which are weighted functions of the particle f values, whereas the ‘particle’ basis (or the ‘ f ’ values) contains values for the mass of particles travelling in each direction. Clearly the particle basis is well suited to computation, whereas the problem is defined in terms of the moment basis. Switching between the two is the key concept in analysing LBM.

Having defined the representation of the fluid in terms of the two populations at each grid point, the unsteady behaviour of the fluid will now be examined. Each time step is split into two distinct processes, namely *streaming* and *collisions*. The streaming process will involve all the population’s (the ‘ f ’ values) moving to the next grid space in the direction of

that population's discrete velocity. Each node will effectively swap populations with each of its nearest neighbours. This is the principle method of communicating disturbances through the grid, and the speed of these exchanges must be much higher than the bulk velocity of the fluid. After the streaming is completed, there is a local collision step. This may be thought of as those particles arriving at each grid point physically colliding, and exchanging momentum, with each other. In fluid dynamics problems the total mass at each grid point must be conserved during the collision step. The modelling of this collision step is vital in ensuring the correct macroscopic behaviour.

Before modelling the collision step an equilibrium solution must be considered. Equilibrium occurs when the spatial gradients of velocity are zero; in this specific case that will be when there is zero velocity everywhere. Equilibrium values for the populations for each discrete velocity in terms of an equilibrium density may be defined, using Equation 2.2, as,

$$\mathbf{f}^{(D1Q2,eq)} = (\mathbf{M}^{D1Q2})^{-1} \begin{bmatrix} \rho^{(eq)} \\ 0 \end{bmatrix} = \begin{bmatrix} \frac{\rho^{(eq)}}{2} \\ \frac{\rho^{(eq)}}{2} \end{bmatrix} \quad (2.3)$$

To model the collision process, a linear relaxation to the equilibrium state is used. That is to say that when the particles from neighbouring sites collide, they do so in such a way as to move closer to an equilibrium state. The rate at which this relaxation occurs is controlled by a parameter λ . The model for this relaxation process is taken from the Bhatnagar-Gross-Krook (BGK) [Bhatnagar et al. (1954)] equation commonly used in continuum kinetic methods. The BGK equation states that, in a collision, particles within a population all having the same velocity leave that population at a rate proportional to the current population, whereas those particles entering that population do so at a rate proportional to the equilibrium value of that population. The collision term is written as $\Omega(f)$ and the post collision state as \mathbf{f}^\dagger .

$$\mathbf{f}^{D1Q2,\dagger} = \mathbf{f}^{D1Q2} + \Omega(\mathbf{f}) = \mathbf{f}^{D1Q2} + \lambda(\mathbf{f}^{D1Q2,eq} - \mathbf{f}^{D1Q2}) \quad (2.4)$$

Remembering that the density is defined as the sum of the elements of \mathbf{f}^{D1Q2} , the vectors

in the previous equation may be summed over their elements to give,

$$\rho^\dagger = \rho + \lambda(\rho^{eq} - \rho) \quad (2.5)$$

It has already been specified that the collision process must conserve mass and so $\rho^\dagger = \rho$. Therefore $\rho^{eq} = \rho$. Equivalently $\sum_i \Omega(f)_i = 0$.

2.2 D1Q2 example code

The MATLAB code for the D1Q2 example outlined above is included here. Initial, and arbitrary, values are defined as follows:

```
nx=31; %number of grid points
nt=30; %number of time steps

M = [1,1;-1,1];

lambda =1/3;%This controls the rate of relaxation

%initialise values of f
for x=1:round(nx/3)
    f(1,x,1)=0.5;
    f(2,x,1)=0.5;
end
for x=(round(nx/3)+1):(round(2*nx/3)-1)
    f(1,x,1)=1;
    f(2,x,1)=1;
end
for x=round(2*nx/3):nx
    f(1,x,1)=0.5;
```

```

    f(2,x,1)=0.5;
end

```

The collision and stream rules are applied at every time step. At each collision step the density is calculated from the existing fluid populations, then the equilibrium function is calculated using this density. Finally the f values are relaxed towards equilibrium. The stream step moves the f values to the nearest neighbour, but also moves them to the next time step, to save a separate copy operation. The node points at each end must be dealt with separately, and a periodic condition has been enforced in this particular example for simplicity.

```

for t=1:nt
%Collide
for x=1:nx
    rho(x) = f(1,x,t)+f(2,x,t);
    feq(:,x) = [0.5*rho(x), 0.5*rho(x)];
    f(:,x,t)=f(:,x,t)+lambda.*(feq(:,x)-f(:,x,t));
end
%stream
for x=2:nx
    f(1,x-1,t+1)=f(1,x,t);
end
for x=1:(nx-1)
    f(2,x+1,t+1)=f(2,x,t);
end
%periodic boundary
f(2,1,t+1)=f(2,nx,t);
f(1,nx,t+1)=f(1,1,t);
end

```

The results of this calculation, the density and velocity, are shown in Figure 2.2. The behaviour is not as expected from a viscous fluid. The total fluid in the domain, the sum over the nodes of the density remains constant over time at 41 non-dimensional units. The scheme therefore conserves mass. However, there is no reduction in the magnitude of the peak velocity of the fluid, and even over much larger time intervals the peak velocity remains the same so that no steady-state is reached. Therefore, it appears that the viscous behaviour of the fluid is not correctly modelled, a conclusion which is supported by the analysis in the subsequent section.

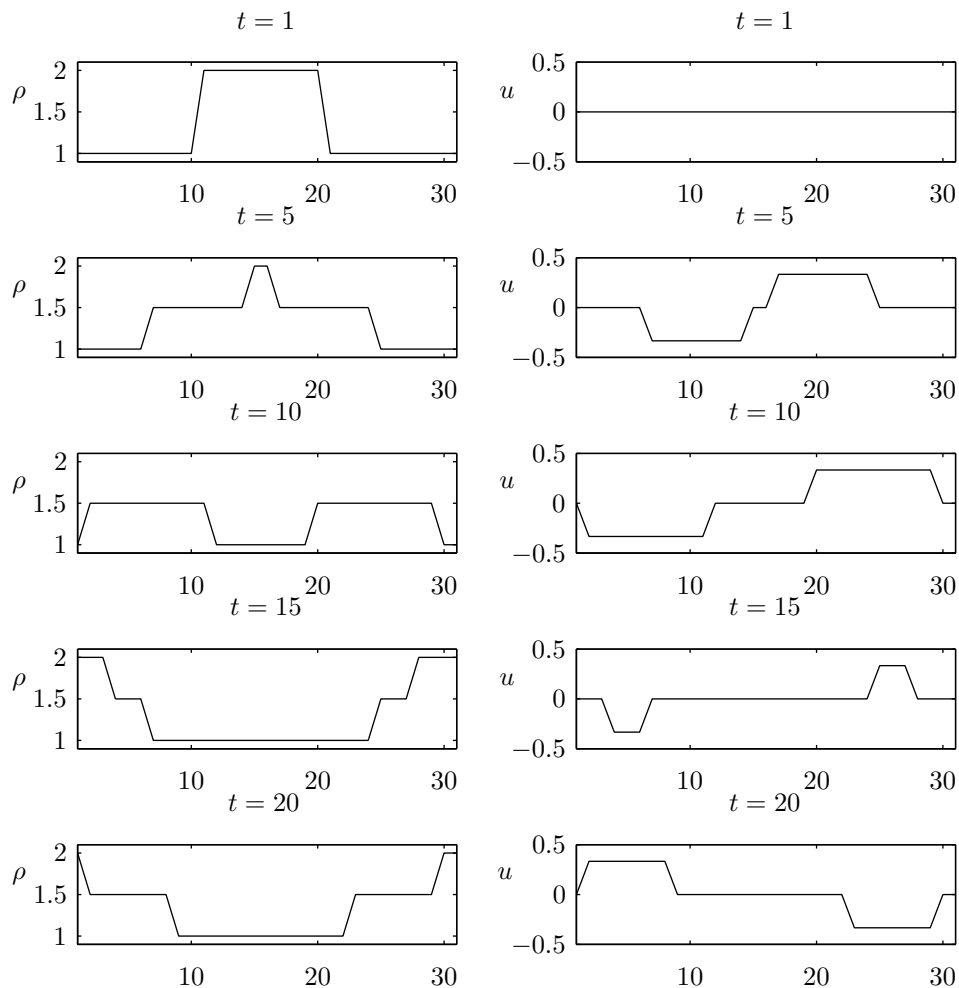


Figure 2.2: Density and velocity profiles at different time steps for D1Q2 example. Periodic boundary conditions were used. Non-dimensional units.

2.3 Analysing the D1Q2 scheme

An analytical expression for the system outlined above is now developed. Combining the streaming and collision step yields an update equation:

$$f_i^{D1Q2}(x + e_i^{D1Q2}, t + 1) = f_i^{D1Q2}(x, t) + \lambda(f_i^{D1Q2,eq}(x, t) - f_i^{D1Q2}(x, t)) \quad (2.6)$$

Where e_i^{D1Q2} is introduced to represent the velocity with which f_i^{D1Q2} streams. Each element moves one grid space per time step, and in this example $e^{D1Q2} = [-1 \ 1]^T$. A truncated Taylor expansion,

$$f_i^{D1Q2}(x + e_i^{D1Q2}, t + 1) = f_i^{D1Q2}(x, t) + \frac{\partial f_i^{D1Q2}}{\partial t} + e_i^{D1Q2} \frac{\partial f_i^{D1Q2}}{\partial x} \quad (2.7)$$

is used to transform Equation 2.6 into a partial differential equation,

$$\frac{\partial f_i^{D1Q2}}{\partial t} + e_i^{D1Q2} \frac{\partial f_i^{D1Q2}}{\partial x} = \lambda(f_i^{D1Q2,eq} - f_i^{D1Q2}) \quad (2.8)$$

Only the first order terms in the Taylor expansion have been included, and there is an error associated with this, but for this simple example this is ignored.

Summing the elements of the vectors in this equation, noting that $\sum_i e_i f_i = \rho u$, gives,

$$\frac{\partial \rho}{\partial t} + \frac{\partial(\rho u)}{\partial x} = \lambda(\rho - \rho) = 0 \quad (2.9)$$

This is the mass conservation equation. Multiplying Equation (2.8) by e_i^{D1Q2} and summing the vector elements, noting $\sum_i e_i^{D1Q2} e_i^{D1Q2} f_i^{D1Q2} = \rho$, yields,

$$\frac{\partial(\rho u)}{\partial t} + \frac{\partial \rho}{\partial x} = \lambda(\rho^{eq} u^{eq} - \rho u) = -\lambda \rho u \quad (2.10)$$

It is now clear that this simple scheme does not recover the correct momentum equation. It is worth exploring the reasons for this. The initial restriction of only two discrete velocities means that there can be only two meaningful macroscopic variables per grid space. The

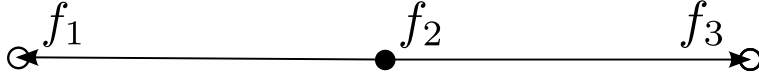


Figure 2.3: The D1Q3 grid. The velocity of the particles associated with f_2 is zero.

momentum equation requires a third macroscopic quantity, the momentum flux density. Therefore, the error in the left hand side of the momentum equation can be attributed to having too few lattice velocities. The error on the right hand side of the momentum equation is due to the choice of using a BGK style collision model and the choice of $f^{(eq)}$. There are an infinite number of ways of modelling the collision process, and each one will give different macroscopic equations. If the collision process were no longer local to each grid node it would be possible to compute the derivatives of the macroscopic variables and perhaps recover the correct momentum equation. However this would sacrifice the simplicity of the current code, and move towards a scheme which is more representative of traditional CFD methods.

2.4 One dimension, three velocity (D1Q3) scheme

To recover the correct momentum equation from the scheme, whilst keeping a local collision operator, another particle velocity is introduced, in this case a population with zero velocity as shown in Figure 2.3. The velocity vector becomes $\mathbf{e}^{D1Q3} = [-1 \ 0 \ 1]^T$, and the transform matrix is,

$$\mathbf{M}^{D1Q3} = \begin{bmatrix} 1 & 1 & 1 \\ -1 & 0 & 1 \\ 1 & 0 & 1 \end{bmatrix} \quad (2.11)$$

The new third moment was selected following the general structure that each row of M is \mathbf{e} transposed with each element raised to the power of the row number minus one. For example row 3 is $[(-1)^2 \ (0)^2 \ (1)^2]$. This approach is in keeping with traditional kinetic theory, however there are different strategies for generating moment bases based on orthogonalisation. Any third moment that is linearly independent of the first two

is acceptable. However, the choice made here reduces the algebraic complexity of what follows. The new moment vector is,

$$\mathbf{m}^{D1Q3} = \begin{bmatrix} \rho \\ \rho u \\ \Pi_{XX} \end{bmatrix} \quad (2.12)$$

Where Π_{XX} is the momentum flux in the x direction. The equilibrium state is

$$\mathbf{m}^{D1Q3,eq} = \begin{bmatrix} \rho \\ \rho u \\ p + \rho u^2 \end{bmatrix} \quad (2.13)$$

where the Euler equation was used to provide a value for Π_{XX} at equilibrium, and p is the pressure of the gas. An equation of state is now required. For simplicity this is taken to be $p = 1/3\rho$. The issue of equations of state will be discussed in considerable length later on, and it is unhelpful to burden this introduction with that discussion.

Using the same technique described in Section 2.3 the same mass conservation equation is recovered, however there is a different momentum equation,

$$\frac{\partial(\rho u)}{\partial t} + \frac{\partial \Pi_{XX}}{\partial x} = \lambda(\rho^{eq} u^{eq} - \rho u) = 0 \quad (2.14)$$

The value for Π_{XX} is unknown, and so the final independent equation in the moment basis is used, which may be obtained by multiplying the $D1Q3$ version of Equation (2.8) by $e_i^{D1Q3} e_i^{D1Q3}$ and summing over i .

$$\frac{\partial \Pi_{XX}}{\partial t} + \frac{\partial(\rho u)}{\partial x} = \lambda(\Pi_{xx}^{(eq)} - \Pi_{XX}) \quad (2.15)$$

Where the fact that the magnitudes of the e_i^{D1Q3} are either unity or zero has been used to give the result $(e_i^{D1Q3})^3 = e_i^{D1Q3}$. The approximation that must be employed to arrive at an expression for Π_{XX} is that it is not too far from its equilibrium value. Therefore the

terms on the left hand side of Equation (2.15) may be given their equilibrium values,

$$\frac{\partial(p + \rho u^2)}{\partial t} + \frac{\partial(\rho u)}{\partial x} = \lambda(p + \rho u^2 - \Pi_{XX}) \quad (2.16)$$

Using the mass continuity equation, 2.9, the equation of state ($p = \rho/3$) and the fact that at equilibrium $\partial(\rho u)/\partial t = -\partial(p + \rho u^2)/\partial x$, after some manipulation the expression for the momentum flux in the x direction becomes,

$$\Pi_{XX} = p + \rho u^2 - \frac{2}{3\lambda}\rho \frac{\partial u}{\partial x} \quad (2.17)$$

For details of exactly how this is reached, consult Dellar (2002b). It is only when the equation of state $p = \rho/3$ is used that such a simple expression is obtained. Inserting this expression into Equation (2.14) yields,

$$\frac{\partial(\rho u)}{\partial t} + \frac{\partial(\rho u^2)}{\partial x} = -\frac{\partial p}{\partial x} + \frac{\partial}{\partial x} \left(\frac{2\rho}{3\lambda} \frac{\partial u}{\partial x} \right) \quad (2.18)$$

which is the compressible one-dimensional Navier-Stokes equation with the viscosity given by $\nu = \lambda/3$. Graphs of the same problem solved with D1Q2 are shown in Figure 2.4. The D1Q3 results show the peak velocity decreasing after 20 time step, and this should be compared with the results from the D1Q2 model. The scheme reaches a steady state with zero velocity and a constant density, as would be expected.

2.5 Concluding remarks on the 1D examples

A relatively simple code, D1Q2, was developed and although there are problems with the momentum equation it is remarkable that the mass conservation equation is recovered. Such a model could be used to model the transport of a passive scalar in an established flow field. The introduction of one extra velocity was sufficient to solve the problem with the correct momentum equation.

The one-dimensional code will now be abandoned in favour of a two-dimensional scheme

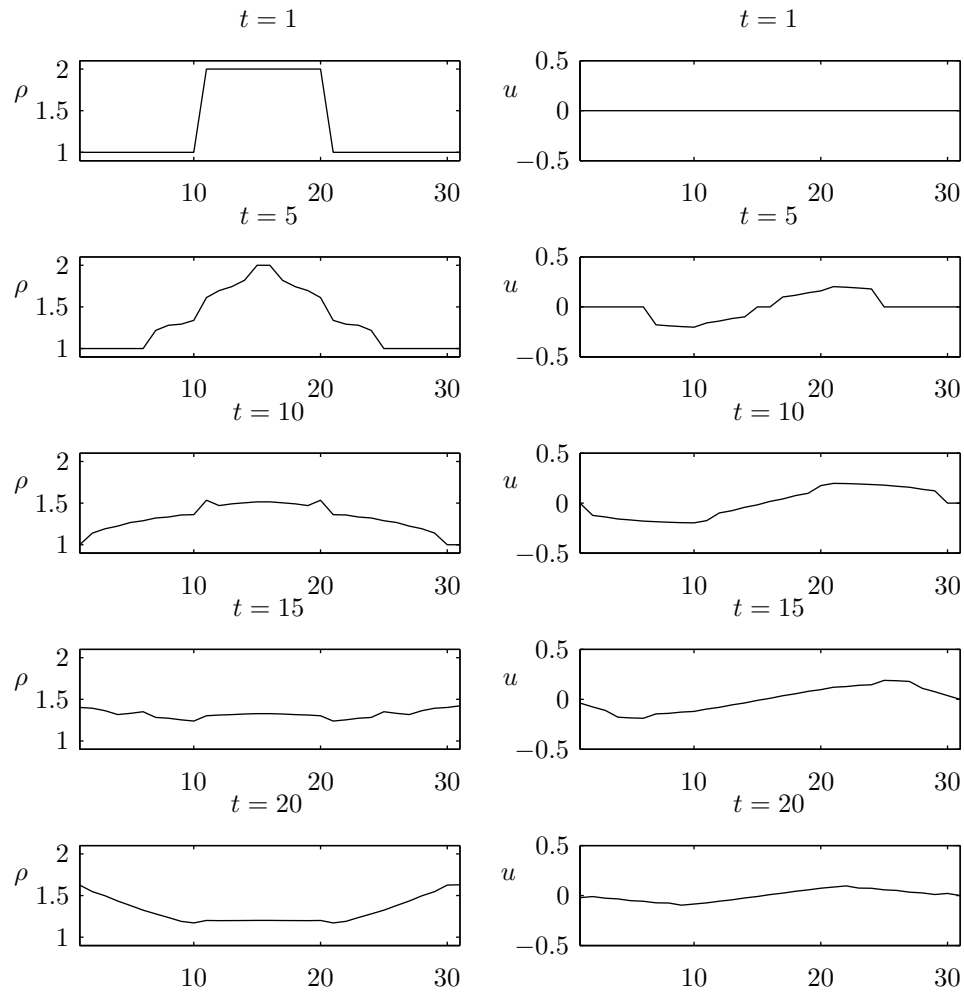


Figure 2.4: Density and velocity profiles at different time steps with the D1Q3 model. Periodic boundary conditions were used. Non-dimensional units.

with nine velocities. However, the method that will be used is based on the same principles as the one-dimensional method developed here. By choosing the moment system wisely the macroscopic equations will appear in conservation form, as they did in the example above. With nine velocities per grid node it will be shown that the correct momentum equation in two dimensions can be recovered, but not the energy equation.

Chapter 3

Literature Review

This chapter contains a review of the literature on the Lattice Boltzmann method and the phenomenon of diffusive slip. With a topic as broad as Lattice Boltzmann even the most extensive literature review would not be comprehensive, and hence only selected topics have been examined. The literature review on diffusive slip is more comprehensive, however, because the subject has not been so extensively researched.

3.1 Lattice Boltzmann Methods (LBM)

3.1.1 Lattice Boltzmann from the Lattice Gas Automaton

A search for ‘Lattice Boltzmann’ on the ‘Web of Knowledge’ journal search engine returns 4,941 results, an indication of the size of the following that LBM has enjoyed in recent years. The earliest entries date back to 1989, when LBM emerged from the Lattice Gas Cellular Automaton (LGCA or LGA) computational scheme. The intention of both methods was to model the behaviour of individual particles, and thus model the macroscopic behaviour of a collection of particles. In the LGA the domain was split into nodes, each of which had a population of particles moving with its own discrete velocities. The key difference between this and LBM is that the number of particles at each node with a certain velocity is either one or zero; in LBM this could be any real number. The LGA was computationally

intensive, and the LB method is better suited to the architecture of most computers as the local collision step may be easily parallelised. For problems where the Navier-Stokes equations are not applicable, for example in the study of rarefied gas flow, there was no established computational method. Since then, both LBM and Monte Carlo methods have been developed.

The earliest review of LBM was conducted by Succi et al. (1991) and it is worthwhile examining his work in some depth as it lays the foundation for many misconceptions that follow. The description of the Lattice Boltzmann Equation (LBE) begins, ‘*The LBE is a nonlinear finite difference equation (even though it does not result from the discretisation of any partial differential equation!)*’. This is interesting as almost exactly the same method is presented as the discretisation of the continuous Bhatnagar Gross Krook (BGK) equation, Bhatnagar et al. (1954), in later work.

The Succi paper described a Lattice Boltzmann method which will not be examined here as it has since been superseded. Results were then presented for laminar flow through porous material, bifurcations of a two-dimensional Poiseuille flow and fully developed two-dimensional forced turbulence. This general approach, presenting a model with very complicated and specific applications, is common in the LBM literature. The scope of papers generally far exceeds their depth. In the results presented by Succi for the flow through a porous material there are several immediate problems. The pressure force is applied to each grid site, meaning that a region of fluid almost entirely encircled by impermeable material will have a high velocity. The boundaries are not examined in depth. A reader more experienced in traditional computational fluid dynamics techniques would be left wondering what time steps and grid spacing were used, how the method converged and whether it was stable. Instead, what Succi presents is a series of particular cases where the results look qualitatively impressive.

Most of the early work on LBM was dedicated to finding model expressions for the collision term. As seen in Chapter 2, the collision term is essential in determining which macroscopic equations the scheme describes. A particularly interesting paper on this subject is that of Chen et al. (1992). They correctly identified that if one has an LB model

with only one speed (not one velocity), an increase in the density of the fluid is equivalent to an increase in the momentum flux (in Chapter 2 in the D1Q2 model $\sum_i e_i e_i f_i = \sum_i f_i$). Therefore there must be at least one population having a velocity with a different speed, the simplest being a zero velocity population. Unfortunately, the authors chose to cloud the solution to this simple mathematical problem with talk of a ‘particle reservoir’. The simplest form of the collision integral was used, a linear relaxation to equilibrium,

$$\Omega(f_i) = -\lambda(f_i - f_i^{(eq)}) \quad (3.1)$$

It should be noted that Ω_i is a general expression for the collision integral, such that $\mathbf{f}^+ = \mathbf{f} + \Omega(\mathbf{f})$. A general expression for the equilibrium distribution was also given, and then constants within that expression were derived by consideration of mass and momentum conservation, and by the correct form of the three viscous stress components. This approach is misleading however, because the form of the general expression had already imposed some symmetry constraints which were not explicitly mentioned. Finally, they noted that there was still one degree of freedom in the definition of the equilibrium function and so an arbitrary constraint was introduced. Nevertheless, the algorithm they described is still widely used today in an essentially unchanged form.

3.1.2 The scope of Lattice Boltzmann

LBM, trading on its computational simplicity and stability, has been applied to a bewildering array of problems: magnetohydrodynamics, immiscible fluids, compressible fluids, incompressible fluids, nonlinear reaction-diffusion equations, thermo-hydrodynamics, non-Newtonian flow, multi-phase, multi-components and short-time motion of colloidal particles had all received the Lattice Boltzmann treatment as early as 1993. Although obviously very different from each other, these papers shared a common theme, the use of LBM as a substitution for the Navier-Stokes or similar equations, with some extra physics bolted on. It is possible that this work does quickly, and in some cases successfully, simulate these complex phenomena, which traditional CFD struggles to do, but it is beyond the scope of

the present work to study all the attempts in detail. The results of the multi-component models are examined, however, particularly because the early models do not recover the correct physics.

3.1.3 The rise of Lattice BGK

The most popular LBM ‘starter’ paper is that of Chen and Doolen (1998), with an astounding 1,501 (as of July 2010) citations. This paper defines the ‘second generation’ of LBM, abandoning the derivation from the lattice cellular automaton and instead rewriting the history of LBM as a discretisation of the continuous BGK model. The two-dimensional nine-velocity model (called D2Q9) is the standard model. The Lattice Boltzmann equation became the now common Lattice BGK (LBGK) equation,

$$f_i(\alpha + e_{\alpha,i}, \beta + e_{\beta,i}, t + 1) = f_i(\alpha, \beta, t) - \lambda[f_i(\alpha, \beta, t) - f_i^{(eq)}(\alpha, \beta, t)] \quad (3.2)$$

The equilibrium function which was previously so carefully constructed is now the continuous Maxwellian distribution confined to the discrete velocity set using a Gauss-Hermite quadrature. This change in derivation surprisingly does not lead to a significant change in the value of the equilibrium function itself. Essentially, although the method has not changed the interpretation is quite different and this is a dangerous step. It is no longer clear that the method has evolved from considerations of the conservation of mass and momentum in terms of macroscopic variables and, instead, it is viewed as being derived purely from microscopic considerations.

The early papers of He and Luo (1997b,c,a) strongly supported the LBGK philosophy, although Luo’s later papers highlighted shortcomings of the method, Luo (2004). More recently he has turned to the Multiple Relaxation Time (MRT) model, see Lallemand and Luo (2000). However, the damage had already been done in establishing the microscopic interpretation of LBGK. Not that this was the fault of Luo, rather the lax referencing of his early papers by other authors. Succi et al. (2002) reviewed LBGK in the context of other microscopic lattice based methods.

Because of this implied microscopic nature of LBGK, efforts have been made to uncover behaviour beyond Navier-Stokes, especially in micro-channel flow. Verhaeghe et al. (2009) proved that all the attempts beforehand, and they listed 15 such papers, have been exercises more in curve fitting than modelling the physics. They modelled Navier-Stokes flow with Knudsen velocity slip at the wall. In order to enforce this slip they used an approach mathematically similar to the approach in this work, but the explanation is confused by the unnecessary use of microscopic boundaries, as will be discussed in Chapter 5.

This thesis, building on the work of Asinari and Ohwada (2009), hopefully puts beyond doubt the fact that with a two-dimensional nine-velocity LBGK method it is not possible to recover the rarefied gas equations beyond the Navier-Stokes level.

3.1.4 Boundaries for LBM

The confusion about the microscopic or macroscopic nature of LBM has probably had the biggest impact on boundary conditions, a subject in which there is a lack of good quality work. By far the most common approach to modelling solid-fluid boundaries is the so-called ‘bounce-back’ rule, which is often said to be derived from physical considerations of the particle collision with the wall; when the particle impacts with the wall its velocity is reversed. In fact, there has never been a suggestion that this is how real particles behave and this method originated from the LGA. When real particles impact with a wall they reflect either in a specular way, with the component of their velocity normal to the wall reversing, or in a diffusive way, returning from the wall in a random direction. Attempts have been made to replicate both these processes in LBM, notably by Sofonea and Sekerka (2005a).

Efforts have also been made to improve on the poor performance of the bounce-back method. Ziegler (1993) showed that the results of the bounce-back boundary condition more accurately represented a no-slip wall if the position of the wall was interpreted as half way between the last fluid node and the first solid node, a view shared by He et al. (1997). Another correction to the bounce-back method was proposed by Junk and Yang

(2005) who were particularly concerned with geometry that varied on a scale less than one grid spacing. Inamuro et al. (1995) devised a method where the unknown distribution functions at a wall were set to their equilibrium values with a counter slip-velocity such that the overall velocity was zero.

For open (inlet and outlet) boundary conditions there is no simple solution to be found in continuum theory, equivalent to bounce-back, and in some respects this has been an advantage in forcing the invention of more creative schemes. The situation can be simply stated by considering that at a straight boundary there are 3 unknown elements of \mathbf{f} , and usually only two hydrodynamic constraints. Noble et al. (1995b,a) considered closure methods for the extra unknown introduced at a boundary. Zou and He (1997) proposed what is probably the most popular scheme, the so-called ‘non-equilibrium bounce-back’ method (this scheme will be examined in Chapter 5). Yu et al. (2005) tried to modify the Zou and He method to reduce the reflection of pressure waves at the boundary.

For setting a non-zero velocity along the walls of a channel Latt et al. (2008) conducted a review of several methods, and found no significant differences between their performances. Hollis et al. (2008) used the viscous shear stress as a closure condition for boundaries, and went on to try and deal with nodes at the intersection between intersecting straight boundaries, something conspicuously absent from most other papers. Ginzburg and d’Humières (2003) conducted a review of the different methods of reflecting the particles from a surface.

An interesting approach was taken by Skordos (1993), who used finite difference approximations of the derivatives of the hydrodynamic variables to recreate the values of the higher moments at a boundary. Maier et al. (1996) and Chen et al. (1999) used extrapolation of the known elements of \mathbf{f} for the same purpose.

In general, schemes which extrapolate the boundary condition from the interior should be treated, in the opinion of the author, with suspicion. The boundary conditions are an essential part of the solution of partial differential equations, and they must be imposed on the PDE, not the other way around.

3.1.5 Improvements on LBGK

The Multiple Relaxation Time (MRT) collision term, proposed initially by Higuera et al. (1989) and later by Lallemand and Luo (2000), is an extension of the LBGK model. Each moment is relaxed at a different rate, and the collision terms are given by,

$$\Omega(\mathbf{f}) = M^{-1}\Lambda M(\mathbf{f}^{eq} - \mathbf{f}) \quad (3.3)$$

where Λ is a diagonal matrix of relaxation rates, explained in Section 4.3. This offers several advantages over LBGK, see for example Dellar (2003) and Reis and Phillips (2008). There are two different moment systems commonly used. Continuum kinetic methods use a moment basis of increasing powers of the molecular velocity, as explained in Section 2.4. The advantage of this basis is that it is easily extendable, and discrepancies between continuum kinetic theory and Lattice Boltzmann may be easily observed, as in Section 4.1.3. However, Lallemand and Luo (2000) used a moment basis derived from a purely mathematical background, such that the moments are orthogonal. This allows the identification and isolation of non-hydrodynamic ‘ghost’ moments, at the expense of a more conceptually complicated scheme. In terms of computational expense, it is not clear that either basis offers an advantage.

The single relaxation time model may be seen as a special case of the MRT model with all relaxation times set to the same value. Another special case is the two relaxation time scheme proposed by Ginzburg et al. (2008).

The motivation for the development of the MRT approach was to reduce the effect that higher order (unphysical) moments have on the lower order moments of interest. Latt and Chopard (2006) developed a novel solution, instead of MRT, to this problem. After each time step they ‘regularise’ \mathbf{f} to remove any influence from the higher order moments. This is computationally expensive however, and MRT offers a much neater solution. In fact, the Latt and Chopard (2006) method is equivalent to MRT with a particular choice of collision times that sets the higher moments to equilibrium after each collision, as in Higuera et al.

(1989) and McNamara et al. (1995).

3.1.6 LBM for multi-component fluids

In the modelling of mixtures of gases, there are two important differences from the single component method. Firstly, the effect of the different molecular masses of the gases must be taken into consideration. Secondly, the collision term must be modified to take into account the momentum exchanged between the species.

The first problem proves difficult to overcome using LBGK, as conventionally a non-physical equation of state is used and the grid spacing is proportional to the molecular masses, as will be explained in Section 4.1.6.

McCracken and Abraham (2005) proposed a method of interpolating between two differently spaced grids. However, this is too computationally intensive for real applications. If one considers that the ratio between the molecular masses of a binary gas could be, say, 20, the grid spacing ratio would have to be the same. Therefore a $10 \times 10 \times 10$ grid for one species would require a $200 \times 200 \times 200$ grid for the other species.

Yu and Zhao (2000) proposed a model that allowed a change in the equation of state using a finite difference based modification to the pressure term in the momentum equation. This was done with the use of an ‘attractive force term’ added to the collision term which then appeared in the momentum equation. The modified equation of state did not appear in the viscous terms however. Essentially, this was the first attempt at a model which would be developed more successfully by Dellar (2002b), who removed the need for the finite difference scheme. He developed a more robust model for generalised equations of state, based on the shallow water equations but applicable to any barotropic equation of state. Guo and Zhao (2003) applied essentially the same method to multiple gas mixtures.

To address the second problem it seems the natural choice to turn to continuum kinetic theory as described by Hamel (1966) and Sirovich (1962). The collision term in both these

models may be grossly simplified, and written as,

$$\Omega_\sigma = \Omega^{\sigma,\sigma} + \Omega^{\sigma,\varsigma} \quad (3.4)$$

Where $\Omega^{\sigma,\sigma}$ represents self-collisions between particles of the same species, and $\Omega^{\sigma,\varsigma}$ represents cross collisions between particles of different species. This approach was adopted by Sofonea and Sekerka (2001, 2005b) who realised that if BGK-style models are used to describe the collision process, such as,

$$\Omega_\sigma = \lambda^{\sigma,\sigma}(f_\sigma - f^{(eq),\sigma,\sigma}) + \lambda^{\sigma,\varsigma}(f_\sigma - f^{(eq),\sigma,\varsigma}), \quad (3.5)$$

then this expression may be rearranged into the form,

$$\Omega_\sigma = \lambda^*(f_\sigma - f^{(eq),*}) \quad (3.6)$$

where the values with a superscript * are functions of the self-collision and cross-collision relaxation frequencies and equilibrium functions. Sofonea and Sekerka set $f^{(eq),*}$ to be a function of the mixture velocity, the mass mean of the species velocities. The value of λ^* may then be set to model diffusion correctly, but the viscosity recovered is incorrect.

To circumvent this shortcoming, Facin et al. (2004), Luo and Girimaji (2002) and Asinari (2005) separately proposed ‘three relaxation time’ models, of the form of equation (3.5). Arcidiacono et al. (2006b,a, 2007) also proposed a similar model, but derived from an entropic point of view. Asinari (2006) demonstrated that when these models are written in the form of Equation (3.6) the equilibrium function does not have a simple form, implying that when a mixture composed of identical components is considered, it does not behave in the same way as a single gas.

Asinari (2008, 2009) developed a lattice Boltzmann model based on the Andries et al. (2002) (AAP) model for gas mixtures. Two vital points are established, the first is that the diffusive behaviour of the gases can be modelled by an exchange of momentum between the species. The second is that the MRT method can be used to apply different relaxation

times to the diffusive behaviour and the viscous behaviour. In this manner the diffusivity and viscosity can be made entirely independent of each other.

To summarise, the differentiation between self and cross collisions is appropriate for continuous kinetic theory. However, it is difficult to separate the diffusivity and viscosity of the gases in a LB model from this starting point. It is better to start from a moment basis, where diffusivity and viscosity are already separated.

3.1.7 LBM in porous media and solid oxide fuel cells

A review of the early work using LB for flow in porous materials can be found in Chen and Doolen (1998). Ahrenholz et al. (2006) provide an insight into how more complicated porous media geometries may be reconstructed in a computational model.

Several people have attempted to model flow through the porous material of a Solid Oxide Fuel Cell (SOFC). Asinari et al. (2007) used electron microscopy to image the SOFC electrolyte and then took average properties of grain size to reconstruct the geometry. Joshi et al. (2007b,a) thought that they modelled the non-continuum diffusion equations in porous media and SOFCs, despite only using a D2Q9 scheme. Both authors used bounce-back boundary conditions and, most importantly, did not refer to diffusion slip at the solid walls or even the slip between the species. The scope of these papers is very large, and it is difficult to validate their results quantitatively.

Wang and Afsharpoya (2006) considered much larger channels in SOFCs, and claimed to predict turbulence at high Reynolds numbers, again using a bounce back wall condition. Although not related to LBM, interesting work was done by Lee et al. (2002, 2003, 2005) on solid oxide fuel cell geometry and composition, although no attempt was made to model flow. Instead, permeability was deduced purely from geometric considerations.

Most recently, Rama et al. (2010) conducted a study of polymer electrolyte fuel cells, and integrated the flow computations with the electrochemistry. Unfortunately, they used the Luo and Girimaji (2002) model, in which each species' grid spacing is different. The extra interpolation needed because of this adds an unnecessary computational overhead.

Furthermore, there was no detailed consideration of fluid-solid boundaries, and the bounce-back boundary condition was used without justification or explanation.

3.2 Diffusion slip

The unusual history of diffusion slip is now described. The story is characterised by painstaking work over many years and a reluctance by the wider engineering community to accept clear experimental evidence. This should be contrasted with the often rushed work of the LBM community and their eagerness to accept new theories despite an absence of evidence.

The story begins with the work of Sir Thomas Graham, a Scottish chemist who lived between 1805 and 1869. His original papers, Graham (1876), although fascinating, are difficult to read now as concepts such as viscosity had not been formalised. However, Mason and Evans (1969) and Mason et al. (1969) have produced a modern summary, which should be considered essential reading for any student of this subject. Graham was responsible for discovering the relation which has become known as ‘Graham’s law’; when two gases diffuse into each other, under a condition of constant total pressure (defined as the sum of the partial pressures), the ratio of their molecular fluxes is inversely proportional to the square root of the ratio of their molecular masses. In the experiments conducted by Graham, a stucco plug was used to separate the two gases. Over time, the results of these experiments became confused, and it was wrongly assumed that the pores in the stucco must have been very small so that the result was due to non-continuum effects. In fact, stucco has rather large pores, and the gas flows were well within the continuum regime.

The scale of the misunderstanding regarding the zero total pressure drop problem is eloquently outlined by Mills (2003). If a diffusing gas mixture in a channel has constant total pressure, the mass mean velocity is not zero. Almost all standard text books claim the opposite, however, including Bennett and Myers (1982), Welty et al. (1984), White (1988), Holman (1988), Geankoplis (1993), Baehr and Stephan (1998), Incropera et al. (2001) and Cengel (1998). This is an astounding error in the history of the analysis of

diffusing gas mixtures.

The discrepancy has been highlighted and attempts have been made to address it from both a mathematical and an experimental point of view. Dullien and Scott (1962) and Evans et al. (1961b) both confirmed mathematically that Graham’s law applies for both continuum and non-continuum conditions in a channel. Excellent experiments were carried out by Knaff and Schlunder (1985), Hoogschagen (1955), Remick and Geankoplis (1973) and Evans et al. (1961a, 1962a,b, 1963). All these experiments confirmed Graham’s law over a wide range of pressures.

The reason for at least some of the confusion is due to the treatment of the solid wall boundary condition. Kramers and Kistemaker (1943) proposed that the mass mean velocity of a diffusing gas mixture is not zero at the wall. Instead they identified a ‘diffusion slip’ of the mixture directed, in the case of a binary gas, away from the higher concentration of the heavier gas. The magnitude of the diffusion slip velocity derived by Kramers and Kistemaker (1943) is,

$$u_{slip} = \left(\frac{M_A - M_B}{n_A M_A + n_B M_B} - \frac{\sqrt{M_B} - \sqrt{M_A}}{n_A \sqrt{M_A} + n_B \sqrt{M_B}} \right) D_{AB} \frac{dn_A}{dx} \quad (3.7)$$

where u_{slip} is the mixture slip velocity in the x direction. In this equation the light gas is A and the heavy gas is B , M_σ is the molar mass of gas σ , n_σ the number of molecules per unit volume of gas σ , D_{AB} the diffusion coefficient and x is the distance along the channel. The expression for the diffusion slip velocity was extended to multiple gas mixtures by Jackson (1977) and studied in some depth by Noever (1990a,b,c), who referred to it as the ‘baroeffect’.

More recently, Young and Todd (2005) and then Mills (2007) revisited the topic, but otherwise it remains relatively unexplored. In any application which has a small or zero total pressure change, but large changes in gas composition, correct modelling of diffusion slip at solid wall boundaries is essential.

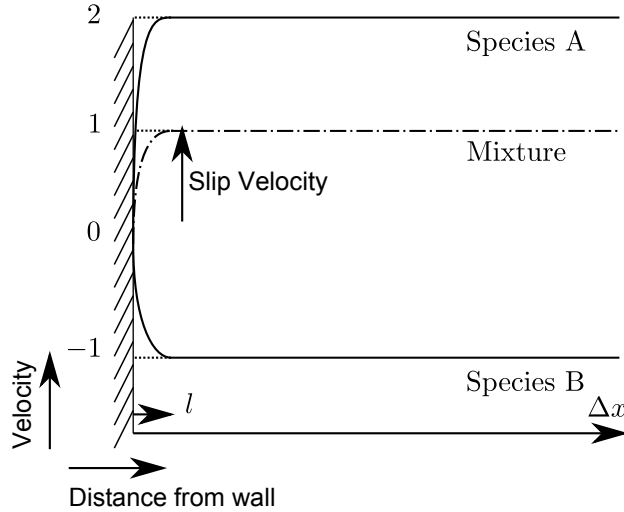


Figure 3.1: Species and mixture velocities tangential to the wall, close to a solid wall. A characteristic mean free path length is l , while a characteristic grid spacing may be Δx . The flat velocity profiles away from the wall indicate that viscous effects are small compared to the diffusive effect. The slip velocity of the mixture is predominantly due to diffusion slip.

3.2.1 Origin of diffusion slip

The question of exactly how diffusion slip occurs is now examined in more depth. Figure 3.1 shows the velocity profiles of a binary gas near a wall. In the bulk of the flow the total pressure gradient is small and a concentration gradient parallel to the wall and which is constant across the channel causes diffusion of the two species in a direction parallel to the wall. Some suitable average mean free path l is defined such that the particles less than a distance l from the wall collide with the wall without making any other collisions. In the region between the wall and a distance l from the wall the continuum equations, Navier-Stokes and Stefan-Maxwell, are not applicable. Unless this region is to be modelled correctly with the appropriate rarefied gas equations, boundary conditions appropriate to the continuum modelling level must be applied. Looking again at Figure 3.1, it is suggested that the appropriate continuum boundary conditions at the wall are indicated by the dotted lines. Finally, although the grid spacing Δx drawn on Figure 3.1 is larger than l , even if $\Delta x < l$ the no-slip condition would not be appropriate for the model developed in this work, as the governing equations cannot resolve physical effects on that scale.

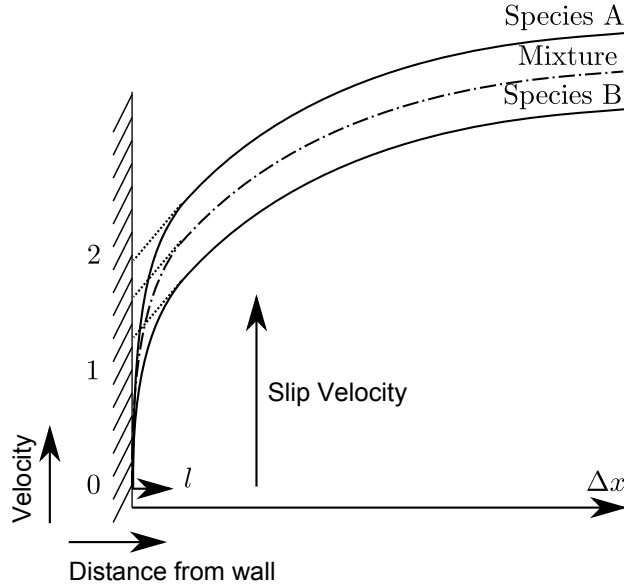


Figure 3.2: Species and mixture velocities tangential to the wall, close to a solid wall. A characteristic mean free path length is l , while a characteristic grid spacing may be Δx . The total pressure gradient is large, therefore the slip velocity at the wall is predominantly due to Knudsen slip (which can be ignored for continuum flow).

Figure 3.2 shows a binary gas subject to Knudsen slip, and is included for comparison with diffusion slip. The two are similar, however there is one very important distinction, Knudsen slip has a large effect when the pressure of the gas is so low, or the channel is so narrow, that the mean free path of the gas is no longer negligibly small. In such a case the Knudsen number (l/H where H is the channel width) is greater than, say, 0.01. Diffusion slip has a large effect when the diffusion fluxes of the species are much greater than the convective fluxes. Both types of slip occur at all times, however for low Knudsen numbers Knudsen slip can be ignored and for flows with high pressure gradients diffusion slip can be ignored.

The argument of Kramers and Kistemaker (1943), for a Maxwell gas with perfect diffusive reflection of molecules from the wall, is essentially as follows. The number of molecules of each gas passing through a surface parallel to the concentration gradient is $n_\sigma \bar{c}_\sigma / 4$, where \bar{c}_σ is the mean molecular velocity in the gas and n_σ is the number of molecules. The momentum carried through this surface is therefore $n_\sigma \bar{c}_\sigma m_\sigma u_\sigma / 4$, where m_σ is the mass of a

molecule of species σ and u_σ is the velocity of the species σ . If the surface is a stationary physical wall, the molecules returning from the wall have zero average velocity, and zero average momentum. Therefore, the total momentum crossing the surface is,

$$n_A \bar{c}_A m_A u_A + n_B \bar{c}_B m_B u_B = 0 \quad (3.8)$$

From the equipartition of energy $\sqrt{m_A} \bar{c}_A = \sqrt{m_B} \bar{c}_B$, and Equation (3.8) becomes,

$$\frac{\rho_A u_A}{\sqrt{M_A}} = -\frac{\rho_B u_B}{\sqrt{M_B}} \quad (3.9)$$

Loyalka (1971) extended this analysis to include the effect of different intermolecular force laws and gas-surface interactions. When the species have identical molecular masses, the analysis of Kramers and Kistemaker (1943) predicts zero slip, although a small slip velocity actually occurs due to these additional considerations. For species with very different molecular masses however, the Kramers and Kistemaker (1943) expression gives reasonably good agreement with Loyalka's full expression. This analysis was extended to a higher level of accuracy by involving a second order Chapman-Enskog expansion by Ivchenko et al. (2002). They found the diffusion slip coefficient was then highly sensitive to the model used for intermolecular forces.

A study of the layer adjacent to the wall was conducted using the numerical technique of molecular-dynamics by Mo and Rosenberger (1991). The results were, however, inconclusive. More recently, Kim et al. (2009) also studied this subject with both Direct Simulation Monte Carlo and D2Q9 and D2Q16 Lattice Boltzmann models. The results reported were very limited and did not recover Graham's law. Clearly, further work in this area is needed.

To the best of the author's knowledge, no attempt has been made to model macroscopic diffusive slip using the Lattice Boltzmann method.

Chapter 4

Single-Component Lattice Boltzmann

In this chapter, a kinetic-style scheme to solve the single component isothermal compressible Navier-Stokes equations is derived. The nine velocity two dimensional (D2Q9) grid is used. To make this model easily extendable to multi-component gas mixtures the correct Ideal Gas equation of state is used. This is not the norm in LBM and it does mean that a time accurate solution cannot be obtained, as will be demonstrated. However, unless a physical equation of state is used when multi-component gases are considered, the effect of the different molecular weights of the species cannot be incorporated into the model.

The system of moments is chosen, and then the equilibrium distribution function is defined using the principles of mass and momentum conservation. The higher equilibrium moments do not enter the mass and momentum equations and are selected on the grounds of stability. The results of Dellar (2002b) are used to ensure this. The relaxation process using the ‘Multiple Relaxation Time’ (MRT) model is investigated. An expression for the momentum flux density tensor including viscous terms leads to the momentum equation, which turns out to be the steady-state compressible Navier-Stokes equation.

The results of this chapter are not new, but the presentation and interpretation are unique. Chapman and Cowling (1970) introduced a very successful method of analysis for continuum kinetic theory, and this has been used with some success in Lattice Boltzmann methods. The principle idea is that the velocity distribution function is expanded in

terms of a small parameter, such that $f = f^{(0)} + \epsilon f^{(1)} + \epsilon f^{(2)} \dots$, and the time and space derivatives are similarly expanded. By substituting the expanded velocity distribution function into the Boltzmann equation, taking moments, and equating terms of similar powers in ϵ , equations for the macroscopic variables are recovered. The so-called zeroth approximation represents a flow at equilibrium. The first approximation leads to the Navier-Stokes equations and subsequent approximations lead to the Burnett equations and increasingly rarefied flow.

When the Boltzmann equation is represented in terms of just nine particle velocities the use of the Chapman-Enskog expansion is unnecessary. With such a limited set of particle velocities the third order moments are not independent, and effects past the Navier-Stokes level cannot be recovered. The parameter ϵ used in the Chapman-Enskog analysis is meaningless and instead will be replaced with small parameters (ϵ_{Ma} and ϵ_{Kn}) defined by the computational grid spacing and time step used to simulate the physical problem. These parameters should not be confused with the physical Mach and Knudsen numbers, although, in general, the literature does not make this distinction and can therefore be confusing.

4.1 The D2Q9 grid and the Boltzmann equation

4.1.1 The D2Q9 grid

This work is limited to the D2Q9 grid shown in Figure 4.1, with velocities given by;

$$\mathbf{e}_x = c \begin{pmatrix} 0 & 1 & 0 & -1 & 0 & 1 & -1 & -1 & 1 \end{pmatrix}^T \quad (4.1)$$

$$\mathbf{e}_y = c \begin{pmatrix} 0 & 0 & 1 & 0 & -1 & 1 & 1 & -1 & -1 \end{pmatrix}^T \quad (4.2)$$

where c is the speed at which the values f are moved across the lattice, the so-called ‘grid speed’. Models can be constructed with any number of velocities, but D2Q9 has the advantages of being compatible with a Cartesian grid and having independent zeroth and

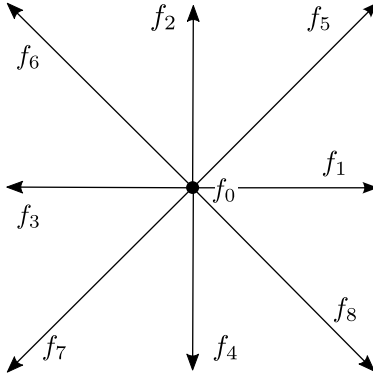


Figure 4.1: The D2Q9 grid. The velocity associated with f_0 is zero.

second order moments (like D1Q3 but unlike D1Q2). The velocity distribution function is expressed as a vector of the nine components,

$$\mathbf{f} = \left(f_0 \ f_1 \ f_2 \ f_3 \ f_4 \ f_5 \ f_6 \ f_7 \ f_8 \right)^T \quad (4.3)$$

As seen in Chapter 2 the Lattice Boltzmann method, when analysed with the use of a Taylor expansion, leads to a partial differential equations of the form,

$$\frac{\partial \mathbf{f}}{\partial t} + e_x \frac{\partial \mathbf{f}}{\partial x} + e_y \frac{\partial \mathbf{f}}{\partial y} = \Omega(\mathbf{f}) \quad (4.4)$$

In this case the resulting equation can be compared with the continuous Boltzmann equation, indeed the form is the same. However, such severe restrictions on \mathbf{f} exist that the comparison is almost meaningless. In the continuous Boltzmann equation, $\Omega(\mathbf{f})$ is a function that describes the effect that collisions between molecules have on the velocity distribution function. In the Lattice Boltzmann method, $\Omega(\mathbf{f})$ describes the effect of the ‘collision’ step in the calculation.

4.1.2 Scaling

Two scales are used throughout this work. A characteristic length, time and velocity for the physical problem L , t_f and U (where $Ut_f = L$) are defined. This establishes the non-

dimensional variables in the fluid dynamic scale (macroscopic), denoted by the use of a caret, like $\hat{\cdot}$.

$$\hat{x}_\alpha = \frac{x_\alpha}{L} \quad \hat{t} = \frac{t}{t_f} \quad \hat{u}_\alpha = \frac{u_\alpha}{U} \quad (4.5)$$

Another characteristic length, time and velocity Δx , Δt and c (where $\Delta t c = \Delta x$) are also defined. This is the computational scale. Δx and Δt are the grid length and time step and c will be called the ‘grid speed’. Variables in this scale are denoted with a $\tilde{\cdot}$.

$$\tilde{x}_\alpha = \frac{x_\alpha}{\Delta x} \quad \tilde{t} = \frac{t}{\Delta t} \quad \tilde{u}_\alpha = \frac{u_\alpha}{c} \quad (4.6)$$

The key advantage of the computational scale is that the scaled grid spacing and time step are unity. Two small parameters, ϵ_{Ma} and ϵ_{Kn} , are defined as,

$$\epsilon_{Kn} = \frac{\Delta x}{L} \quad \epsilon_{Ma} = \frac{U}{c} \quad (4.7)$$

The same scale is used for the density in the computational scale and in the fluid dynamic scale, such that $\tilde{\rho} = \hat{\rho} = \rho/\rho_0$. ρ_0 is a reference density, the value of which should be chosen so that $\tilde{\rho}$ is close to unity, to reduce numerical errors. The velocity distribution function f is scaled in the same way, $\tilde{f} = \hat{f} = f/\rho_0$.

For the pressure, sufficient scales are already defined thus,

$$\tilde{p} = \frac{p}{\rho_0 c^2} \quad \hat{p} = \frac{p}{\rho_0 U^2} \quad (4.8)$$

4.1.3 The truncated nine moment system

The continuum velocity distribution function can be described by an infinite set of integrals, or moments. However once the velocity set is reduced to nine velocities, just nine moments are needed to exactly reconstruct the discrete velocity distribution function. The definition of these moments is only subject to the condition that they must be independent, and different sets are commonly used. This discussion is restricted to the kinetic style set, and

			Π_0		
		Π_X		Π_Y	
	Π_{XX}		Π_{XY}		Π_{YY}
Π_{XXX}		Π_{XXY}		Π_{XYY}	Π_{YYY}
Π_{XXXX}	$\Pi_{XXX Y}$		Π_{XXYY}	Π_{XYYY}	Π_{YYYY}

Table 4.1: Moments of the D2Q9 velocity set

the results of other authors are converted into this set when appropriate.

The general notation for each moment, Π , is,

$$\Pi_{\underbrace{XXX}_m \underbrace{YYY}_n} = \sum_i e_{x,i}^m e_{y,i}^n f_i \quad (4.9)$$

A special case is $\Pi_0 = \sum_i f_i$. The first nine moments of this infinite set can be arranged as shown in Table 4.1. Due to the fact that the magnitude of the velocity components are unity in the computational scale, $\tilde{e}_\alpha^3 = \tilde{e}_\alpha$. This means that the moments that are ‘grayed out’ in Table 4.1 are not independent, and,

$$\Pi_{XXX} = \sum_i e_{x,i}^3 f_i = \sum_i c^3 \tilde{e}_{x,i}^3 f_i = \sum_i c^3 \tilde{e}_{x,i} f_i = \sum_i c^2 e_{x,i} f_i = c^2 \Pi_X \quad (4.10)$$

Similarly,

$$\Pi_{YYY} = c^2 \Pi_Y, \quad \Pi_{XXY} = c^2 \Pi_{XY}, \quad \Pi_{XYY} = c^2 \Pi_{XY} \quad (4.11)$$

The flux of each moment is related to the moments on the line beneath it in Table 4.1, as will be shown later. The nine independent moments may be arranged in a vector of moments \mathbf{m} as,

$$\mathbf{m} = (\Pi_0 \ \Pi_X \ \Pi_Y \ \Pi_{XX} \ \Pi_{YY} \ \Pi_{XY} \ \Pi_{XYY} \ \Pi_{XXY} \ \Pi_{XYYY})^T \quad (4.12)$$

In the computational scale the relation between \mathbf{m} and \mathbf{f} may be expressed as,

$$\tilde{\mathbf{m}} = \tilde{\mathbf{M}}\tilde{\mathbf{f}} \quad (4.13)$$

where $\tilde{\mathbf{M}}$ is the transform matrix,

$$\tilde{\mathbf{M}} = \begin{pmatrix} 1 & 1 & 1 & 1 & 1 & 1 & 1 & 1 & 1 \\ 0 & 1 & 0 & -1 & 0 & 1 & -1 & -1 & 1 \\ 0 & 0 & 1 & 0 & -1 & 1 & 1 & -1 & -1 \\ 0 & 1 & 0 & 1 & 0 & 1 & 1 & 1 & 1 \\ 0 & 0 & 1 & 0 & 1 & 1 & 1 & 1 & 1 \\ 0 & 0 & 0 & 0 & 0 & 1 & -1 & 1 & -1 \\ 0 & 0 & 0 & 0 & 0 & 1 & -1 & -1 & 1 \\ 0 & 0 & 0 & 0 & 0 & 1 & 1 & -1 & -1 \\ 0 & 0 & 0 & 0 & 0 & 1 & 1 & 1 & 1 \end{pmatrix} \quad (4.14)$$

4.1.4 The scaled evolution equation

The dimensions of the collision integral, $\Omega(f)$, is density time⁻¹, and it is non-dimensionalised by $\tilde{\Omega}(f) = \Omega(f)\Delta t/\rho_0$. Picking a mix of scalings which will later prove useful one can rewrite the evolution equation in non-dimensional form,

$$\frac{1}{t_f} \frac{\partial \tilde{f}_i}{\partial \hat{t}} + \frac{c}{L} \tilde{e}_{x,i} \frac{\partial \tilde{f}_i}{\partial \hat{x}} + \frac{c}{L} \tilde{e}_{y,i} \frac{\partial \tilde{f}_i}{\partial \hat{y}} = \frac{\tilde{\Omega}(\tilde{f}_i)}{t_c} \quad (4.15)$$

Then, substituting the definitions of the small parameters ϵ_{Ma} and ϵ_{Kn} yields,

$$\epsilon_{Ma}\epsilon_{Kn} \frac{\partial \tilde{f}_i}{\partial \hat{t}} + \epsilon_{Kn} \tilde{e}_{x,i} \frac{\partial \tilde{f}_i}{\partial \hat{x}} + \epsilon_{Kn} \tilde{e}_{y,i} \frac{\partial \tilde{f}_i}{\partial \hat{y}} = \tilde{\Omega}(\tilde{f}_i) \quad (4.16)$$

This equation will provide the vital link between the computational scheme and the equations for the macroscopic variables, as it links the quantities computed in the Boltzmann scale to the fluid dynamic length and time scales. In the D2Q9 model there are 9 values for

i , and nine equations, which translate into nine independent equations for the macroscopic variables.

4.1.5 Moments of the evolution equation

Nine unique moments were defined in Section 4.1.3 and now an equation for the evolution of these moments will be derived. This may easily be achieved using the evolution equation for the distribution function. Taking the vector form of Equation (4.16) and pre-multiplying by $\tilde{\mathbf{M}}$, results in the evolution equation for the moments,

$$\begin{aligned}
& \epsilon_{Ma} \epsilon_{Kn} \frac{\partial}{\partial \hat{t}} \begin{pmatrix} \tilde{\Pi}_0 \\ \tilde{\Pi}_X \\ \tilde{\Pi}_Y \\ \tilde{\Pi}_{XX} \\ \tilde{\Pi}_{YY} \\ \tilde{\Pi}_{XY} \\ \tilde{\Pi}_{XYY} \\ \tilde{\Pi}_{XXY} \\ \tilde{\Pi}_{XXY} \end{pmatrix} + \epsilon_{Kn} \frac{\partial}{\partial \hat{x}} \begin{pmatrix} \tilde{\Pi}_X \\ \tilde{\Pi}_{XX} \\ \tilde{\Pi}_{XY} \\ \tilde{\Pi}_X \\ \tilde{\Pi}_{XYY} \\ \tilde{\Pi}_{XXY} \\ \tilde{\Pi}_{XXY} \\ \tilde{\Pi}_{XY} \\ \tilde{\Pi}_{XYY} \end{pmatrix} + \epsilon_{Kn} \frac{\partial}{\partial \hat{y}} \begin{pmatrix} \tilde{\Pi}_Y \\ \tilde{\Pi}_{XY} \\ \tilde{\Pi}_{YY} \\ \tilde{\Pi}_{XXY} \\ \tilde{\Pi}_Y \\ \tilde{\Pi}_{XYY} \\ \tilde{\Pi}_{XY} \\ \tilde{\Pi}_{XXY} \\ \tilde{\Pi}_{XXY} \end{pmatrix} = \\
& \begin{pmatrix} \sum_i \tilde{\Omega}_i(f) \\ \sum_i \tilde{e}_{x,i} \tilde{\Omega}_i(f) \\ \sum_i \tilde{e}_{y,i} \tilde{\Omega}_i(f) \\ \sum_i \tilde{e}_{x,i} \tilde{e}_{x,i} \tilde{\Omega}_i(f) \\ \sum_i \tilde{e}_{y,i} \tilde{e}_{y,i} \tilde{\Omega}_i(f) \\ \sum_i \tilde{e}_{x,i} \tilde{e}_{y,i} \tilde{\Omega}_i(f) \\ \sum_i \tilde{e}_{x,i} \tilde{e}_{y,i} \tilde{e}_{y,i} \tilde{\Omega}_i(f) \\ \sum_i \tilde{e}_{x,i} \tilde{e}_{x,i} \tilde{e}_{y,i} \tilde{\Omega}_i(f) \\ \sum_i \tilde{e}_{x,i} \tilde{e}_{x,i} \tilde{e}_{y,i} \tilde{e}_{y,i} \tilde{\Omega}_i(f) \end{pmatrix} \quad (4.17)
\end{aligned}$$

This provides further proof that the moment system is truncated, as the evolution of each moment can be described without reference to any moment outside the chosen set of nine. Thus there is no direct equivalent to Newton's viscosity law; the momentum equation cannot be expressed purely in terms of density and velocity. Instead, the viscosity is controlled by the relaxation frequency of the second order moments.

4.1.6 The equation of state

The Ideal Gas equation links the pressure of the gas to the density,

$$\tilde{p} = \tilde{RT}\tilde{\rho} \tag{4.18}$$

Where \tilde{RT} is the gas constant divided by c^2 . Several authors, For example Reis and Phillips (2008) and Lallemand and Luo (2000), propose $(\tilde{RT}) = 1/3$ for maximum stability and accuracy. However in doing so they are abandoning the physical equation of state in favour of a new, unphysical, link between pressure and density that is a function of the scaling used. In the incompressible limit the equation of state may be ignored, but for multicomponent applications it is vital that the equation of state is correct. The correct Ideal gas equation is used in this chapter to ensure the results may be extended to multicomponent gas mixtures.

4.2 The equilibrium distribution

Conventionally, equilibrium has been defined when all the moments of $\Omega(f)$ are zero. For the continuous Boltzmann equation this is a sensible proposition; it is not the same as saying that there are no collisions, just that the collisions on average have no effect on the macroscopic properties. In the Lattice Boltzmann method equilibrium is defined in the same way, noting the higher moments will still be affected by the finite number of velocities, and so the particle distribution function cannot be compared to its continuum equivalent. Therefore, in this section the right hand side of equation (4.17) will be set to zero and the

moments given the superscript (eq) to indicate that they refer to the equilibrium state.

4.2.1 Mass conservation

The first moment of the evolution equation, (4.17), at equilibrium is

$$\epsilon_{Kn}\epsilon_{Ma}\frac{\partial\tilde{\Pi}_0^{(eq)}}{\partial\hat{t}} + \epsilon_{Kn}\frac{\partial\tilde{\Pi}_X^{(eq)}}{\partial\hat{x}} + \epsilon_{Kn}\frac{\partial\tilde{\Pi}_Y^{(eq)}}{\partial\hat{y}} = 0 \quad (4.19)$$

The mass conservation equation in the fluid dynamic scaling is,

$$\frac{\partial\hat{\rho}}{\partial\hat{t}} + \frac{\partial(\hat{\rho}\hat{u}_x)}{\partial\hat{x}} + \frac{\partial(\hat{\rho}\hat{u}_y)}{\partial\hat{y}} = 0 \quad (4.20)$$

By comparison between the form of these equations, the lower order moments of the equilibrium function may be defined as,

$$\tilde{\Pi}_0^{(eq)} = \hat{\rho} \quad (4.21)$$

$$\tilde{\Pi}_X^{(eq)} = \epsilon_{Ma}\hat{\rho}\hat{u}_x \quad (4.22)$$

$$\tilde{\Pi}_Y^{(eq)} = \epsilon_{Ma}\hat{\rho}\hat{u}_y \quad (4.23)$$

Using these relations the D2Q9 model exactly recovers the mass conservation law with a discrete velocity set. Numerical effects due to discretizing space and time have yet to be considered.

4.2.2 Momentum conservation

The second and third moments of the evolution equation, (4.17), at equilibrium are:

$$\epsilon_{Kn}\epsilon_{Ma}^2\frac{\partial(\hat{\rho}\hat{u}_x)}{\partial\hat{t}} + \epsilon_{Kn}\frac{\partial\tilde{\Pi}_{XX}^{eq}}{\partial\hat{x}} + \epsilon_{Kn}\frac{\partial\tilde{\Pi}_{XY}^{eq}}{\partial\hat{y}} = 0 \quad (4.24)$$

$$\epsilon_{Kn}\epsilon_{Ma}^2\frac{\partial(\hat{\rho}\hat{u}_y)}{\partial\hat{t}} + \epsilon_{Kn}\frac{\partial\tilde{\Pi}_{XY}^{eq}}{\partial\hat{x}} + \epsilon_{Kn}\frac{\partial\tilde{\Pi}_{YY}^{eq}}{\partial\hat{y}} = 0 \quad (4.25)$$

where Equation (4.22) and (4.23) have been used. The equilibrium form of the momentum conservation equation is

$$\frac{\partial(\hat{\rho}\hat{u}_x)}{\partial\hat{t}} + \frac{\partial(\hat{p} + \hat{\rho}\hat{u}_x^2)}{\partial\hat{x}} + \frac{\partial(\hat{\rho}\hat{u}_y\hat{u}_x)}{\partial\hat{y}} = 0 \quad (4.26)$$

$$\frac{\partial(\hat{\rho}\hat{u}_y)}{\partial\hat{t}} + \frac{\partial(\hat{\rho}\hat{u}_y\hat{u}_x)}{\partial\hat{x}} + \frac{\partial(\hat{p} + \hat{\rho}\hat{u}_y^2)}{\partial\hat{y}} = 0 \quad (4.27)$$

From comparison between these two sets of equations the second order moments must be,

$$\tilde{\Pi}_{XX}^{eq} = \epsilon_{Ma}^2(\hat{p} + \hat{\rho}\hat{u}_x^2) \quad (4.28)$$

$$\tilde{\Pi}_{YY}^{eq} = \epsilon_{Ma}^2(\hat{p} + \hat{\rho}\hat{u}_y^2) \quad (4.29)$$

$$\tilde{\Pi}_{XY}^{eq} = \epsilon_{Ma}^2(\hat{\rho}\hat{u}_y\hat{u}_x) \quad (4.30)$$

4.2.3 Higher moments

The higher moments present a problem for the nine velocity model. In continuous kinetic theory the first order moments are the mass flux, the second order moments are the momentum flux and the third order moments are the energy flux. Therefore, the appropriate equation to use for defining the equilibrium values of the third order moments would be the conservation of energy. However, it is in the third order moments that the D2Q9 lattice starts to show its deficiencies ($\tilde{\Pi}_{XXX} = \tilde{\Pi}_X$ and $\tilde{\Pi}_{YYY} = \tilde{\Pi}_Y$), and so it is impossible to recover the energy equation correctly. The scheme is often referred to as isothermal because the BGK collision operator is intentional changed to conserve temperature rather than energy under collisions, see Dellar (2001). D’Humières (1992) formulated a thermal D2Q9 scheme, but it only correctly reproduces the Euler equations. The non-equilibrium part of the third order moments should not be regarded as meaningful, although the equilibrium parts have to take the correct values that yield the Navier-Stokes equations.

There is another problem with the higher moments: they may cause instability. Instability of this type is normally associated with an oscillation on a wavelength equal to the grid spacing, and cannot be identified using the long wavelength analysis used here. The

priority when assigning equilibrium values to the higher moments is therefore to suppress this instability. Dellar (2002b) has analysed these unstable modes and recommends values for the higher moments. Because he has used a different moment base, they are translated here,

$$\tilde{\Pi}_{XXY}^{eq} = \epsilon_{Ma} \frac{1}{3} \hat{\rho} \hat{u}_y \quad (4.31)$$

$$\tilde{\Pi}_{XYX}^{eq} = \epsilon_{Ma} \frac{1}{3} \hat{\rho} \hat{u}_x \quad (4.32)$$

$$\tilde{\Pi}_{XXYY}^{eq} = \epsilon_{Ma}^2 \frac{1}{3} (p + \hat{\rho} \hat{u}_x^2 + \hat{\rho} \hat{u}_y^2) \quad (4.33)$$

The third order equilibrium moments also appear in the expression for the momentum flux density tensor, however the fourth order moment has no impact on the hydrodynamic variables. As such, any interest in it is small; if it is stable that is sufficient.

4.2.4 Recovering the equilibrium distribution function

Once the moments of the equilibrium distribution function are known, it is a trivial task to recover the actual function, using the linear mapping matrix \tilde{M} .

$$\tilde{\mathbf{f}}^{eq} = \tilde{M}^{-1} \tilde{\mathbf{m}}^{eq} \quad (4.34)$$

Where the equilibrium moments are,

$$\tilde{\mathbf{m}}^{eq} = \begin{pmatrix} \tilde{\Pi}_0^{(eq)} \\ \tilde{\Pi}_X^{(eq)} \\ \tilde{\Pi}_Y^{(eq)} \\ \tilde{\Pi}_{XX}^{(eq)} \\ \tilde{\Pi}_{YY}^{(eq)} \\ \tilde{\Pi}_{XY}^{(eq)} \\ \tilde{\Pi}_{XYY}^{(eq)} \\ \tilde{\Pi}_{XXY}^{(eq)} \\ \tilde{\Pi}_{XXYY}^{(eq)} \end{pmatrix} = \begin{pmatrix} \hat{\rho} \\ \epsilon_{Ma} \hat{\rho} \hat{u}_x \\ \epsilon_{Ma} \hat{\rho} \hat{u}_y \\ \epsilon_{Ma}^2 (\hat{p} + \hat{\rho} \hat{u}_x^2) \\ \epsilon_{Ma}^2 (\hat{p} + \hat{\rho} \hat{u}_y^2) \\ \epsilon_{Ma}^2 (\hat{\rho} \hat{u}_x \hat{u}_y) \\ \epsilon_{Ma} \frac{1}{3} \hat{\rho} \hat{u}_x \\ \epsilon_{Ma} \frac{1}{3} \hat{\rho} \hat{u}_y \\ \epsilon_{Ma}^2 \frac{1}{3} (\hat{p} + \hat{\rho} \hat{u}_x^2 + \hat{\rho} \hat{u}_y^2) \end{pmatrix} = \begin{pmatrix} \tilde{\rho} \\ \tilde{\rho} \tilde{u}_x \\ \tilde{\rho} \tilde{u}_y \\ (\tilde{p} + \tilde{\rho} \tilde{u}_x^2) \\ (\tilde{p} + \tilde{\rho} \tilde{u}_y^2) \\ (\tilde{\rho} \tilde{u}_x \tilde{u}_y) \\ \frac{1}{3} \tilde{\rho} \tilde{u}_x \\ \frac{1}{3} \tilde{\rho} \tilde{u}_y \\ \frac{1}{3} (\tilde{p} + \tilde{\rho} \tilde{u}_x^2 + \tilde{\rho} \tilde{u}_y^2) \end{pmatrix} \quad (4.35)$$

Using the equation of state to remove references to pressure, $\tilde{\mathbf{f}}^{(eq)}$ can be written as,

$$\tilde{\mathbf{f}}^{eq} = \begin{pmatrix} \tilde{f}_0^{(eq)} \\ \tilde{f}_1^{(eq)} \\ \tilde{f}_2^{(eq)} \\ \tilde{f}_3^{(eq)} \\ \tilde{f}_4^{(eq)} \\ \tilde{f}_5^{(eq)} \\ \tilde{f}_6^{(eq)} \\ \tilde{f}_7^{(eq)} \\ \tilde{f}_8^{(eq)} \end{pmatrix} = \begin{pmatrix} -\frac{1}{3} \tilde{\rho} (5(\tilde{RT}) - 3 + 2(\tilde{u}_x^2 + \tilde{u}_y^2)) \\ \frac{1}{6} \tilde{\rho} (2\tilde{u}_x^2 - \tilde{u}_y^2 + 2\tilde{u}_x + 2(\tilde{RT})) \\ \frac{1}{6} \tilde{\rho} (-\tilde{u}_x^2 + 2\tilde{u}_y^2 + 2\tilde{u}_y + 2(\tilde{RT})) \\ \frac{1}{6} \tilde{\rho} (2\tilde{u}_x^2 - \tilde{u}_y^2 - 2\tilde{u}_x + 2(\tilde{RT})) \\ \frac{1}{6} \tilde{\rho} (-\tilde{u}_x^2 + 2\tilde{u}_y^2 - 2\tilde{u}_y + 2(\tilde{RT})) \\ \frac{1}{12} \tilde{\rho} (\tilde{u}_x^2 + \tilde{u}_y^2 + 3\tilde{u}_x \tilde{u}_y + \tilde{u}_x + \tilde{u}_y + (\tilde{RT})) \\ \frac{1}{12} \tilde{\rho} (\tilde{u}_x^2 + \tilde{u}_y^2 - 3\tilde{u}_x \tilde{u}_y - \tilde{u}_x + \tilde{u}_y + (\tilde{RT})) \\ \frac{1}{12} \tilde{\rho} (\tilde{u}_x^2 + \tilde{u}_y^2 + 3\tilde{u}_x \tilde{u}_y - \tilde{u}_x - \tilde{u}_y + (\tilde{RT})) \\ \frac{1}{12} \tilde{\rho} (\tilde{u}_x^2 + \tilde{u}_y^2 - 3\tilde{u}_x \tilde{u}_y + \tilde{u}_x - \tilde{u}_y + (\tilde{RT})) \end{pmatrix} \quad (4.36)$$

4.3 The MRT collision operator

The Multiple Relaxation Time (MRT) collision operator involves a linear relaxation to equilibrium. Each moment of the distribution function will relax towards its equilibrium value at a different rate, controlled by a relaxation frequency. These relaxation frequencies

are assembled in a matrix Λ ,

$$\Lambda = \begin{pmatrix} \lambda^0 & 0 & 0 & 0 & 0 & 0 & 0 & 0 & 0 \\ 0 & \lambda^1 & 0 & 0 & 0 & 0 & 0 & 0 & 0 \\ 0 & 0 & \lambda^2 & 0 & 0 & 0 & 0 & 0 & 0 \\ 0 & 0 & 0 & \frac{\lambda^\xi + \lambda^\nu}{2} & \frac{\lambda^\xi - \lambda^\nu}{2} & 0 & 0 & 0 & 0 \\ 0 & 0 & 0 & \frac{\lambda^\xi - \lambda^\nu}{2} & \frac{\lambda^\xi + \lambda^\nu}{2} & 0 & 0 & 0 & 0 \\ 0 & 0 & 0 & 0 & 0 & \lambda^\nu & 0 & 0 & 0 \\ 0 & 0 & 0 & 0 & 0 & 0 & \lambda^6 & 0 & 0 \\ 0 & 0 & 0 & 0 & 0 & 0 & 0 & \lambda^7 & 0 \\ 0 & 0 & 0 & 0 & 0 & 0 & 0 & 0 & \lambda^8 \end{pmatrix} \quad (4.37)$$

λ^ν controls shear viscosity while λ^ξ is related to bulk viscosity. Splitting the terms like this will enable these two effects to be separated. Isotropy requires that $\lambda^1 = \lambda^2$ and $\lambda^6 = \lambda^7$.

The collision operator for the velocity distribution function is constructed by pre-multiplying the distribution function evolution equation, (4.16), by M to get the moment evolution equation, then setting the right hand side to be a linear relaxation to equilibrium.

$$M\Omega(\mathbf{f}) = \Lambda(\mathbf{m}^{eq} - \mathbf{m}) \quad (4.38)$$

Premultiplying by the inverse of M , the collision operator becomes,

$$\Omega(\mathbf{f}) = M^{-1}\Lambda(\mathbf{m}^{eq} - \mathbf{m}) = M^{-1}\Lambda M(\mathbf{f}^{eq} - \mathbf{f}) \quad (4.39)$$

In the applications considered in this work mass is always conserved during a collision, and hence the value for λ^0 will always be multiplied by zero and is irrelevant. If mass is not conserved, for example due to chemical reactions, this would not be the case. Likewise, for single component gases, momentum is conserved and λ^1 and λ^2 are irrelevant. In multi-component gases momentum is exchanged between the species.

4.3.1 Evolution of moments

Taking moments of the evolution Equation (4.16) results in the evolution equation for the nine moments, and if the MRT collision operator is used the result is,

$$\begin{aligned}
& \epsilon_{Ma} \epsilon_{Kn} \frac{\partial}{\partial \hat{t}} \begin{pmatrix} \tilde{\Pi}_0 \\ \tilde{\Pi}_X \\ \tilde{\Pi}_Y \\ \tilde{\Pi}_{XX} \\ \tilde{\Pi}_{YY} \\ \tilde{\Pi}_{XY} \\ \tilde{\Pi}_{XYY} \\ \tilde{\Pi}_{XXY} \\ \tilde{\Pi}_{XYY} \end{pmatrix} + \epsilon_{Kn} \frac{\partial}{\partial \hat{x}} \begin{pmatrix} \tilde{\Pi}_X \\ \tilde{\Pi}_{XX} \\ \tilde{\Pi}_{XY} \\ \tilde{\Pi}_X \\ \tilde{\Pi}_{XYY} \\ \tilde{\Pi}_{XXY} \\ \tilde{\Pi}_{XYY} \\ \tilde{\Pi}_{XXY} \\ \tilde{\Pi}_{XYY} \end{pmatrix} + \epsilon_{Kn} \frac{\partial}{\partial \hat{y}} \begin{pmatrix} \tilde{\Pi}_Y \\ \tilde{\Pi}_{XY} \\ \tilde{\Pi}_{YY} \\ \tilde{\Pi}_{XXY} \\ \tilde{\Pi}_Y \\ \tilde{\Pi}_{XYY} \\ \tilde{\Pi}_{XY} \\ \tilde{\Pi}_{XXY} \\ \tilde{\Pi}_{XYY} \end{pmatrix} \\
& = \begin{pmatrix} \tilde{\lambda}^0 (\tilde{\Pi}_0^{eq} - \tilde{\Pi}_0) \\ \tilde{\lambda}^1 (\tilde{\Pi}_X^{eq} - \tilde{\Pi}_X) \\ \tilde{\lambda}^2 (\tilde{\Pi}_Y^{eq} - \tilde{\Pi}_Y) \\ \frac{\tilde{\lambda}^\xi + \tilde{\lambda}^\nu}{2} (\tilde{\Pi}_{XX}^{eq} - \tilde{\Pi}_{XX}) + \frac{\tilde{\lambda}^\xi - \tilde{\lambda}^\nu}{2} (\tilde{\Pi}_{YY}^{eq} - \tilde{\Pi}_{YY}) \\ \frac{\tilde{\lambda}^\xi + \tilde{\lambda}^\nu}{2} (\tilde{\Pi}_{YY}^{eq} - \tilde{\Pi}_{YY}) + \frac{\tilde{\lambda}^\xi - \tilde{\lambda}^\nu}{2} (\tilde{\Pi}_{XX}^{eq} - \tilde{\Pi}_{XX}) \\ \tilde{\lambda}^\nu (\tilde{\Pi}_{XY}^{eq} - \tilde{\Pi}_{XY}) \\ \tilde{\lambda}^6 (\tilde{\Pi}_{XYY}^{eq} - \tilde{\Pi}_{XYY}) \\ \tilde{\lambda}^7 (\tilde{\Pi}_{XXY}^{eq} - \tilde{\Pi}_{XXY}) \\ \tilde{\lambda}^8 (\tilde{\Pi}_{XYY}^{eq} - \tilde{\Pi}_{XYY}) \end{pmatrix} \quad (4.40)
\end{aligned}$$

To obtain the correct mass conservation equation $\tilde{\Pi}_0 = \tilde{\Pi}_0^{eq} = \hat{\rho}$ and $\tilde{\Pi}_\alpha = \tilde{\Pi}_\alpha^{(eq)} = \epsilon_{Ma} \hat{\rho} \hat{u}_\alpha$. The momentum equation involves the terms, $\tilde{\Pi}_{XX}$, $\tilde{\Pi}_{YY}$ and $\tilde{\Pi}_{XY}$, which are not at equilibrium. It will require some assumptions to simplify these terms.

4.3.2 The momentum flux density tensor (Π_{XX}, Π_{XY} and Π_{YY})

The components of the momentum flux density tensor appear in the 4th, 5th and 6th rows of Equation (4.40), where they are expressed in terms of the derivatives of the other moments. An expression for the higher moments is currently unknown, but could be calculated from the final three rows of Equation (4.40). Such a calculation would be very complicated and to simplify this problem the Maxwellian iteration of Ikenberry and Truesdell (1956) is used. VanKampen (1987) and Dellar (2002a) proved that this approach is equivalent to the Chapman-Enskog method for recovering the Navier-Stokes equations. Equilibrium values (from Equation (4.35)) are substituted into the left hand side of Equation (4.40), while retaining the real distribution function (that is, not at equilibrium) on the right hand side. The 4th, 5th and 6th rows become:

$$\begin{aligned} \epsilon_{Ma}\epsilon_{Kn}\frac{\partial}{\partial \hat{t}} \begin{pmatrix} \epsilon_{Ma}^2(\hat{p} + \hat{\rho}\hat{u}_x^2) \\ \epsilon_{Ma}^2(\hat{p} + \hat{\rho}\hat{u}_y^2) \\ \epsilon_{Ma}^2(\hat{\rho}\hat{u}_x\hat{u}_y) \end{pmatrix} + \epsilon_{Kn}\frac{\partial}{\partial \hat{x}} \begin{pmatrix} \epsilon_{Ma}\hat{\rho}\hat{u}_x \\ \epsilon_{Ma}\frac{1}{3}\hat{\rho}\hat{u}_x \\ \epsilon_{Ma}\frac{1}{3}\hat{\rho}\hat{u}_y \end{pmatrix} + \epsilon_{Kn}\frac{\partial}{\partial \hat{y}} \begin{pmatrix} \epsilon_{Ma}\frac{1}{3}\hat{\rho}\hat{u}_y \\ \epsilon_{Ma}\hat{\rho}\hat{u}_y \\ \epsilon_{Ma}\frac{1}{3}\hat{\rho}\hat{u}_x \end{pmatrix} \\ \approx \begin{pmatrix} \frac{\tilde{\lambda}^\xi + \tilde{\lambda}^\nu}{2}(\tilde{\Pi}_{XX}^{eq} - \tilde{\Pi}_{XX}) + \frac{\tilde{\lambda}^\xi - \tilde{\lambda}^\nu}{2}(\tilde{\Pi}_{YY}^{eq} - \tilde{\Pi}_{YY}) \\ \frac{\tilde{\lambda}^\xi + \tilde{\lambda}^\nu}{2}(\tilde{\Pi}_{YY}^{eq} - \tilde{\Pi}_{YY}) + \frac{\tilde{\lambda}^\xi - \tilde{\lambda}^\nu}{2}(\tilde{\Pi}_{XX}^{eq} - \tilde{\Pi}_{XX}) \\ \tilde{\lambda}^\nu(\tilde{\Pi}_{XY}^{eq} - \tilde{\Pi}_{XY}) \end{pmatrix} \quad (4.41) \end{aligned}$$

The Ideal Gas Equation, (4.18), is used to replace pressure terms with density terms, and when the expressions for the equilibrium moments is included on the left hand side

Equation (4.41) becomes,

$$\begin{aligned}
& \epsilon_{Ma} \epsilon_{Kn} \frac{\partial}{\partial \hat{t}} \begin{pmatrix} \tilde{RT} \hat{\rho} + \epsilon_{Ma}^2 (\hat{\rho} \hat{u}_x^2) \\ \tilde{RT} \hat{\rho} + \epsilon_{Ma}^2 (\hat{\rho} \hat{u}_y^2) \\ \epsilon_{Ma}^2 (\hat{\rho} \hat{u}_x \hat{u}_y) \end{pmatrix} + \epsilon_{Kn} \frac{\partial}{\partial \hat{x}} \begin{pmatrix} \epsilon_{Ma} \hat{\rho} \hat{u}_x \\ \epsilon_{Ma} \frac{1}{3} \hat{\rho} \hat{u}_x \\ \epsilon_{Ma} \frac{1}{3} \hat{\rho} \hat{u}_y \end{pmatrix} + \epsilon_{Kn} \frac{\partial}{\partial \hat{y}} \begin{pmatrix} \epsilon_{Ma} \frac{1}{3} \hat{\rho} \hat{u}_y \\ \epsilon_{Ma} \hat{\rho} \hat{u}_y \\ \epsilon_{Ma} \frac{1}{3} \hat{\rho} \hat{u}_x \end{pmatrix} \\
& \approx \begin{pmatrix} \frac{\tilde{\lambda}^\xi + \tilde{\lambda}^\nu}{2} (\epsilon_{Ma}^2 (\hat{p} + \hat{\rho} \hat{u}_x^2) - \tilde{\Pi}_{XX}) + \frac{\tilde{\lambda}^\xi - \tilde{\lambda}^\nu}{2} (\epsilon_{Ma}^2 (\hat{p} + \hat{\rho} \hat{u}_y^2) - \tilde{\Pi}_{YY}) \\ \frac{\tilde{\lambda}^\xi + \tilde{\lambda}^\nu}{2} (\epsilon_{Ma}^2 (\hat{p} + \hat{\rho} \hat{u}_y^2) - \tilde{\Pi}_{YY}) + \frac{\tilde{\lambda}^\xi - \tilde{\lambda}^\nu}{2} (\epsilon_{Ma}^2 (\hat{p} + \hat{\rho} \hat{u}_x^2) - \tilde{\Pi}_{XX}) \\ \tilde{\lambda}^\nu (\epsilon_{Ma}^2 \hat{\rho} \hat{u}_x \hat{u}_y - \tilde{\Pi}_{XY}) \end{pmatrix} \quad (4.42)
\end{aligned}$$

With any physical (that is, independent of scaling) equation of state the correct unsteady equations cannot be recovered, only the steady-state Navier-Stokes equations can be recovered. To illustrate this point the terms that lead to this error will be included, but removed at a later stage. However, to simplify the algebra the terms of the type $\partial(\rho u)/\partial t$ will be set to zero at this stage. The mass conservation equation, (4.20), is used to change the remaining time derivative terms to spatial derivatives.

$$\begin{aligned}
& \epsilon_{Kn} \epsilon_{Ma} \frac{\partial}{\partial \hat{x}} \begin{pmatrix} (1 - \tilde{RT}) \hat{\rho} \hat{u}_x \\ (\frac{1}{3} - \tilde{RT}) \hat{\rho} \hat{u}_x \\ \frac{1}{3} \hat{\rho} \hat{u}_y \end{pmatrix} + \epsilon_{Kn} \epsilon_{Ma} \frac{\partial}{\partial \hat{y}} \begin{pmatrix} (\frac{1}{3} - \tilde{RT}) \hat{\rho} \hat{u}_y \\ (1 - \tilde{RT}) \hat{\rho} \hat{u}_y \\ \frac{1}{3} \hat{\rho} \hat{u}_x \end{pmatrix} \\
& \approx \begin{pmatrix} \frac{\tilde{\lambda}^\xi + \tilde{\lambda}^\nu}{2} (\epsilon_{Ma}^2 (\hat{p} + \hat{\rho} \hat{u}_x^2) - \tilde{\Pi}_{XX}) + \frac{\tilde{\lambda}^\xi - \tilde{\lambda}^\nu}{2} (\epsilon_{Ma}^2 (\hat{p} + \hat{\rho} \hat{u}_y^2) - \tilde{\Pi}_{YY}) \\ \frac{\tilde{\lambda}^\xi + \tilde{\lambda}^\nu}{2} (\epsilon_{Ma}^2 (\hat{p} + \hat{\rho} \hat{u}_y^2) - \tilde{\Pi}_{YY}) + \frac{\tilde{\lambda}^\xi - \tilde{\lambda}^\nu}{2} (\epsilon_{Ma}^2 (\hat{p} + \hat{\rho} \hat{u}_x^2) - \tilde{\Pi}_{XX}) \\ \tilde{\lambda}^\nu (\epsilon_{Ma}^2 \hat{\rho} \hat{u}_x \hat{u}_y - \tilde{\Pi}_{XY}) \end{pmatrix} \quad (4.43)
\end{aligned}$$

After rearranging, the normal components of the momentum flux density tensor are given by,

$$\begin{aligned} \begin{pmatrix} \tilde{\Pi}_{XX} \\ \tilde{\Pi}_{YY} \end{pmatrix} &\approx \begin{pmatrix} \epsilon_{Ma}^2(\hat{p} + \hat{\rho}\hat{u}_x^2) \\ \epsilon_{Ma}^2(\hat{p} + \hat{\rho}\hat{u}_y^2) \end{pmatrix} - \\ &\epsilon_{Ma}\epsilon_{Kn} \left[\frac{\partial}{\partial \hat{x}} \begin{pmatrix} (\frac{1}{3}(\frac{1}{\lambda^\epsilon} + \frac{1}{\lambda^\nu}) + \frac{1}{\lambda^\epsilon}(\frac{1}{3} - \tilde{RT}))\hat{\rho}\hat{u}_x \\ (\frac{1}{3}(\frac{1}{\lambda^\epsilon} - \frac{1}{\lambda^\nu}) + \frac{1}{\lambda^\epsilon}(\frac{1}{3} - \tilde{RT}))\hat{\rho}\hat{u}_x \end{pmatrix} \right. \\ &\quad \left. + \frac{\partial}{\partial \hat{y}} \begin{pmatrix} (\frac{1}{3}(\frac{1}{\lambda^\epsilon} - \frac{1}{\lambda^\nu}) + \frac{1}{\lambda^\epsilon}(\frac{1}{3} - \tilde{RT}))\hat{\rho}\hat{u}_y \\ (\frac{1}{3}(\frac{1}{\lambda^\epsilon} + \frac{1}{\lambda^\nu}) + \frac{1}{\lambda^\epsilon}(\frac{1}{3} - \tilde{RT}))\hat{\rho}\hat{u}_y \end{pmatrix} \right] \end{aligned} \quad (4.44)$$

Obviously if $\tilde{RT} = \frac{1}{3}$ then some terms become zero, but if $\tilde{RT} > \frac{1}{3}$ these terms dominate. This is the source of the instability experienced at high values of \tilde{RT} , this will be seen more clearly in Equation (4.48). The momentum flux density tensor is completed by the third row of equation (4.43),

$$\tilde{\Pi}_{XY} \approx \epsilon_{Ma}^2 \hat{\rho} \hat{u}_x \hat{u}_y - \epsilon_{Ma} \epsilon_{Kn} \frac{1}{\lambda^\nu} \frac{1}{3} \left(\frac{\partial}{\partial \hat{x}} (\hat{\rho} \hat{u}_y) + \frac{\partial}{\partial \hat{y}} (\hat{\rho} \hat{u}_x) \right) \quad (4.45)$$

4.3.3 The momentum equation

Consider the second and third moment of the evolution equation, (4.40).

$$\epsilon_{Ma}\epsilon_{Kn} \frac{\partial}{\partial \hat{t}} \begin{pmatrix} \tilde{\Pi}_X \\ \tilde{\Pi}_Y \end{pmatrix} + \epsilon_{Kn} \frac{\partial}{\partial \hat{x}} \begin{pmatrix} \tilde{\Pi}_{XX} \\ \tilde{\Pi}_{XY} \end{pmatrix} + \epsilon_{Kn} \frac{\partial}{\partial \hat{y}} \begin{pmatrix} \tilde{\Pi}_{XY} \\ \tilde{\Pi}_{YY} \end{pmatrix} = \begin{pmatrix} \tilde{\lambda}^1 (\tilde{\Pi}_X^{eq} - \tilde{\Pi}_X) \\ \tilde{\lambda}^2 (\tilde{\Pi}_Y^{eq} - \tilde{\Pi}_Y) \end{pmatrix} \quad (4.46)$$

The right hand side of this equation becomes zero in all cases. Substituting the definition of the momentum flux density tensor, Equations (4.44) and (4.45) into Equation (4.46)

yields,

$$\begin{aligned}
& \epsilon_{Ma}^2 \epsilon_{Kn} \frac{\partial}{\partial \hat{t}} \begin{pmatrix} \hat{\rho} \hat{u}_x \\ \hat{\rho} \hat{u}_y \end{pmatrix} + \epsilon_{Kn} \frac{\partial}{\partial \hat{x}} \begin{pmatrix} \epsilon_{Ma}^2 (\hat{p} + \hat{\rho} \hat{u}_x^2) \\ 0 \end{pmatrix} + \epsilon_{Kn} \frac{\partial}{\partial \hat{y}} \begin{pmatrix} 0 \\ \epsilon_{Ma}^2 (\hat{p} + \hat{\rho} \hat{u}_y^2) \end{pmatrix} \\
& + \epsilon_{Kn} \frac{\partial}{\partial \hat{x}} \begin{pmatrix} -\epsilon_{Ma} \epsilon_{Kn} \left(\frac{\partial}{\partial \hat{x}} \left[\left(\frac{1}{3} \left(\frac{1}{\lambda^\xi} + \frac{1}{\lambda^\nu} \right) + \frac{1}{\lambda^\xi} \left(\frac{1}{3} - \tilde{RT} \right) \right) \hat{\rho} \hat{u}_x \right] - \frac{\partial}{\partial \hat{y}} \left[\left(\frac{1}{3} \left(\frac{1}{\lambda^\xi} - \frac{1}{\lambda^\nu} \right) + \frac{1}{\lambda^\xi} \left(\frac{1}{3} - \tilde{RT} \right) \right) \hat{\rho} \hat{u}_y \right] \right) \\ \quad \epsilon_{Ma}^2 \hat{\rho} \hat{u}_x \hat{u}_y - \epsilon_{Ma} \epsilon_{Kn} \frac{1}{3\lambda^\nu} \left(\frac{\partial}{\partial \hat{x}} (\hat{\rho} \hat{u}_y) + \frac{\partial}{\partial \hat{y}} (\hat{\rho} \hat{u}_x) \right) \end{pmatrix} \\
& + \epsilon_{Kn} \frac{\partial}{\partial \hat{y}} \begin{pmatrix} \epsilon_{Ma}^2 \hat{\rho} \hat{u}_x \hat{u}_y - \epsilon_{Ma} \epsilon_{Kn} \frac{1}{3\lambda^\nu} \left(\frac{\partial}{\partial \hat{x}} (\hat{\rho} \hat{u}_y) + \frac{\partial}{\partial \hat{y}} (\hat{\rho} \hat{u}_x) \right) \\ -\epsilon_{Ma} \epsilon_{Kn} \left(\frac{\partial}{\partial \hat{x}} \left[\left(\frac{1}{3} \left(\frac{1}{\lambda^\xi} - \frac{1}{\lambda^\nu} \right) + \frac{1}{\lambda^\xi} \left(\frac{1}{3} - \tilde{RT} \right) \right) \hat{\rho} \hat{u}_x \right] - \frac{\partial}{\partial \hat{y}} \left[\left(\frac{1}{3} \left(\frac{1}{\lambda^\xi} + \frac{1}{\lambda^\nu} \right) + \frac{1}{\lambda^\xi} \left(\frac{1}{3} - \tilde{RT} \right) \right) \hat{\rho} \hat{u}_y \right] \right) \end{pmatrix} \\
& = 0 \quad (4.47)
\end{aligned}$$

These equations can be rearranged into the standard form for the Navier-Stokes equations,

$$\begin{aligned}
& \epsilon_{Ma}^2 \epsilon_{Kn} \frac{\partial}{\partial \hat{t}} \begin{pmatrix} \hat{\rho} \hat{u}_x \\ \hat{\rho} \hat{u}_y \end{pmatrix} + \epsilon_{Ma}^2 \epsilon_{Kn} \frac{\partial}{\partial \hat{x}} \begin{pmatrix} \hat{\rho} \hat{u}_x^2 \\ \hat{\rho} \hat{u}_x \hat{u}_y \end{pmatrix} + \epsilon_{Ma}^2 \epsilon_{Kn} \frac{\partial}{\partial \hat{y}} \begin{pmatrix} \hat{\rho} \hat{u}_x \hat{u}_y \\ \hat{\rho} \hat{u}_y^2 \end{pmatrix} = \\
& - \epsilon_{Ma}^2 \epsilon_{Kn} \begin{pmatrix} \frac{\partial}{\partial \hat{x}} (\hat{p}) \\ \frac{\partial}{\partial \hat{y}} (\hat{p}) \end{pmatrix} + \epsilon_{Ma} \epsilon_{Kn}^2 \frac{\partial}{\partial \hat{x}} \begin{pmatrix} \frac{\partial}{\partial \hat{x}} \left(\frac{1}{\lambda^\xi} + \frac{1}{\lambda^\nu} \right) \frac{1}{3} \hat{\rho} \hat{u}_x + \frac{\partial}{\partial \hat{y}} \left(\frac{1}{\lambda^\xi} - \frac{1}{\lambda^\nu} \right) \frac{1}{3} \hat{\rho} \hat{u}_y \\ \frac{1}{3\lambda^\nu} \frac{\partial}{\partial \hat{x}} (\hat{\rho} \hat{u}_y) + \frac{1}{3\lambda^\nu} \frac{\partial}{\partial \hat{y}} (\hat{\rho} \hat{u}_x) \end{pmatrix} \\
& + \epsilon_{Ma} \epsilon_{Kn}^2 \frac{\partial}{\partial \hat{y}} \begin{pmatrix} \frac{1}{3\lambda^\nu} \frac{\partial}{\partial \hat{x}} (\hat{\rho} \hat{u}_y) + \frac{1}{3\lambda^\nu} \frac{\partial}{\partial \hat{y}} (\hat{\rho} \hat{u}_x) \\ \frac{\partial}{\partial \hat{x}} \left(\frac{1}{\lambda^\xi} - \frac{1}{\lambda^\nu} \right) \frac{1}{3} \hat{\rho} \hat{u}_x + \frac{\partial}{\partial \hat{y}} \left(\frac{1}{\lambda^\xi} + \frac{1}{\lambda^\nu} \right) \frac{1}{3} \hat{\rho} \hat{u}_y \end{pmatrix} \\
& + \epsilon_{Ma} \epsilon_{Kn}^2 \frac{\partial}{\partial \hat{x}} \begin{pmatrix} \frac{1}{\lambda^\xi} \left(\frac{1}{3} - \tilde{RT} \right) \left(\frac{\partial \hat{\rho} \hat{u}_x}{\partial \hat{x}} + \frac{\partial \hat{\rho} \hat{u}_y}{\partial \hat{y}} \right) \\ 0 \end{pmatrix} + \epsilon_{Ma} \epsilon_{Kn}^2 \frac{\partial}{\partial \hat{y}} \begin{pmatrix} 0 \\ \frac{1}{\lambda^\xi} \left(\frac{1}{3} - \tilde{RT} \right) \left(\frac{\partial \hat{\rho} \hat{u}_x}{\partial \hat{x}} + \frac{\partial \hat{\rho} \hat{u}_y}{\partial \hat{y}} \right) \end{pmatrix} \\
& (4.48)
\end{aligned}$$

The final terms are zero in the steady state, as can be seen when the mass conservation equation (4.20) is considered, and when $\tilde{RT} = \frac{1}{3}$. If $\tilde{RT} > \frac{1}{3}$ then these terms represent a negative bulk viscosity, and it is no surprise that this results in unstable behaviour. At

this stage these terms are removed to reveal,

$$\begin{aligned} \epsilon_{Ma}^2 \epsilon_{Kn} \left[\frac{\partial}{\partial \hat{x}} \begin{pmatrix} \hat{\rho} \hat{u}_x^2 \\ \hat{\rho} \hat{u}_x \hat{u}_y \end{pmatrix} + \frac{\partial}{\partial \hat{y}} \begin{pmatrix} \hat{\rho} \hat{u}_x \hat{u}_y \\ \hat{\rho} \hat{u}_y^2 \end{pmatrix} \right] &= -\epsilon_{Ma}^2 \epsilon_{Kn} \begin{pmatrix} \frac{\partial}{\partial \hat{x}}(\hat{p}) \\ \frac{\partial}{\partial \hat{y}}(\hat{p}) \end{pmatrix} \\ + \epsilon_{Ma} \epsilon_{Kn}^2 \left[\frac{\partial^2}{\partial \hat{x}^2} \begin{pmatrix} (\frac{1}{\lambda^\xi} + \frac{1}{\lambda^\nu}) \frac{1}{3} \hat{\rho} \hat{u}_x \\ \frac{1}{\lambda^\nu} \frac{1}{3} \hat{\rho} \hat{u}_y \end{pmatrix} + \frac{\partial^2}{\partial \hat{y}^2} \begin{pmatrix} \frac{1}{\lambda^\nu} \frac{1}{3} \hat{\rho} \hat{u}_x \\ (\frac{1}{\lambda^\xi} + \frac{1}{\lambda^\nu}) \frac{1}{3} \hat{\rho} \hat{u}_y \end{pmatrix} + \frac{\partial^2}{\partial \hat{x} \partial \hat{y}} \begin{pmatrix} \frac{1}{\lambda^\xi} \frac{1}{3} \hat{\rho} \hat{u}_y \\ \frac{1}{\lambda^\xi} \frac{1}{3} \hat{\rho} \hat{u}_x \end{pmatrix} \right] \end{aligned} \quad (4.49)$$

This equation has the same form as the compressible Navier-Stokes equation. The shear viscosity terms can be controlled by a suitable choice for λ^ν , while the bulk viscosity is controlled by λ^ξ .

The kinematic shear viscosity, ν , of the fluid is given by,

$$\tilde{\lambda}^\nu = \frac{\epsilon_{Kn}}{\epsilon_{Ma}} \frac{1}{3\hat{\nu}} = \frac{1}{3\hat{\nu}} \quad (4.50)$$

The bulk viscosity coefficient, ξ , with the same units as the kinematic viscosity, is given by,

$$\tilde{\lambda}^\xi = \frac{\epsilon_{Kn}}{\epsilon_{Ma}} \frac{1}{3\hat{\xi}} = \frac{1}{3\hat{\xi}} \quad (4.51)$$

There are several interpretations of bulk viscosity, see Dellar (2001) for details, and this definition is not regarded as standard. The relationship between Dellar's μ' (which is the same as μ_B used by Vincenti and Kruger (1976)) and ξ is $\xi\rho = \mu/3 + \mu'$. For a perfect monatomic gas $\mu' = 0$ and so $\xi = \nu/3$. It is interesting to note that the standard single relaxation time model is obtained by setting all the relaxation rates equal, including $\lambda^\nu = \lambda^\xi$ meaning $\xi = \nu$, and the Navier-Stokes equations recovered have bulk viscosity terms.

Introducing the definition of the viscosities into Equation (4.49) yields,

$$\begin{aligned} \frac{\partial}{\partial \hat{x}} \begin{pmatrix} \hat{\rho} \hat{u}_x^2 \\ \hat{\rho} \hat{u}_x \hat{u}_y \end{pmatrix} + \frac{\partial}{\partial \hat{y}} \begin{pmatrix} \hat{\rho} \hat{u}_x \hat{u}_y \\ \hat{\rho} \hat{u}_y^2 \end{pmatrix} = - \begin{pmatrix} \frac{\partial}{\partial \hat{x}}(\hat{p}) \\ \frac{\partial}{\partial \hat{y}}(\hat{p}) \end{pmatrix} + \hat{\nu} \left[\frac{\partial^2}{\partial \hat{x}^2} \begin{pmatrix} \hat{\rho} \hat{u}_x \\ \hat{\rho} \hat{u}_y \end{pmatrix} + \frac{\partial^2}{\partial \hat{y}^2} \begin{pmatrix} \hat{\rho} \hat{u}_x \\ \hat{\rho} \hat{u}_y \end{pmatrix} \right] \\ + \hat{\xi} \left[\frac{\partial^2}{\partial \hat{x}^2} \begin{pmatrix} \hat{\rho} \hat{u}_x \\ 0 \end{pmatrix} + \frac{\partial^2}{\partial \hat{y}^2} \begin{pmatrix} 0 \\ \hat{\rho} \hat{u}_y \end{pmatrix} + \frac{\partial^2}{\partial \hat{x} \partial \hat{y}} \begin{pmatrix} \hat{\rho} \hat{u}_y \\ \hat{\rho} \hat{u}_x \end{pmatrix} \right] \quad (4.52) \end{aligned}$$

4.4 Conclusions

There are 9 unique moments corresponding to the nine discrete velocities of the D2Q9 scheme. Three of the moments are the fluid density and velocity components. Another three of the moments are the components of the momentum flux density tensor. The third order moments, Π_{XXY} and Π_{XYX} , must have specific equilibrium values that yield the Navier-Stokes equations, but the non-equilibrium parts of these moments is meaningless. For the Π_{XXY} moment, the equilibrium value is selected for stability rather than hydrodynamic reasons, and the non-equilibrium part is meaningless.

A model which recovers the steady-state isothermal compressible Navier-Stokes equations was described. The use of the ideal gas equation of state means that a time accurate solution cannot be found. A restriction on the magnitude of \tilde{RT} , and thus on c , was identified from the expression for the momentum flux density tensor. The shear and bulk viscosities may be independently controlled by setting values for the relaxation frequencies λ^ν and λ^ξ respectively.

Chapter 5

Boundary Conditions and Numerical Implementation

In Chapter 4 a LB scheme was developed and analysed to show that it is equivalent to the steady-state isothermal compressible Navier-Stokes equations. Although this scheme was based on a reduced set of particle velocities, it is still a continuous scheme. To make it suitable for computation, the derivatives must be replaced by discrete approximations. In this chapter a commonly used method for an explicit second order accurate scheme will be described. Before that, a new method of analysis for boundary conditions using the moment basis, rather than the particle basis, will be introduced. This method allows analysis of commonly used boundary conditions, and will be used when new boundary conditions are developed in subsequent chapters.

All variables in Section 5.1 are in the computational scale, and for clarity the $\tilde{\cdot}$ is dropped.

5.1 Boundary conditions for LB

5.1.1 Kinetic style boundaries

Reading the literature, two clear themes come to the fore. The first is the use of kinetic style boundary conditions, such as specular, diffuse or bounce-back reflection. The motivation

for this approach is clear as these are the boundary conditions used when solving the continuous Boltzmann equation. The second theme is the use of ‘half-grid-wall’ schemes, where the location of the wall is assumed to be half way between the last and second from last row of nodes. The motivation for this approach is that the kinetic style boundaries do not work satisfactorily. Of course, in taking this approach the initial assumption that boundary conditions for the continuous Boltzmann equation can be used for LB methods is violated, but these schemes do work in some cases, as shown in Section 5.1.4.

Given the analysis of the previous chapters, it is clear that kinetic style boundaries are not appropriate for the D2Q9 system. When dealing with the 9 moment truncated system, rather than the full set of infinitely many moments, a key link with the continuous Boltzmann equation has been lost. Principally, the length of the grid spacing is much larger than the mean free path, and physical effects at a scale smaller than the hydrodynamic scale are not recreated. Therefore, the conditions at the boundary should be viewed as macroscopic, not microscopic.

5.1.2 Moment grouping

This section approaches the subject of boundary conditions from a fresh perspective, without any pretensions to replicate the full Boltzmann equation. Instead, a relatively simple problem is examined; at a straight boundary (corners are dealt with in Section 5.1.5) values for the three unknown elements of \mathbf{f} must be supplied. Therefore 3 independent equations must be identified. As the problem is expressed in terms of the hydrodynamic moments, the boundary conditions should be specified in these terms. To do this, the unknown f values must be transformed into unknown moments. For clarity two general cases, a horizontal wall and a vertical open boundary, will be considered. Of course any orientation can be analysed by application of the principles of symmetry. The horizontal wall shown in Figure 5.1a has unknown f values f_2 , f_5 and f_6 . By setting the other values of f to zero

temporarily, it can be seen how these values appear in the moment basis.

$$M \begin{pmatrix} 0 \\ 0 \\ f_2 \\ 0 \\ 0 \\ f_5 \\ 0 \\ 0 \\ f_8 \end{pmatrix} = \begin{pmatrix} f_2 + f_5 + f_6 \\ f_5 - f_6 \\ f_2 + f_5 + f_6 \\ f_5 + f_6 \\ f_2 + f_5 + f_6 \\ f_5 - f_6 \\ f_5 - f_6 \\ f_5 + f_6 \\ f_5 + f_6 \end{pmatrix} \quad \text{where} \quad \mathbf{m} = \begin{pmatrix} \Pi_0 \\ \Pi_X \\ \Pi_Y \\ \Pi_{XX} \\ \Pi_{YY} \\ \Pi_{XY} \\ \Pi_{XY} \\ \Pi_{XXY} \\ \Pi_{XXY} \end{pmatrix} \quad (5.1)$$

The unknown f values only occur in certain combinations, these combinations and their associated moments are listed in Table 5.1. Each group contains moments with the same power of x in their description,¹. For a vertical open boundary shown in Figure 5.1b with unknown f values f_1 , f_5 and f_8 the process can be repeated and Table 5.2 is obtained.

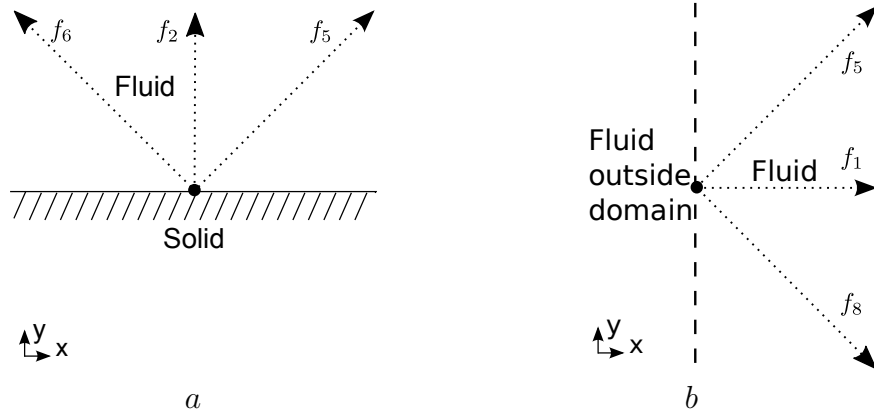


Figure 5.1: *a*: A node at a horizontal wall. *b*: A node at a vertical open boundary. The unknown f values are shown with dotted lines. f values running along the boundary are streamed from neighbouring cells.

¹Interestingly, this agrees with the theory of Torrilhon and Struchtrup (2008). They found that from their truncated 13 moment system the boundary conditions needed at the wall are all the moments with an ‘odd’ power of y ($\Pi_Y, \Pi_{XY}, \Pi_{XXY}$).

Unknowns	Moments
$f_2 + f_5 + f_6$	Π_0, Π_Y, Π_{YY}
$f_5 - f_6$	$\Pi_X, \Pi_{XY}, \Pi_{XYY}$
$f_5 + f_6$	$\Pi_{XX}, \Pi_{XXY}, \Pi_{XXYY}$

Table 5.1: Moment groups for a horizontal boundary

Unknowns	Moments
$f_1 + f_5 + f_8$	Π_0, Π_X, Π_{XX}
$f_5 - f_8$	$\Pi_Y, \Pi_{XY}, \Pi_{XXY}$
$f_5 + f_8$	$\Pi_{YY}, \Pi_{XYY}, \Pi_{XXYY}$

Table 5.2: Moment groups for a vertical boundary

For each boundary, one macroscopic variable from each group must be specified to uniquely specify the boundary condition. Specifying more than one from each group is not possible.

5.1.3 Analysis of Zou and He boundary conditions

Zou and He (1997) used a very unusual concept, ‘non-equilibrium bounce-back’, to derive a set of boundary conditions. Although the logic in the derivation is not made clear in their paper, the conditions themselves have proved to be useful. The method introduced here allows these conditions to be analysed in a more straightforward way.

The Zou and He condition for a wall boundary, when applied to a node on a wall, is equivalent to setting,

$$f_2 = f_4 \tag{5.2a}$$

$$f_5 = f_7 - \frac{1}{2} - (f_1 - f_3) + \frac{1}{2}\rho u_x \tag{5.2b}$$

$$f_6 = f_8 + \frac{1}{2} + (f_1 - f_3) - \frac{1}{2}\rho u_x \tag{5.2c}$$

In terms of moments, the Zou and He boundary becomes,

$$\mathbf{m} = \begin{pmatrix} f_0 + f_1 + 2f_4 + f_3 + 2f_7 + 2f_8 \\ \rho u_x \\ 0 \\ f_1 + f_3 + 2f_7 + 2f_8 \\ 2f_4 + 2f_7 + 2f_8 \\ \rho u_x + 2f_7 - f_1 + f_3 - 2f_8 \\ \rho u_x - f_1 + f_3 \\ 0 \\ 2f_7 + 2f_8 \end{pmatrix} \quad (5.3)$$

The only moments that do not contain references to f values are Π_X, Π_Y and Π_{XXY} . In effect, the conditions that are being applied at the wall boundary are,

$$\Pi_X = \rho u_x, \quad \Pi_Y = 0, \quad \Pi_{XXY} = \frac{1}{3}\rho u_y = 0 \quad (5.4)$$

The first two conditions contain hydrodynamic quantities and so are useful in defining the problem. The third condition, however, seems arbitrary. In the preceding derivation, setting a value for the quantity ρu_x was discussed, but for practical problems one may wish to set just the velocity. However the density, $\rho = \Pi_0$, is in the same group as Π_Y . This means that the value for ρ is already fixed as,

$$\rho = f_0 + f_1 + f_3 + 2(f_7 + f_4 + f_8) \quad (5.5)$$

This value may be used in conjunction with the desired u_x to give the desired value of Π_X .

The Zou and He condition for an open boundary is,

$$f_1 = f_3 + \frac{2}{3}\rho u_x \quad (5.6a)$$

$$f_5 = f_7 - \frac{1}{2}(f_2 - f_4) + \frac{1}{6}\rho u_x \quad (5.6b)$$

$$f_8 = f_6 + \frac{1}{2}(f_2 - f_4) + \frac{1}{6}\rho u_x \quad (5.6c)$$

Which is equivalent in moment terms to,

$$\mathbf{m} = \begin{pmatrix} f_0 + 2f_3 + \rho u_x + f_2 + f_4 + 2f_7 + 2f_6 \\ \rho u_x \\ 0 \\ 2f_3 + \rho u_x + 2f_7 + 2f_6 \\ f_2 + f_4 + 2f_7 + \frac{1}{3}\rho u_x + 2f_6 \\ 2f_7 - f_2 + f_4 - 2f_6 \\ \frac{1}{3}\rho u_x \\ -f_2 + f_4 \\ 2f_7 + \frac{1}{3}\rho u_x + 2f_6 \end{pmatrix} \quad (5.7)$$

The only moments that do not contain references to f values are Π_X, Π_Y and Π_{XY} . In effect, the conditions that are being applied at the open boundary are,

$$\Pi_X = \rho u_x, \quad \Pi_Y = 0, \quad \Pi_{XY} = \frac{1}{3}\rho u_x = \Pi_{XY}^{eq} \quad (5.8)$$

where the final relation comes from the definition of the equilibrium function, Equation (4.35). The first two conditions are desirable, as these are hydrodynamic quantities, but the final condition cannot easily be justified. The term ρu_x may be split according to the rule

$$\rho u_x = \rho - (f_0 + f_2 + f_4 + 2(f_3 + f_6 + f_7)) \quad (5.9)$$

Such that either ρ or ρu_x may be set, but not both.

5.1.4 Analysis of ‘bounce-back’, specular and diffusive boundary conditions

For completeness, the same analysis used in 5.1.3 is applied to the bounce-back boundary condition, where the unknown f values on a wall are given by,

$$f_2 = f_4, \quad f_5 = f_7, \quad f_6 = f_8 \quad (5.10)$$

Leading to the conditions in the moment basis,

$$\Pi_Y = 0, \quad \Pi_{XY Y} = 0, \quad \Pi_{XX Y} = 0 \quad (5.11)$$

Two conditions are imposed on the higher non-hydrodynamic moments, while the only hydrodynamic condition is that the flowrate through the wall is zero. The velocity along the wall is undefined, and it is this velocity that is often reported as Knudsen slip. In fact it is not, just a result of specifying the boundary conditions improperly! Nevertheless the results obtained using bounce-back are close to the correct solution, and it is worthwhile considering why this is the case. $\Pi_{XY Y}$, like the other moments, is composed of the equilibrium value plus a non-equilibrium term, $\Pi_{XY Y} = \frac{1}{3}\rho u_x + \Pi_{XY Y}^{(neq)}$. As the non-equilibrium term is small, setting $\Pi_{XY Y} = 0$ is equivalent to setting u_x to a small value. One could derive an exact expression for this value, using a method similar to the one used to obtain an expression for the non-equilibrium parts of the momentum flux density tensor. This was done by Ginzburg and Adler (1994), who then set the higher relaxation frequency to ensure zero velocity. Similarly setting $\Pi_{XX Y} = 0$ implies $\frac{1}{3}\rho u_y + \Pi_{XX Y}^{(neq)} = 0$. As $u_y = 0$, this is effectively specifying $\Pi_{XX Y}^{(neq)} = 0$. Those who defend bounce-back would argue that it is quick to implement. However, for many people the time saved using bounce-back was subsequently wasted analysing the slip velocity it creates (see Verhaeghe et al. (2009) again).

The same analysis applied to specular reflection, defined by;

$$f_2 = f_4, \quad f_5 = f_8, \quad f_6 = f_7 \quad (5.12)$$

results in the following moment conditions,

$$\Pi_Y = 0, \quad \Pi_{XY} = 0, \quad \Pi_{XXY} = 0 \quad (5.13)$$

Again, these are a fairly arbitrary set of constraints. As there is no longer the constraint that $\Pi_{XY} = 0$, the velocity at the wall is not set to zero, or even a value close to zero. Instead, the conditions $\Pi_{XY} = \Pi_Y = 0$ lead to the viscous shear stress being set to zero, which is effectively setting $\partial u_x / \partial y = 0$. In channel flow this leads to the x velocity at the wall being the same as the velocity along the centre of the channel. As with bounce-back, setting $\Pi_{XXY} = 0$ is equivalent to $\Pi_{XXY}^{(neg)} = 0$, and it is not clear if this has any impact on the solution.

A diffusive reflection boundary condition, a LB version of Maxwell's boundary condition for the continuum Boltzmann equation, is proposed by many authors, including Verhaeghe et al. (2009) and Sofonea and Sekerka (2005a). The various schemes for implementing diffusive reflection all start from arbitrary constraints in the particle basis, and when viewed in the moment basis simply reveal different arbitrary constraints. The details are therefore omitted from this work. Verhaeghe et al. (2009) and Guo et al. (2009) suggest combining the diffusive reflection boundary condition with either the bounce-back or specular reflection boundary condition. By specifying how much of one or the other condition is used some control is possible over some of the moments, such as the slip velocity. However, this seems an unnecessarily complicated and less effective way of achieving what is described in this work.

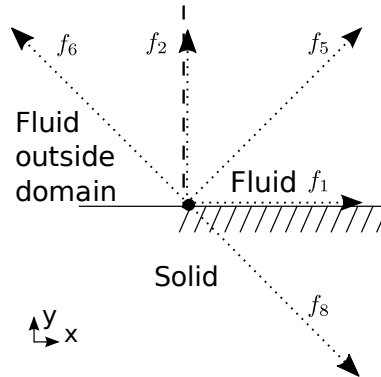


Figure 5.2: A concave corner node. The unknown f values are shown with dotted lines. The dashed line is the open boundary, the solid line is the wall.

5.1.5 Treatment of corner nodes

At this stage it is worth mentioning the treatment of corners. The literature on LB hardly touches on the issue, yet simulations show that the treatment is absolutely essential for a well-behaved solution. The idea of studying boundaries in the moment basis can be used to suggest an extension of the Zou and He boundary conditions to include corners. However, this is not satisfactory and a better solution will be proposed later.

Corner nodes can be divided into two types, concave and convex corners. A concave corner is such that a fluid node is surrounded by five solid nodes, such that there are five unknown values of f . A convex corner has only one solid node as a neighbour, and as such is, in most cases, a trivial problem.

As an example consider the concave corner shown in Figure 5.2 with unknown f values f_1 , f_2 , f_5 , f_7 and f_8 . Substituting zero for the known f values into the moment equation

gives:

$$M \begin{pmatrix} 0 \\ f_1 \\ f_2 \\ 0 \\ 0 \\ f_5 \\ 0 \\ f_7 \\ f_8 \end{pmatrix} = \begin{pmatrix} f_1 + f_2 + f_5 + f_7 + f_8 \\ f_1 + f_5 - f_7 + f_8 \\ f_2 + f_5 - f_7 - f_8 \\ f_1 + f_5 + f_7 + f_8 \\ f_2 + f_5 + f_7 + f_8 \\ f_5 + f_7 - f_8 \\ f_5 - f_7 + f_8 \\ f_5 - f_7 - f_8 \\ f_5 + f_7 + f_8 \end{pmatrix} \quad \mathbf{m} = \begin{pmatrix} \Pi_0 \\ \Pi_X \\ \Pi_Y \\ \Pi_{XX} \\ \Pi_{YY} \\ \Pi_{XY} \\ \Pi_{XY} \\ \Pi_{XXY} \\ \Pi_{XXY} \end{pmatrix} \quad (5.14)$$

The moments are not as neatly arranged in groups as they were for straight boundaries. Obviously the moments are not fully independent, only five may be given values, however there is some freedom as to which five are selected.

For example, for a corner which forms the intersection between a wall and an open boundary enforced using the Zou and He method, Equations (5.2) and (5.6), one could apply the conditions of both, giving,

$$\Pi_0 = \rho_{open} \quad (5.15)$$

$$\Pi_X = \rho_{open} u_x \quad (5.16)$$

$$\Pi_Y = 0 \quad (5.17)$$

$$\Pi_{XY} = \frac{1}{3} \rho u_x = \Pi_{XY}^{eq} \quad (5.18)$$

$$\Pi_{XXY} = 0 \quad (5.19)$$

These conditions in moment space lead to the following f values:

$$f_1 = f_3 + \frac{2}{3}\rho_{open}u_x \quad (5.20a)$$

$$f_2 = f_4 \quad (5.20b)$$

$$f_5 = f_7 + \frac{1}{6}\rho_{open}u_x \quad (5.20c)$$

$$f_6 = -\frac{1}{2}f_0 - f_3 - f_4 - f_7 + \frac{1}{2}\rho_{open} - \frac{1}{2}\rho_{open}u_x \quad (5.20d)$$

$$f_8 = -\frac{1}{2}f_0 - f_3 - f_4 - f_7 + \frac{1}{2}\rho_{open} - \frac{1}{3}\rho_{open}u_x \quad (5.20e)$$

To summarise, this is not the recommended solution to the corner nodes, but a method for corners that is consistent with the Zou and He open and wall boundary conditions.

To demonstrate the effect of changing the corner nodes, two different boundary conditions were applied to the corner nodes of a simulation of Poiseuille flow in a channel. For both simulations the boundary at the wall was enforced using bounce back, and the inlet and outlet using the Zou and He conditions. Firstly, the Zou and He open boundary condition (Equation (5.6)) and then the bounce-back rule (Equation (5.10)) were applied to the corner nodes, and the result is shown in Figure 5.3. Secondly, the improved treatment described here (Equation (5.20)) was applied, with zero slip velocity, and the results are shown in Figure 5.4. It is clear that using the moment basis to apply consistent conditions at the corner greatly improves the accuracy of the solution, the error is one thousand times smaller in the corner. However, a better solution for Poiseuille flow is proposed in Chapter 6.

5.2 Numerical implementation

To convert the PDEs described in Chapter 4 into a numerical scheme, a first-order accurate Forward-Euler scheme is used. This scheme has the advantage of being explicit, but has low accuracy. Following the approach of many authors, including Chen and Doolen (1998), a modified collision term is introduced which makes the scheme second-order accurate.

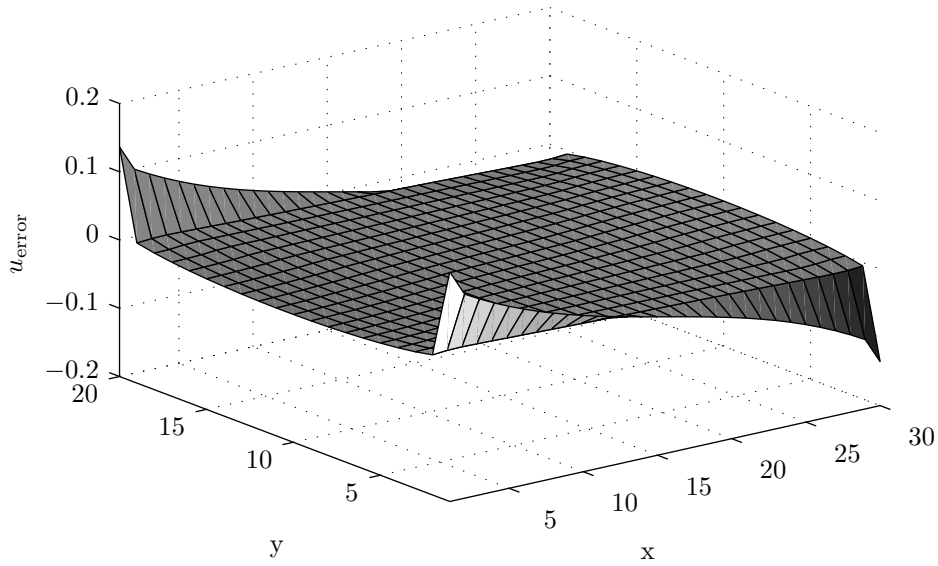


Figure 5.3: u_{error} is the difference between the velocity calculated and the analytical solution for Poiseuille flow. The wall follows the lines $y = 1$ and $y = 20$. The corner nodes have the Zou and He conditions for an open boundary, followed by the application of the bounce-back rule. The corner nodes clearly cause a large error.

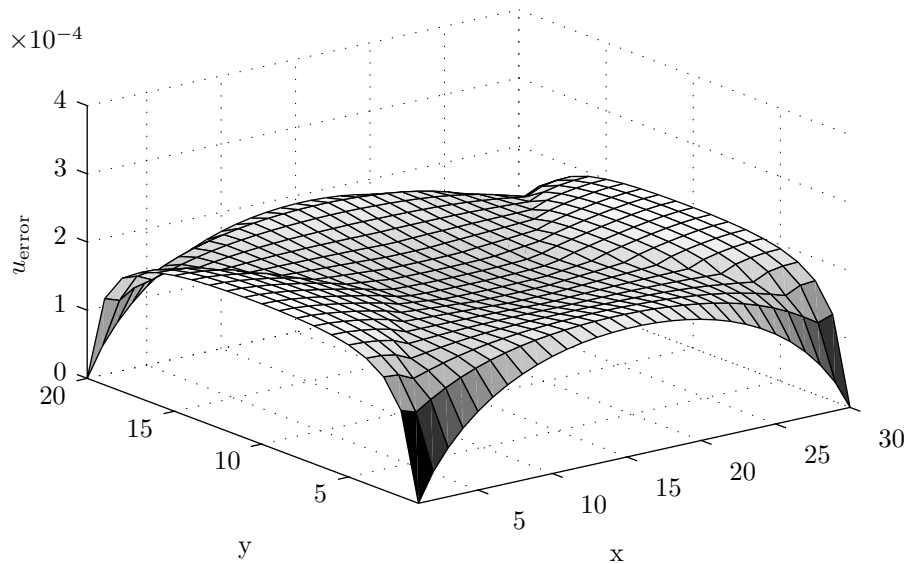


Figure 5.4: u_{error} is the difference between the velocity recovered and the analytical solution. The wall follows the lines $y = 1$ and $y = 20$. The corner nodes have the conditions described in Equation (5.20) imposed. The corner nodes cause a small disturbance to the whole domain

Introducing \tilde{f}^+ to represent $\tilde{f}(\tilde{x} + 1, \tilde{y} + 1, \tilde{t} + 1)$, that is after collision and streaming, the forward Euler scheme can be written as,

$$\tilde{\mathbf{f}}^+ = \tilde{\mathbf{f}} + \tilde{M}^{-1} \tilde{\Lambda}' \tilde{M} (\tilde{\mathbf{f}}^{(eq)} - \tilde{\mathbf{f}}) \quad (5.21)$$

Where the prime superscript ($'$) in $\tilde{\Lambda}'$ indicates that a correction for numerical errors has been included. If $\tilde{\Lambda}' = \tilde{\Lambda}$ this scheme would only be first-order accurate in space. Taking moments of Equation (5.21), and picking the XX component of the momentum flux density tensor evolution equation (as an example), gives,

$$\tilde{\Pi}_{XX}^+ - \tilde{\Pi}_{XX} = \frac{\tilde{\lambda}^{\nu'} + \tilde{\lambda}^{\xi'}}{2} (\tilde{\Pi}_{XX}^{(eq)} - \tilde{\Pi}_{XX}) + \frac{\tilde{\lambda}^{\nu'} - \tilde{\lambda}^{\xi'}}{2} (\tilde{\Pi}_{YY}^{(eq)} - \tilde{\Pi}_{YY}) \quad (5.22)$$

A similar equation can be derived using a second order accurate central-differencing method, such as,

$$\begin{aligned} (\tilde{\Pi}_{XX}^+ - \tilde{\Pi}_{XX}) = \frac{1}{2} \left[\frac{\tilde{\lambda}^{\nu} + \tilde{\lambda}^{\xi}}{2} \left((\tilde{\Pi}_{XX}^{(eq)} - \tilde{\Pi}_{XX}) + (\tilde{\Pi}_{XX}^{(eq)+} - \tilde{\Pi}_{XX}^+) \right) \right. \\ \left. + \frac{\tilde{\lambda}^{\nu} - \tilde{\lambda}^{\xi}}{2} \left((\tilde{\Pi}_{YY}^{(eq)} - \tilde{\Pi}_{YY}) + (\tilde{\Pi}_{YY}^{(eq)+} - \tilde{\Pi}_{YY}^+) \right) \right] \quad (5.23) \end{aligned}$$

Now, assuming $\Pi_{\alpha\alpha}^{(eq)+} = \Pi_{\alpha\alpha}^{(eq)}$ (where no summation on α is implied), as $\Pi_{\alpha\alpha}^{(eq)+}$ is unknown at the beginning of the time step, the central differencing method becomes,

$$\begin{aligned} (\tilde{\Pi}_{XX}^+ - \tilde{\Pi}_{XX}) \left(1 + \frac{\tilde{\lambda}^{\nu} + \tilde{\lambda}^{\xi}}{4} \right) = \frac{\tilde{\lambda}^{\nu} + \tilde{\lambda}^{\xi}}{2} (\tilde{\Pi}_{XX}^{(eq)} - \tilde{\Pi}_{XX}) \\ + \frac{\tilde{\lambda}^{\nu} - \tilde{\lambda}^{\xi}}{2} (\tilde{\Pi}_{YY}^{(eq)} - \tilde{\Pi}_{YY}) - \frac{\tilde{\lambda}^{\nu} - \tilde{\lambda}^{\xi}}{4} (\tilde{\Pi}_{YY}^+ - \tilde{\Pi}_{YY}) \quad (5.24) \end{aligned}$$

There is a similar equation which can be derived by repeating the above steps with the YY component of the momentum flux density tensor, and this must be used to remove the dependence on $(\tilde{\Pi}_{YY}^+ - \tilde{\Pi}_{YY})$. After some algebra, these two equations may be written in

the form of Equation (5.22),

$$\begin{aligned}
(\tilde{\Pi}_{XX}^+ - \tilde{\Pi}_{XX}) &= 2 \frac{\tilde{\lambda}^\nu + \tilde{\lambda}^\xi + \tilde{\lambda}^\nu \tilde{\lambda}^\xi}{(\tilde{\lambda}^\nu + 2) + (\tilde{\lambda}^\xi + 2)} (\tilde{\Pi}_{XX}^{(eq)} - \tilde{\Pi}_{XX}) \\
&\quad - \frac{2\tilde{\lambda}^\nu - 2\tilde{\lambda}^\xi}{(\tilde{\lambda}^\nu + 2) + (\tilde{\lambda}^\xi + 2)} (\tilde{\Pi}_{YY}^{(eq)} - \tilde{\Pi}_{YY}) \quad (5.25)
\end{aligned}$$

For this equation to describe the same scheme as Equation (5.22) the modified collision times must be,

$$\tilde{\lambda}^{\nu'} = \frac{\tilde{\lambda}^\nu}{(1 + \frac{\tilde{\lambda}^\nu}{2})}, \quad \tilde{\lambda}^{\xi'} = \frac{\tilde{\lambda}^\xi}{(1 + \frac{\tilde{\lambda}^\xi}{2})} \quad (5.26)$$

Chapter 6

Solution of Poiseuille Flow

A LB model for single component flow was developed in Chapter 4, and a method for analysing and creating boundary conditions was developed in Chapter 5. These will now be used to model Poiseuille flow. The boundary conditions for Poiseuille flow will be determined from the analytical solution. Non-dimensional results are included to show the limits of the model, however the section of greatest interest is the solution to a real physical problem. This is rarely (maybe never) done in the literature, especially for a gas obeying the Ideal Gas law.

6.1 Theoretical solution

Before attempting to compute a solution to Poiseuille flow it is informative to recover the well known analytical solution from the LB model. The Poiseuille problem is flow through a channel driven by a pressure gradient in the x direction, with zero velocity at the wall (although a slip velocity is carried through the algebra for generality). The following conditions are met,

$$\hat{u}_y = 0 \qquad \frac{\partial \hat{\rho}}{\partial \hat{y}} = 0 \qquad \frac{\partial \hat{p}}{\partial \hat{y}} = 0 \qquad \frac{\partial}{\partial \hat{t}} = 0 \qquad (6.1)$$

Introducing these simplifications into the mass conservation equation, (4.20), yields

$$\frac{\partial(\hat{\rho}\hat{u}_x)}{\partial\hat{x}} = -\frac{\partial(\hat{\rho}\hat{u}_y)}{\partial\hat{y}} = 0 \quad (6.2)$$

The terms are equal to zero because the y velocity is zero everywhere. Given these conditions the momentum flux density tensor, Equation (4.44) and Equation (4.45) becomes:

$$\tilde{\Pi}_{XX} = \epsilon_{Ma}^2(\hat{p} + \hat{\rho}\hat{u}_x^2) \quad (6.3a)$$

$$\tilde{\Pi}_{YY} = \epsilon_{Ma}^2\hat{p} \quad (6.3b)$$

$$\tilde{\Pi}_{XY} = -\epsilon_{Ma}^2\hat{\nu}\left(\frac{\partial\hat{\rho}\hat{u}_x}{\partial\hat{y}}\right) \quad (6.3c)$$

The momentum equation (4.46) becomes,

$$\frac{\partial}{\partial\hat{x}} \begin{pmatrix} \tilde{\Pi}_{XX} \\ \tilde{\Pi}_{XY} \end{pmatrix} = -\frac{\partial}{\partial\hat{y}} \begin{pmatrix} \tilde{\Pi}_{XY} \\ \tilde{\Pi}_{YY} \end{pmatrix} \quad (6.4)$$

Into which the values of the momentum flux density tensor given by Equations (6.3) can be substituted to obtain,

$$\frac{\partial}{\partial\hat{x}} \begin{pmatrix} \hat{p} + \hat{\rho}\hat{u}_x^2 \\ -\hat{\nu}\left(\frac{\partial\hat{\rho}\hat{u}_x}{\partial\hat{y}}\right) \end{pmatrix} = -\frac{\partial}{\partial\hat{y}} \begin{pmatrix} -\hat{\nu}\left(\frac{\partial\hat{\rho}\hat{u}_x}{\partial\hat{y}}\right) \\ \hat{p} \end{pmatrix} \quad (6.5)$$

With the use of the identities,

$$\frac{\partial\hat{\rho}\hat{u}_x^2}{\partial\hat{x}} = 2\hat{u}_x\frac{\partial\hat{\rho}\hat{u}_x}{\partial\hat{x}} - \hat{u}_x^2\frac{\partial\hat{\rho}}{\partial\hat{x}} = 0 - \hat{u}_x^2\frac{\partial\hat{\rho}}{\partial\hat{x}} \quad (6.6)$$

$$\frac{\partial}{\partial\hat{x}}\frac{\partial\hat{\rho}\hat{u}_x}{\partial\hat{y}} = \frac{\partial}{\partial\hat{y}}\frac{\partial\hat{\rho}\hat{u}_x}{\partial\hat{x}} = 0 \quad (6.7)$$

$$\frac{\partial}{\partial\hat{y}}(\hat{p}) = 0 \quad (6.8)$$

the second row of (6.5) becomes zero, while the first row becomes,

$$\frac{\partial \hat{p}}{\partial \hat{x}} - \hat{u}_x^2 \frac{\partial \hat{\rho}}{\partial \hat{x}} = \frac{\partial \hat{p}}{\partial \hat{x}} \left(1 - \frac{\hat{u}_x^2}{\hat{R}T} \right) = \hat{\nu} \left(\frac{\partial^2 \hat{\rho} \hat{u}_x}{\partial \hat{y}^2} \right) \quad (6.9)$$

where the second term was obtained by using the Ideal Gas equation. As the physical problems which will be considered are low Mach number, $\hat{u}_x^2 \ll \hat{R}T$ and $(1 - \frac{\hat{u}_x^2}{\hat{R}T}) \approx 1$, this is easily confused with the incompressible limit, and it is worth clarifying what is being limited. The assumption is that $\sqrt{\hat{R}T}$ is much greater than the mean speed of the flow, u_x . The density is not constant but changes in the density will be $1/\hat{R}T$ times changes in pressure, and therefore they will be very small. However, the relative change in pressure and density are the same size, $\Delta p/p = \Delta \rho/\rho$.

Integrating equation (6.9) with respect to \hat{y} then setting boundary conditions of zero x velocity at $\hat{y} = \pm \hat{H}/2$, where H is the channel width, gives,

$$\hat{u}_x = \frac{1}{2\hat{\rho}\hat{\nu}} \frac{\partial \hat{p}}{\partial \hat{x}} \left(\hat{y}^2 - (\hat{H}/2)^2 \right) \quad (6.10)$$

This is in agreement with the usual theoretical solution of the Poiseuille flow.

6.1.1 Moment based boundary conditions for Poiseuille Flow

Using the analytical solution of the Poiseuille flow, one can see that the higher order moments, Π_{XXY} , Π_{XYX} and Π_{XYY} , are not needed in order to recover the correct velocity profile. Therefore, using these moments in boundary conditions, as existing methods such as bounce-back do, may introduce an error. An approach using only the lower moments, as in the analytical solution, is now explored. Considering the grouping of moments at a

wall, Table 5.1, one possible combination is,

$$\tilde{\Pi}_Y = 0 \quad (6.11)$$

$$\tilde{\Pi}_X = \tilde{\rho}\tilde{u}_{slip} \quad (6.12)$$

$$\tilde{\Pi}_{XX} = \tilde{p} + \tilde{\rho}\tilde{u}_{slip}^2 \quad (6.13)$$

For the sake of generality a slip velocity along the wall is included. An expression for the pressure, \hat{p} , is required, however. Remembering that the value of $\tilde{\rho}$ can be calculated from the known f values, \hat{p} can be calculated using the equation of state, giving

$$\tilde{\Pi}_{XX} = \tilde{p} + \tilde{\rho}\tilde{u}_{slip}^2 = \tilde{\rho}(\tilde{R}\tilde{T} + \tilde{u}_{slip}^2) \quad (6.14)$$

At an open boundary the moments to be set are,

$$\tilde{\Pi}_0 = \tilde{\rho}_{open} \quad (6.15)$$

$$\tilde{\Pi}_Y = 0 \quad (6.16)$$

$$\tilde{\Pi}_{YY} = \tilde{p}_{open} = \tilde{R}\tilde{T}\tilde{\rho}_{open} \quad (6.17)$$

At a corner all these conditions are imposed simultaneously,

$$\tilde{\Pi}_0 = \tilde{\rho}_{open} \quad (6.18)$$

$$\tilde{\Pi}_X = \tilde{\rho}_{open}\tilde{u}_{slip} \quad (6.19)$$

$$\tilde{\Pi}_Y = 0 \quad (6.20)$$

$$\tilde{\Pi}_{XX} = \tilde{\rho}_{open}(\tilde{R}\tilde{T} + \tilde{u}_{slip}^2) \quad (6.21)$$

$$\tilde{\Pi}_{YY} = \tilde{R}\tilde{T}\tilde{\rho}_{open} \quad (6.22)$$

A summary of these conditions is shown in Figure 6.1. Using them the unknown f values can be recovered. At a wall they are,

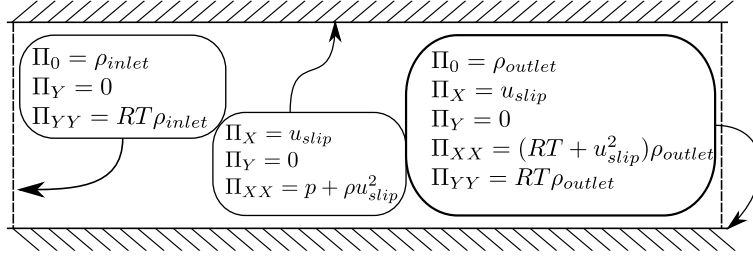


Figure 6.1: Boundary conditions for Poiseuille flow

$$\tilde{f}_2 = \tilde{f}_1 + \tilde{f}_3 + \tilde{f}_4 + 2\tilde{f}_7 + 2\tilde{f}_8 - (\tilde{R}T + \tilde{u}_x^2)\tilde{\rho} \quad (6.23a)$$

$$\tilde{f}_5 = -\tilde{f}_1 - \tilde{f}_8 + \frac{\tilde{u}_x\tilde{\rho}}{2} + \frac{1}{2}(\tilde{R}T + \tilde{u}_x^2)\tilde{\rho} \quad (6.23b)$$

$$\tilde{f}_6 = -\tilde{f}_3 - \tilde{f}_7 - \frac{\tilde{u}_x\tilde{\rho}}{2} + \frac{1}{2}(\tilde{R}T + \tilde{u}_x^2)\tilde{\rho} \quad (6.23c)$$

at an open boundary,

$$\tilde{f}_1 = -\tilde{f}_0 - \tilde{f}_3 + \tilde{\rho} - \tilde{R}T\tilde{\rho} \quad (6.24a)$$

$$\tilde{f}_5 = -\tilde{f}_2 - \tilde{f}_6 + \frac{1}{2}\tilde{R}T\tilde{\rho} \quad (6.24b)$$

$$\tilde{f}_8 = -\tilde{f}_4 - \tilde{f}_7 + \frac{1}{2}\tilde{R}T\tilde{\rho} \quad (6.24c)$$

and at the intersection of a wall and open boundary,

$$\tilde{f}_1 = -\tilde{f}_0 - \tilde{f}_3 + \tilde{\rho} - \tilde{R}T\tilde{\rho} \quad (6.25a)$$

$$\tilde{f}_2 = -\tilde{f}_0 - \tilde{f}_4 + \tilde{\rho} - (\tilde{R}T + \tilde{u}_x^2)\tilde{\rho} \quad (6.25b)$$

$$\tilde{f}_5 = \frac{1}{2}(-\tilde{f}_1 - \tilde{f}_2 + \tilde{f}_3 + \tilde{f}_4) + \tilde{f}_7 + \frac{1}{2}\tilde{\rho}\tilde{u}_x \quad (6.25c)$$

$$\tilde{f}_6 = \frac{1}{2}(-\tilde{f}_0 - \tilde{f}_2 - \tilde{f}_4) - \tilde{f}_3 - \tilde{f}_7 + \frac{1}{2}\tilde{\rho} - \tilde{u}_x\tilde{\rho} \quad (6.25d)$$

$$\tilde{f}_8 = -\tilde{f}_0 - \tilde{f}_1 - \tilde{f}_2 - \tilde{f}_3 - \tilde{f}_4 - \tilde{f}_5 - \tilde{f}_6 - \tilde{f}_7 + \tilde{\rho} \quad (6.25e)$$

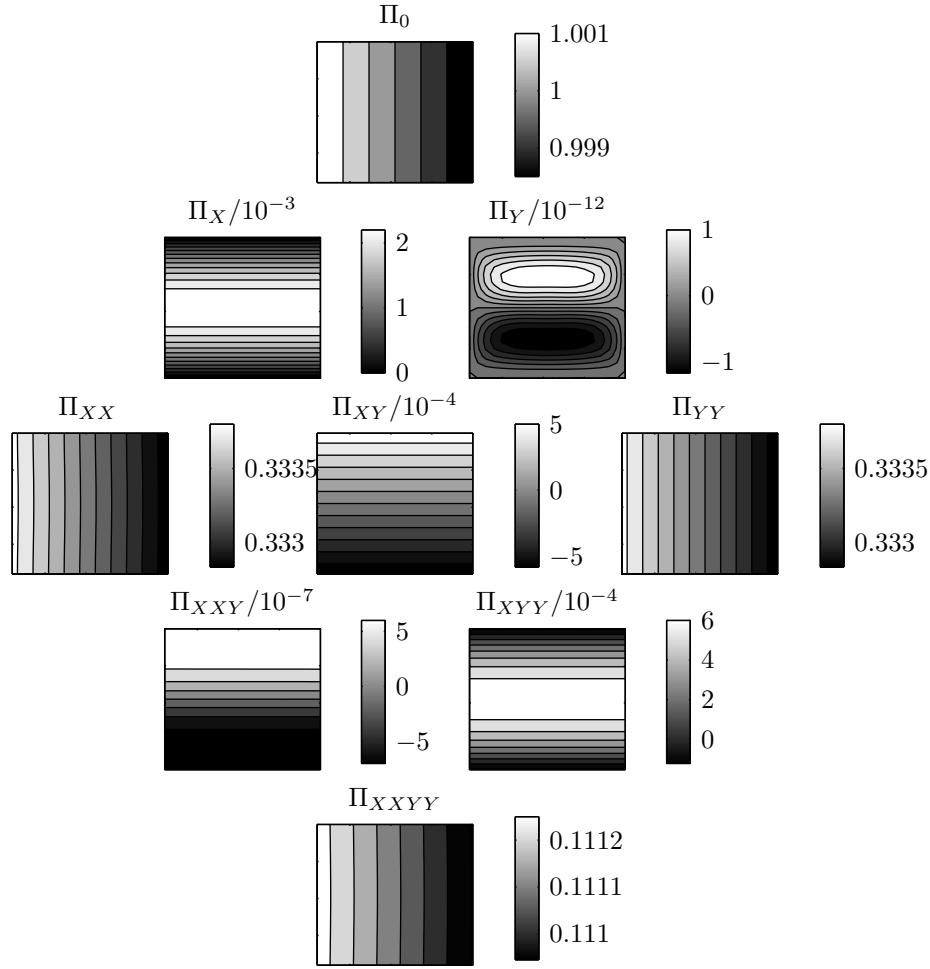


Figure 6.2: Moments for a solution to the Poiseuille flow arranged according to their order in Table 4.1. A 20×20 grid was used, the pressure drop was 1×10^{-3} , $\tilde{R}T = 1/3$ and $\tilde{\nu} = 1$. The moments near the bottom are higher order. Non-dimensional units.

6.2 Non-dimensional results for Poiseuille flow

In this section results from a simple non-dimensional Poiseuille flow are presented. Poiseuille flow is particularly simple, and the stability and accuracy demonstrated here will be far higher than could be expected in a more complicated geometry. Unless otherwise stated, all results in this section are of a solution that has converged, defined by the change in total momentum throughout the domain from one time step to the next being zero to machine accuracy. The geometry is a 20×20 grid, with the pressure imposed on both ends using the method from Section 6.1.1. The accuracy will be measured as the percentage error in the

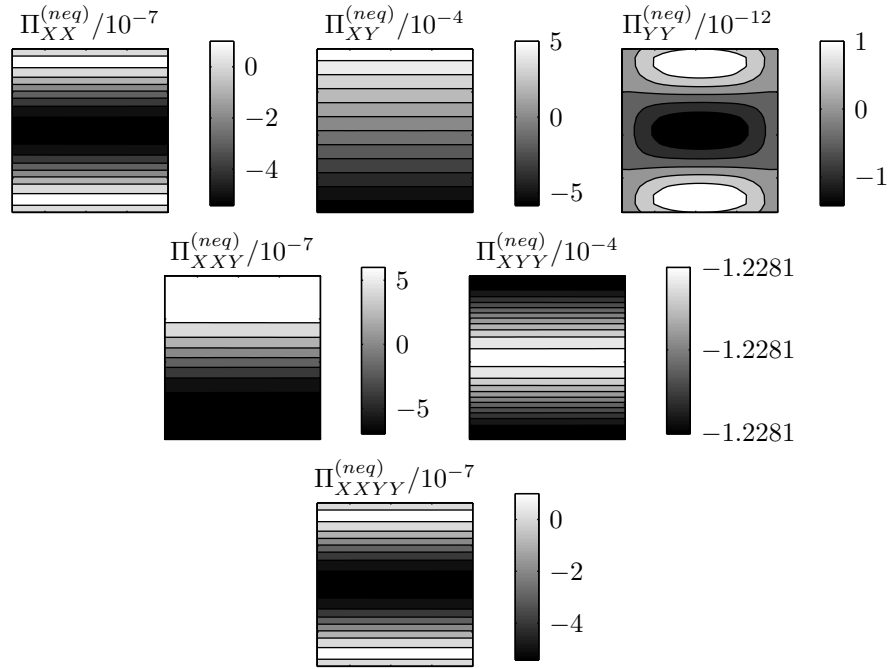


Figure 6.3: Non-equilibrium part of moments, or the difference between the equilibrium values and the actual moments, shown in Figure 6.2. The non-equilibrium part of the conserved moments is zero, and not shown. Non-dimensional units.

cross-channel average velocity half way along the channel compared with the theoretical solution.

Figure 6.2 shows contours for all the moments, for a typical computation of Poiseuille flow. It is informative to study carefully the shape of these contours, and compare them with the equilibrium values; the difference between the two is shown in Figure 6.3. The density and x momentum behave as the theoretical solution predicts. The y velocity is interesting, it is small, but there is obviously a pattern to it. This is because of the compressible nature of the solution. At lower values of x velocity, the y velocity becomes too small to resolve and this pattern disappears.

The YY component of the momentum flux density tensor is very close to its equilibrium values, however the equilibrium values of the XY momentum flux is effectively zero, and so the non-equilibrium value is very substantial. As is to be expected, the XX viscous stress is smaller than the XY viscous stress, and is constant along lines of constant y .

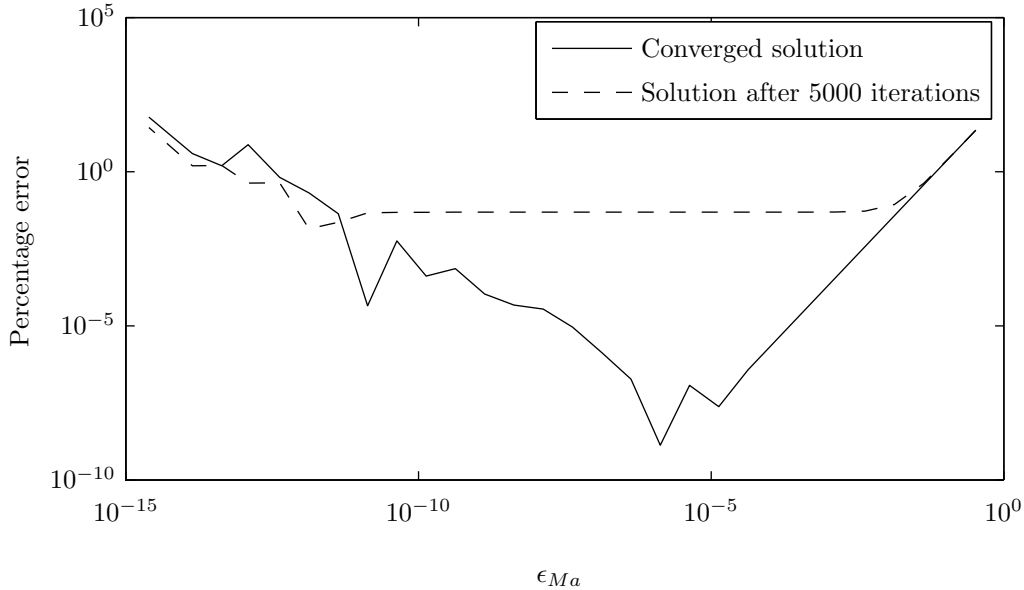


Figure 6.4: Percentage error of average velocity mid-way along the channel compared with theoretical solution for Poiseuille flow. The pressure difference driving the flow was varied to give different values of ϵ_{Ma}

The first test conducted was to vary the overall pressure difference in order to change the maximum velocity. The value of \tilde{RT} was $1/3$, the average scaled pressure was $1/3$ and all relaxation frequencies were set to 1.5 . Results are shown in Figure 6.4 for solutions which were fully converged, and for solutions after 5,000 iterations. Looking at the converged solutions, clearly the magnitude of ϵ_{Ma} has an impact on the accuracy, if it is too high there is an error due to compressibility effects, and if it is too low the limited numerical range of the computer introduces an error. There is a range where the accuracy is acceptable. Within this range the number of iterations to convergence tends to reduce with lower values of ϵ_{Ma} . After 5,000 iterations the main source of error is due to the time dependent nature of the solution, and this error is roughly independent of ϵ_{Ma} .

The effect of changing the value of \tilde{RT} was also investigated and the results are shown in Figure 6.5. Again the average scaled pressure was $1/3$ and all relaxation frequencies were set to 1.5 . The pressure gradient was varied to find the maximum stable value of ϵ_{Ma} . The definition of ‘stable’ is not exact, as the error is high with large ϵ_{Ma} values, and therefore these results are only approximate. Values of \tilde{RT} above $1/2$ are not stable. The

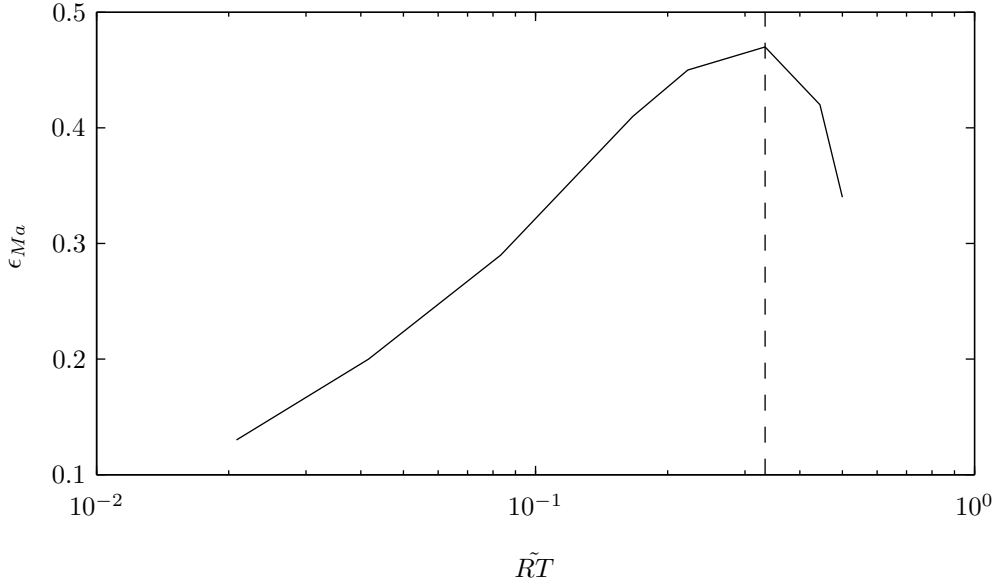


Figure 6.5: Maximum stable value of ϵ_{Ma} at different values of (\tilde{RT}) . The dashed vertical line shows $(\tilde{RT}) = 1/3$

results in Figure 6.5 are clear, there is maximum stability when $\tilde{RT} = 1/3$. This agrees with the conclusions reached in Section 4.3.2. For constant values of ϵ_{Ma} the accuracy increases with small values of \tilde{RT} , as long as it remains stable, as the change in density is smaller and thus the compressibility effect is less.

Figure 6.6 shows the result of changing all the relaxation times together, within the range of stable values from 0.2 to 1.5, which corresponds to viscosities of 1.5 to 0.06. Everything else was held constant. The accuracy improves with smaller values of $\tilde{\lambda}$, however ϵ_{Ma} also decreases, and it is not clear if this is the source of the improvement in accuracy.

Figure 6.7 shows the range of stability for λ^ξ , at different values of all the other relaxation frequencies (where $\lambda^8 = \lambda^7 = \lambda^6 = \lambda^\nu$). The lowest value of λ^ξ which is stable is 0.35 times λ^ν , and therefore bulk viscosity effects will always be present in any solution. If the Vincenti and Kruger (1976) definition of bulk viscosity is used, obtained by setting $\lambda^\nu = \lambda^\xi/3$ as discussed in the text following Equation (4.51), the model is not stable for zero bulk viscosity.

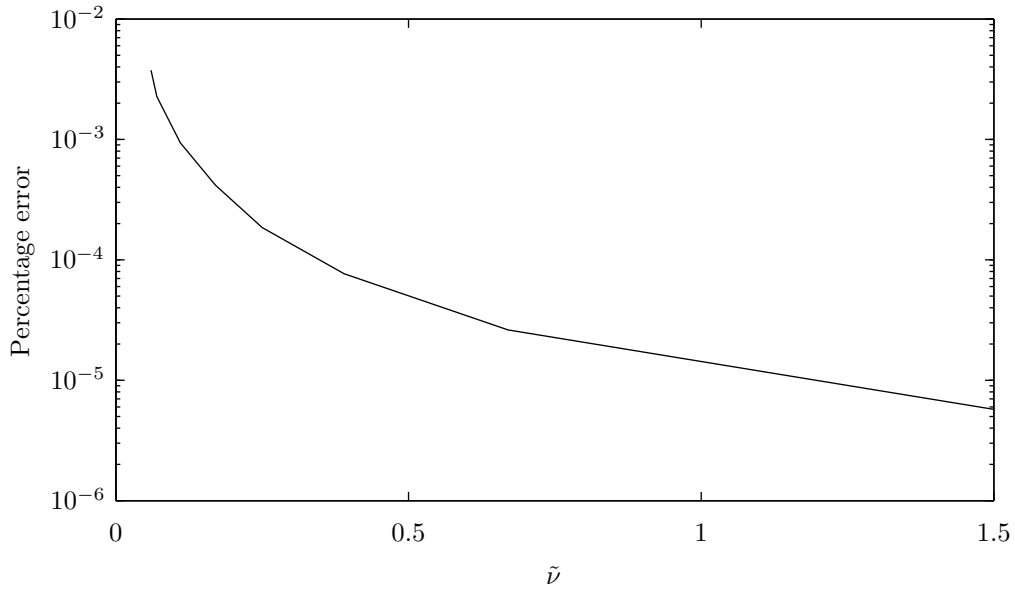


Figure 6.6: Percentage error at different values of viscosity. Pressure difference driving the flow, in non-dimensional units, is 10^{-4} .

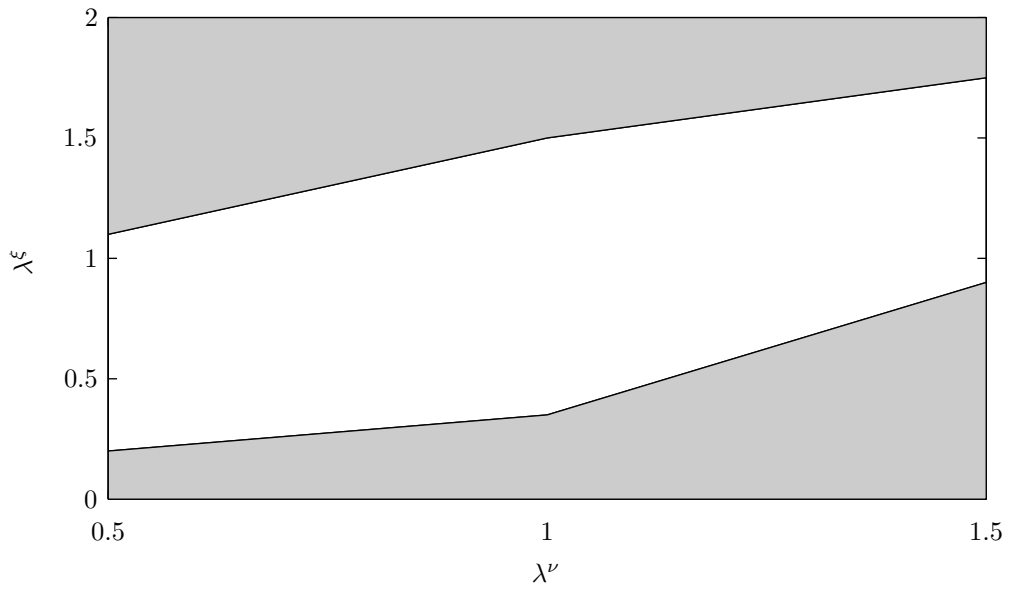


Figure 6.7: The white region represents stable values of $\tilde{\lambda}^\xi$ at different values of $\tilde{\lambda}^\nu$. The pressure difference driving the flow is 10^{-4} in non-dimensional units.

Channel Length (L)	1×10^{-5} m
Channel Height (H)	1×10^{-5} m
Average Pressure	1×10^5 Pa
Total Pressure drop	10 Pa
Temperature (T)	300 K
Gas Constant (R)	4157 J kmol^{-1}
Viscosity of Hydrogen (at 25°C) (μ)	$8.81 \times 10^{-6} \text{ kg m}^{-1} \text{ s}^{-1}$

Table 6.1: Parameters for dimensional Poiseuille problem

6.2.1 Higher moment relaxation frequencies

Changing λ^6 and λ^7 has very little effect on the results. In fact, it is only when these relaxation frequencies are very small that they reduce the accuracy of the solution. There is a stability limit on high and low values of λ^6 and λ^7 but, as these relaxation frequencies play no part in the hydrodynamic equations, avoiding unstable values is easy.

Changes in λ^8 produce an extremely small change in the accuracy of the solution. For quite a wide range of values of λ^ν , λ^8 can be set to zero without affecting accuracy, for values of λ^ν outside this range λ^8 has a stability boundary at a very small number. For all values of λ^ν , λ^8 has a stability boundary at high values. Typically λ^8 cannot be more than $3/2$ times λ^ν .

In view of this situation, it seems that setting $\lambda^6 = \lambda^7 = \lambda^8 = \lambda^\nu$ is the best first approximation. If different values are required, care should be taken, when working on dimensional problems, that the value of the higher relaxation frequencies are set in the fluid dynamic scale, not the computational scale, as discussed by Dellar (2003).

6.3 A dimensional problem

It is useful to examine a dimensional problem, to clarify the accuracy which might be expected from this method. Poiseuille flow of hydrogen was simulated, with the parameters shown in Table 6.3. The analytical solution is obtained by integrating Equation (6.10).

c	N_x		
	30	60	90
1300	-0.9427	-0.9434	-0.9436
2000	-0.9427	-0.9434	-0.9436
3000	-0.9427	-0.9434	-0.9436
4000	-0.9427	-0.9434	-0.9436

Table 6.2: Channel-averaged x velocity obtained from simulations [m/s]

N_x		
30	60	90
0.9448	0.9456	0.9458

Table 6.3: Average x velocity (\bar{u}_x) obtained from trapezoidal integration of the analytical solution, Equation (6.10), [m/s]

$$\bar{u}_x = \frac{H^2}{\mu 12} \frac{dp}{dx} = 0.94589 \text{ m/s} \quad (6.26)$$

Where \bar{u} is the cross-channel averaged velocity in the x direction. As $u_x \ll \sqrt{RT}$ this problem is low Mach number. Solutions were obtained for different numbers of nodes (N_x) and grid speed (c). The mean velocity was calculated from the numerical results using the trapezium rule. For values of c below 1300 m/s the simulation was unstable. The results at larger values of c are shown in table 6.2.

As can be seen, increasing c has no effect on the results to four significant figures. The main cause of error is in the use of the trapezium rule, and the value of ϵ_{Kn} . To differentiate between these errors, trapezoidal integration of the analytical solution was carried out, giving the results shown in table 6.3.

Generally, standard LBM (where $\tilde{RT} = 1/3$) is stable at lower values of c , and so an increase in accuracy can be observed as c increases, consistent with reducing ϵ_{Ma} . In dimensional problems like this, where (\tilde{RT}) has a meaningful value, the requirement to have $\tilde{RT} \leq 1/3$ ensures that ϵ_{Ma} is already so small as to make further increases in accuracy insignificant.

Also recorded were the number of site updates, which is the number of iterations needed

c	N_x		
	30	60	90
1300	1.89×10^7	9.72×10^7	2.92×10^8
2000	1.80×10^7	1.37×10^8	4.29×10^8
3000	2.61×10^7	1.94×10^8	6.08×10^8
4000	3.33×10^7	2.45×10^8	8.26×10^8

Table 6.4: Number of site updates required to reach a converged solution

to reach convergence multiplied by the number of grid points. This is a good indication of the computational time required, regardless of implementation and hardware. It can be seen that increasing the value of c increases the computational time needed, without significantly increasing accuracy, and therefore the lowest value of c possible should be used.

The largest size of the grid spacing Δx was 3×10^{-7} m and grid spacing much larger than this was not stable. The size of the grid spacing is comparable to the mean free path of the gas, but only the continuum equations of fluid dynamics are modelled. Therefore, this method is not well suited for either microscopic or macroscopic modelling.

6.4 Conclusions

The moment based boundary condition method from Chapter 5 was applied to the Poiseuille flow, using the analytical solution for guidance on the values of the moments at the boundaries. At the wall the velocity tangential and normal to the wall was specified, and the viscous normal stress in the direction tangential to the wall was set to zero. At the open boundary the density was specified and the velocity tangential to the boundary and the viscous normal stress tangential to the boundary were set to zero. At the intersection between a wall and an open boundary all these conditions were imposed simultaneously. These boundary conditions are easy to implement and involve no significant increase in computational cost compared with others, such as the bounce-back boundary condition.

Non-dimensional results were obtained for the Poiseuille flow, which highlighted some

features of the LB model. Significantly, the model is not stable for values of $\tilde{RT} \gtrsim 1/3$ and the stability is highest when $\tilde{RT} = 1/3$. The accuracy improves as ϵ_{Ma} is reduced until the limit of the computer's numerical range is reached. Changes to the bulk viscosity, controlled by the relaxation time λ^ξ , cause instability outside of a relatively small region near $\lambda^\xi = \lambda^\nu$. This region is so narrow that the theoretical solution for a simple monatomic gas cannot be recovered.

Finally, the solution to a dimensional problem, Poiseuille flow of hydrogen, was obtained. The Ideal Gas equation of state was included in the model. To ensure that the value of \tilde{RT} is less than 1/3 the value of c must be large, thus the value of ϵ_{Ma} is small and the solution is sufficiently accurate for most purposes. Further increases in c increase the accuracy, but there are few applications where that level of accuracy would be required. Finally, the maximum physical grid spacing for which the scheme is stable is small, around 3×10^{-7} m.

Chapter 7

LB for Multi-Component Gases

The method developed in the previous chapters will now be extended to multi-component gas mixtures. As discussed in Section 3.1.6, most authors seek to split the collision step in the particle basis. Instead, the approach outlined here is to use the multiple relaxation time model to split the collision step in the moment basis, permitting a different relaxation frequency to be used for the diffusive effects and the viscous effects. The concept of a viscosity of each species within a mixture is occasionally mentioned in the literature, for example Asinari (2005). However, as it is poorly defined and not obviously useful it will not be considered in this work. Instead the viscosity is treated as a property of the mixture.

This chapter consists of a brief introduction to the nomenclature used, and an analytical solution for binary channel flow. Three lattice Boltzmann models are defined, analysed and compared, and the most suitable model is selected. Finally the solution of a dimensional binary channel flow problem is investigated. Unfortunately, this shows accuracy which is only first order.

7.1 Multi-component nomenclature

In a multi-component mixture each species is identified with a subscript σ , and the mixture pressure, density and velocity are defined as,

$$p = \sum_{\sigma} p_{\sigma} \quad \rho = \sum_{\sigma} \rho_{\sigma} \quad u = \frac{\sum_{\sigma} \rho_{\sigma} u_{\sigma}}{\rho} \quad (7.1)$$

The term mixture velocity will always refer to this, the mass averaged rather than mole averaged, velocity. The mole and mass fractions, X_{σ} and Y_{σ} respectively, are defined as

$$X_{\sigma} = \frac{p_{\sigma}}{p} \quad Y_{\sigma} = \frac{\rho_{\sigma}}{\rho} \quad (7.2)$$

The equation of state for each species is,

$$p_{\sigma} = \rho_{\sigma} \frac{R_0 T}{M_{\sigma}} = \rho_{\sigma} (R_{\sigma} T) \quad (7.3)$$

where R_0 is the universal molar gas constant. The equation of state for the mixture is

$$p = \rho \frac{R_0 T}{M} = \rho (RT) \quad (7.4)$$

Where M is the mole-averaged molar mass.

7.2 Binary channel flow theory

The flow of two gases through a channel with fixed partial pressures at both ends is the binary equivalent of Poiseuille flow and will now be analysed. The following simplifications will be employed,

$$\hat{u}_{\sigma,y} = 0 \quad \frac{\partial \hat{\rho}_{\sigma}}{\partial \hat{y}} = 0 \quad \frac{\partial \hat{p}_{\sigma}}{\partial \hat{y}} = 0 \quad \frac{\partial}{\partial \hat{t}} = 0 \quad (7.5)$$

Each species obeys the steady-state mass continuity equation,

$$\frac{\partial(\hat{\rho}_\sigma \hat{u}_{\sigma,x})}{\partial \hat{x}} = -\frac{\partial(\hat{\rho}_\sigma \hat{u}_{\sigma,y})}{\partial \hat{y}} = 0 \quad (7.6)$$

The general solution for channel flow of the mixture must be the same as that of a single-component fluid, namely the solution of,

$$\frac{\partial \hat{p}}{\partial \hat{x}} = \frac{\partial}{\partial \hat{y}} \left(\hat{\nu} \hat{\rho} \frac{\partial \hat{u}_x}{\partial \hat{y}} \right) \quad (7.7)$$

Where $\hat{\nu}$ is a suitable scaled viscosity of the mixture. Equation (7.7) may be integrated using a given slip velocity, \hat{u}_{slip} , at the wall. The value of the slip velocity is known from diffusion slip theory, and will be discussed in Section 7.6. $\hat{\rho}$ and $\hat{\nu}$ are uniform in the y direction, and can be taken outside the derivative. The result is,

$$\hat{u}_x = \hat{u}_{slip} + \frac{(\hat{y}^2 - (\hat{H}/2)^2)}{2\hat{\rho}\hat{\nu}} \frac{\partial \hat{p}}{\partial \hat{x}} \quad (7.8)$$

This equation shows that the mixture velocity is parabolic, shifted by the slip velocity at the wall.

Chapman and Cowling (1970) give the following general equation for diffusion of a binary mixture,

$$(u_{A,\alpha} - u_{B,\alpha}) = \frac{-1}{X_A X_B B_{A,B}} \left[\frac{\partial X_A}{\partial \hat{x}_\alpha} + \frac{n_A n_B (m_B - m_A)}{n \rho} \frac{\partial (\ln p)}{\partial \hat{x}_\alpha} - \frac{\rho_A \rho_B}{p \rho} (F_{A,\alpha} - F_{B,\alpha}) + k_T \frac{\partial (\ln T)}{\partial \hat{x}_\alpha} \right] \quad (7.9)$$

where $F_{\sigma,\alpha}$ is a force acting on the species σ in direction of α and k_T is the thermal diffusion ratio. The last two terms are not relevant to this work, but are included for completeness. m_σ is the mass of a molecule of species σ and $B_{\sigma,\varsigma}$ is the diffusion resistance between species σ and ς . The diffusion resistance is the inverse of the binary diffusion coefficient ($B_{\sigma,\varsigma} = 1/D_{\sigma,\varsigma}$). Clearly the diffusion is governed by four physical effects, the concentration

gradient of the species, the pressure gradient of the mixture, the body forces on the different species and the temperature gradient. The second term is known as ‘pressure diffusion’. A good example of where it is important is in the separation of a gas mixture rotated around an axis, such as in a centrifuge. The pressure gradient causes the species to separate until the concentration gradients cause diffusion in the opposite direction and a steady state is reached. In the applications considered in this work there are no body forces on the gases apart from gravity, and where species of different mass are considered this means that the third term is non-zero. However it will be small and may be safely ignored. The assumption is made that the thermal term of Equation (7.9) is zero, as the model is isothermal.

If ‘pressure diffusion’ is ignored the well known Stefan-Maxwell equation is recovered, which can be written as,

$$\hat{\rho} \frac{\partial Y_\sigma}{\partial \hat{x}_\alpha} = \hat{B}_{\sigma,s} \hat{\rho}_\sigma (\hat{u}_\alpha - \hat{u}_{\sigma,\alpha}) \quad (7.10)$$

Equation (7.10) shows that in channel flow, where the species density is constant across the channel, the species velocity takes a parabolic shape just like the mixture velocity but shifted by a constant value. Using Equation (7.8) for the mixture velocity in Equation (7.10) results in an expression for the species velocity,

$$\hat{u}_{\sigma,\alpha} = \hat{u}_{slip} + \frac{(\hat{y}^2 - (\hat{H}/2)^2)}{2\hat{\rho}\hat{\nu}} \frac{\partial \hat{p}}{\partial \hat{x}_\alpha} - \frac{\hat{\rho}}{\hat{B}_{\sigma,s}\hat{\rho}_\sigma} \frac{\partial Y_\sigma}{\partial \hat{x}_\alpha} \quad (7.11)$$

The species velocity is therefore determined by three factors; the slip velocity of the mixture at the wall, the mixture pressure gradient, and the species concentration gradient. Only the term involving the pressure gradient is a function of y . Figure 7.1 illustrates typical velocity profiles for binary channel flow.

Constant total pressure

If the total pressure is constant everywhere, Equation (7.11) reduces to,

$$\hat{u}_{\sigma,\alpha} = \hat{u}_{slip} - \frac{\hat{\rho}}{\hat{B}_{\sigma,s}\hat{\rho}_\sigma} \frac{\partial Y_\sigma}{\partial \hat{x}_\alpha} \quad (7.12)$$

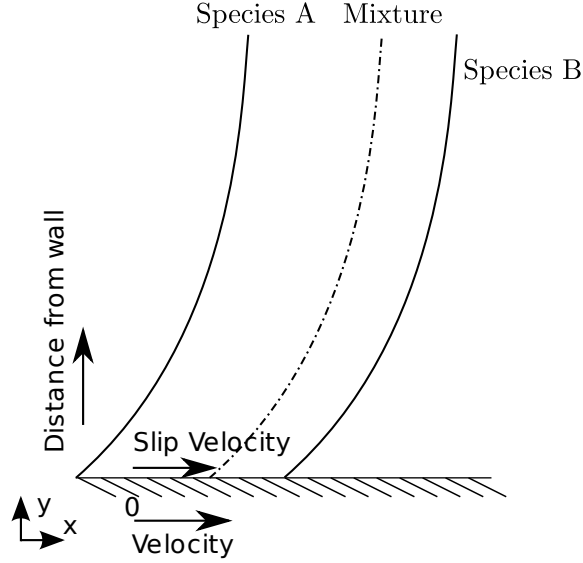


Figure 7.1: Typical velocity profiles for binary channel flow. The parabolic shape of the species and mixture velocities is due to the total pressure gradient. The slip velocity and the diffusion velocity are independent of y .

Using (7.12) and noting that if the total pressure is constant $\partial Y_A / \partial x_\alpha = -\partial Y_B / \partial x_\alpha$, the mixture velocity can be written as,

$$\hat{u}_\alpha = \hat{u}_{slip} - \frac{\hat{\rho}}{\hat{\rho} \hat{B}_{\sigma, \varsigma}} \left(\frac{\hat{\rho}_A}{\hat{\rho}_A} - \frac{\hat{\rho}_B}{\hat{\rho}_B} \right) \frac{\partial \hat{Y}_A}{\partial \hat{x}_\alpha} = \hat{u}_{slip} \quad (7.13)$$

The slip velocity is the only parameter that has an impact on the mixture velocity in the case of zero total pressure drop. If both gases have the same molar mass, diffusion slip theory predicts $\hat{u}_{slip} = 0$, and the mixture velocity \hat{u}_α is therefore zero. However, each individual species will have a velocity at the wall according to the third term of Equation (7.11).

7.3 Multi-component Lattice Boltzmann scheme

To define a Lattice Boltzmann scheme for multi-component gas mixtures, each species must have its own distribution function, f_σ . The lower moments of this function are the

species density and species velocity, in a similar way to the single-component equations. Thus,

$$\begin{bmatrix} \tilde{\Pi}_{\sigma,0} \\ \tilde{\Pi}_{\sigma,X} \\ \tilde{\Pi}_{\sigma,Y} \end{bmatrix} = \begin{bmatrix} \hat{\rho}_\sigma \\ \epsilon_{Ma}\hat{\rho}_\sigma\hat{u}_{\sigma,x} \\ \epsilon_{Ma}\hat{\rho}_\sigma\hat{u}_{\sigma,y} \end{bmatrix} \quad (7.14)$$

An equilibrium distribution function must also be defined. If the lower moments of the equilibrium function are the same as the moments above, momentum will be conserved by each species, and diffusion will not occur. If the lower moments of the equilibrium function are centred on the mixture velocity, then the momentum of the mixture will be conserved, but not that of each species. Therefore, the mixture velocity is used, and the lower moments of the equilibrium function are defined as,

$$\begin{bmatrix} \tilde{\Pi}_{\sigma,0}^{eq} \\ \tilde{\Pi}_{\sigma,X}^{eq} \\ \tilde{\Pi}_{\sigma,Y}^{eq} \end{bmatrix} = \begin{bmatrix} \hat{\rho}_\sigma \\ \epsilon_{Ma}\hat{\rho}_\sigma\hat{u}_x \\ \epsilon_{Ma}\hat{\rho}_\sigma\hat{u}_y \end{bmatrix} \quad (7.15)$$

It is not necessary that the equilibrium function takes this form, as long as the correct diffusion equation can be recovered. Although no alternative forms of the lower moments of the equilibrium function are considered in this work, that is not to say that such considerations might not be profitable. Similar to (4.16) for a single-component gas, the evolution equation for each species is,

$$\epsilon_{Ma}\epsilon_{Kn}\frac{\partial\tilde{f}_{\sigma,i}}{\partial\hat{t}} + \epsilon_{Kn}\tilde{e}_{x,i}\frac{\partial\tilde{f}_{\sigma,i}}{\partial\hat{x}} + \epsilon_{Kn}\tilde{e}_{y,i}\frac{\partial\tilde{f}_{\sigma,i}}{\partial\hat{y}} = \tilde{\Omega}(\tilde{f}_{\sigma,i}) \quad (7.16)$$

7.4 Mass conservation equation

The first moment of Equation (7.16) is,

$$\epsilon_{Kn}\epsilon_{Ma}\frac{\partial(\hat{\rho}_\sigma)}{\partial\hat{t}} + \epsilon_{Kn}\frac{\partial(\epsilon_{Ma}\hat{\rho}_\sigma\hat{u}_{\sigma,x})}{\partial\hat{x}} + \epsilon_{Kn}\frac{\partial(\epsilon_{Ma}\hat{\rho}_\sigma\hat{u}_{\sigma,y})}{\partial\hat{y}} = 0 \quad (7.17)$$

Thus, species mass conservation is ensured, and summing over the mixture it is trivial to show that the mixture mass is also conserved.

7.5 Momentum equation

In Chapter 4 an approximate expression for the momentum flux density tensor was obtained by assuming that the real distribution function was only slightly perturbed from the equilibrium function. This is not strictly true anymore, as the mixture velocity can be very different from the species velocity. In fact, this is an area which could certainly benefit from further work. Lacking such work however, it is assumed the method developed in Chapter 4 is still valid.

The right hand side of the momentum conservation equation is no longer zero, but instead is given by,

$$\tilde{\lambda}^\delta (\tilde{\Pi}_\alpha^{(eq)} - \tilde{\Pi}_\alpha) = \epsilon_{Ma}^2 \epsilon_{Kn} \hat{\lambda}^\delta \hat{\rho}_\sigma (\hat{u}_\alpha - \hat{u}_{\sigma,\alpha}) \quad (7.18)$$

where $\tilde{\lambda}^\delta = \tilde{\lambda}^1 = \tilde{\lambda}^2$ is introduced as the relaxation frequency controlling diffusion. The right hand side is obtained using the definitions of the lower moments from Section 7.3.

It is not possible to write the momentum equation for a single species in a mixture in the form of the corresponding conservation equation for a simple gas, see Vincenti and Kruger (1976). An approximation must be made but the direction to take is not clear. Hence, three plausible possibilities for the equilibrium distribution functions are considered. The first, and perhaps the most intuitive, is the Mixture Centred Equilibrium (MCE) where the higher moments are centred on the mixture velocity. The second is the Species Centred Equilibrium (SCE) where the higher moments are centred on the species velocity. The third is the Corrected Species Centred Equilibrium (CSCE) and will be explained later.

7.5.1 Mixture Centred Equilibrium (MCE)

If all the moments of the equilibrium function are centred on the mixture velocity, the higher moments are,

$$\begin{bmatrix} \tilde{\Pi}_{\sigma,XX}^{eq} \\ \tilde{\Pi}_{\sigma,YY}^{eq} \\ \tilde{\Pi}_{\sigma,XY}^{eq} \\ \tilde{\Pi}_{\sigma,XY}^{eq} \\ \tilde{\Pi}_{\sigma,XY}^{eq} \\ \tilde{\Pi}_{\sigma,XY}^{eq} \\ \tilde{\Pi}_{\sigma,XY}^{eq} \end{bmatrix} = \begin{bmatrix} \epsilon_{Ma}^2 (\hat{p}_\sigma + \hat{\rho}_\sigma (\hat{u}_x)^2) \\ \epsilon_{Ma}^2 (\hat{p}_\sigma + \hat{\rho}_\sigma (\hat{u}_y)^2) \\ \epsilon_{Ma}^2 \hat{\rho}_\sigma \hat{u}_x \hat{u}_y \\ \epsilon_{Ma} \hat{\rho}_\sigma \hat{u}_x / 3 \\ \epsilon_{Ma} \hat{\rho}_\sigma \hat{u}_y / 3 \\ \epsilon_{Ma} \hat{\rho}_\sigma \hat{u}_y / 3 \\ \epsilon_{Ma}^2 \frac{1}{3} (\hat{p}_\sigma + (\hat{\rho}_\sigma \hat{u}_x)^2 + (\hat{\rho}_\sigma \hat{u}_y)^2) \end{bmatrix} \quad (7.19)$$

An approximate expression for the momentum flux density tensor is then obtained following the approach of Section 4.3.2.

$$\begin{aligned} \epsilon_{Ma} \epsilon_{Kn} \frac{\partial}{\partial \hat{t}} \begin{pmatrix} \epsilon_{Ma}^2 (\hat{p}_\sigma + \hat{\rho}_\sigma \hat{u}_x^2) \\ \epsilon_{Ma}^2 (\hat{p}_\sigma + \hat{\rho}_\sigma \hat{u}_y^2) \\ \epsilon_{Ma}^2 (\hat{\rho}_\sigma \hat{u}_y \hat{u}_x) \end{pmatrix} + \epsilon_{Kn} \frac{\partial}{\partial \hat{x}} \begin{pmatrix} \epsilon_{Ma} \hat{\rho}_\sigma \hat{u}_x \\ \epsilon_{Ma} \frac{1}{3} \hat{\rho}_\sigma \hat{u}_x \\ \epsilon_{Ma} \frac{1}{3} \hat{\rho}_\sigma \hat{u}_y \end{pmatrix} + \epsilon_{Kn} \frac{\partial}{\partial \hat{y}} \begin{pmatrix} \epsilon_{Ma} \frac{1}{3} \hat{\rho}_\sigma \hat{u}_y \\ \epsilon_{Ma} \hat{\rho}_\sigma \hat{u}_y \\ \epsilon_{Ma} \frac{1}{3} \hat{\rho}_\sigma \hat{u}_x \end{pmatrix} \\ \approx \begin{pmatrix} \tilde{\lambda}^\nu (\tilde{\Pi}_{\sigma,XX}^{eq} - \tilde{\Pi}_{\sigma,XX}) \\ \tilde{\lambda}^\nu (\tilde{\Pi}_{\sigma,YY}^{eq} - \tilde{\Pi}_{\sigma,YY}) \\ \tilde{\lambda}^\nu (\tilde{\Pi}_{\sigma,XY}^{eq} - \tilde{\Pi}_{\sigma,XY}) \end{pmatrix} \end{aligned} \quad (7.20)$$

There are three different velocities that enter this expression; the velocity from the first order moment (like $\tilde{\Pi}_{\sigma,X}^{eq} = \tilde{\rho}_\sigma \tilde{u}_x$), the velocity from the third order moment (like $\tilde{\Pi}_{\sigma,XXX}^{eq} = \tilde{\Pi}_{\sigma,X}^{eq} = \tilde{\rho}_\sigma \tilde{u}_x$ and $\tilde{\Pi}_{\sigma,XY}^{eq} = \tilde{\rho}_\sigma \tilde{u}_x / 3$), and the velocity from the continuity equation. In this case these are the mixture, mixture and species velocities respectively. To reduce the algebraic complexity $\lambda^\nu = \lambda^\xi$ is assumed or, equivalently, that the collision matrix is diagonal. The result can be easily extended to the more general collision operator discussed earlier.

Repeating the analysis of Chapter 4, the time derivative terms are ignored except those

which (via the equation of state and the species mass conservation Equation (7.17)) contain $(\tilde{RT})_\sigma$. The following expressions for the components of the momentum flux density tensor are obtained,

$$\begin{pmatrix} \tilde{\Pi}_{\sigma,XX} \\ \tilde{\Pi}_{\sigma,YY} \\ \tilde{\Pi}_{\sigma,XY} \end{pmatrix} \approx \begin{pmatrix} \epsilon_{Ma}^2(\hat{p}_\sigma + \hat{\rho}_\sigma \hat{u}_x^2) \\ \epsilon_{Ma}^2(\hat{p}_\sigma + \hat{\rho}_\sigma \hat{u}_y^2) \\ 0 \end{pmatrix} + \epsilon_{Kn} \epsilon_{Ma} \frac{1}{\bar{\lambda}^\nu} \frac{\partial}{\partial \hat{x}} \begin{pmatrix} \hat{\rho}_\sigma(\hat{u}_x - (\tilde{RT})_\sigma \hat{u}_{\sigma,x}) \\ \hat{\rho}_\sigma(\frac{1}{3}\hat{u}_x - (\tilde{RT})_\sigma \hat{u}_{\sigma,x}) \\ \frac{1}{3}\hat{\rho}_\sigma \hat{u}_y \end{pmatrix} \\ + \epsilon_{Kn} \epsilon_{Ma} \frac{1}{\bar{\lambda}^\nu} \frac{\partial}{\partial \hat{y}} \begin{pmatrix} \hat{\rho}_\sigma(\frac{1}{3}\hat{u}_y - (\tilde{RT})_\sigma \hat{u}_{\sigma,y}) \\ \hat{\rho}_\sigma(\hat{u}_y - (\tilde{RT})_\sigma \hat{u}_{\sigma,y}) \\ \frac{1}{3}\hat{\rho}_\sigma \hat{u}_x \end{pmatrix} \quad (7.21)$$

The comparison between Equation (7.21) and Equation (4.44) is particularly interesting, due to the mix of species and mixture velocities in Equation (7.21). The necessary, but not sufficient, criteria for stability from Equation (4.44) was that $\tilde{RT} \lesssim 1/3$ (to ensure that the error terms in Equation (4.44) did not dominate). This condition is now replaced with the condition $(\tilde{RT})_\sigma \tilde{u}_{\sigma,\alpha} \lesssim \tilde{u}_\alpha/3$. Because this contains the species and mixture velocities a maximum stable value of $(\tilde{RT})_\sigma$ cannot be determined. However small values of $(\tilde{RT})_\sigma$ are more likely to be stable than large values.

The non-equilibrium parts of the moments are defined as $\Pi_{\alpha\beta}^{(neq)} = \Pi_{\alpha\beta} - \Pi_{\alpha\beta}^{(eq)}$, and will provide a useful shorthand in what follows. From Equation (7.21) it is clear that $\sum_\sigma \Pi_{\sigma,\alpha\beta}^{(neq)} = \Pi_{\alpha\beta}^{(neq)}$, where $\Pi_{\alpha\beta}^{(neq)}$ is the momentum flux density tensor for the mixture. Substituting the momentum flux density tensor into the species momentum equation, which is the multi-component version of Equation (4.46) gives,

$$\begin{aligned} \frac{\partial}{\partial \hat{t}} \begin{pmatrix} \hat{\rho}_\sigma \hat{u}_{\sigma,x} \\ \hat{\rho}_\sigma \hat{u}_{\sigma,y} \end{pmatrix} + \frac{\partial}{\partial \hat{x}} \begin{pmatrix} \hat{\rho}_\sigma \hat{u}_x^2 \\ \hat{\rho}_\sigma \hat{u}_x \hat{u}_y \end{pmatrix} + \frac{\partial}{\partial \hat{y}} \begin{pmatrix} \hat{\rho}_\sigma \hat{u}_x \hat{u}_y \\ \hat{\rho}_\sigma \hat{u}_y^2 \end{pmatrix} = - \begin{pmatrix} \frac{\partial}{\partial \hat{x}}(\hat{p}_\sigma) \\ \frac{\partial}{\partial \hat{y}}(\hat{p}_\sigma) \end{pmatrix} \\ + \frac{\partial}{\partial \hat{x}} \begin{pmatrix} \Pi_{\sigma,XX}^{(neq)} \\ \Pi_{\sigma,XY}^{(neq)} \end{pmatrix} + \frac{\partial}{\partial \hat{y}} \begin{pmatrix} \Pi_{\sigma,XY}^{(neq)} \\ \Pi_{\sigma,YY}^{(neq)} \end{pmatrix} + \begin{pmatrix} \hat{\lambda}^\delta \hat{\rho}_\sigma (\hat{u}_x - \hat{u}_{\sigma,x}) \\ \hat{\lambda}^\delta \hat{\rho}_\sigma (\hat{u}_y - \hat{u}_{\sigma,y}) \end{pmatrix} \quad (7.22) \end{aligned}$$

Note the factor of $\epsilon_{Ma}^2 \epsilon_{Kn}$ from Equation (7.18) cancels with terms in the momentum equation. Summing over the species results in the momentum equation for the mixture,

$$\begin{aligned} \frac{\partial}{\partial \hat{t}} \begin{pmatrix} \hat{\rho} \hat{u}_x \\ \hat{\rho} \hat{u}_y \end{pmatrix} + \frac{\partial}{\partial \hat{x}} \begin{pmatrix} \hat{\rho} \hat{u}_x^2 \\ \hat{\rho} \hat{u}_x \hat{u}_y \end{pmatrix} + \frac{\partial}{\partial \hat{y}} \begin{pmatrix} \hat{\rho} \hat{u}_x \hat{u}_y \\ \hat{\rho} \hat{u}_y^2 \end{pmatrix} = - \begin{pmatrix} \frac{\partial}{\partial \hat{x}}(\hat{p}) \\ \frac{\partial}{\partial \hat{y}}(\hat{p}) \end{pmatrix} \\ + \frac{\partial}{\partial \hat{x}} \begin{pmatrix} \Pi_{XX}^{(neq)} \\ \Pi_{XY}^{(neq)} \end{pmatrix} + \frac{\partial}{\partial \hat{y}} \begin{pmatrix} \Pi_{\sigma,XY}^{(neq)} \\ \Pi_{\sigma,YY}^{(neq)} \end{pmatrix} \end{aligned} \quad (7.23)$$

This is the same equation as for a single-component fluid, Equation (4.52), and the momentum flux density tensor is the same as Equations (4.44) and (4.45) but with the mixture velocity and density. Multiplying Equation (7.23) by the mass fraction, Y_σ , and subtracting Equation (7.22) results in,

$$Y_\sigma \frac{\partial}{\partial \hat{x}_\alpha}(\hat{p}) - \frac{\partial}{\partial \hat{\alpha}}(\hat{p}_\sigma) = (Y_\sigma - X_\sigma) \frac{\partial}{\partial \hat{x}_\alpha}(\hat{p}) - \hat{p} \frac{\partial}{\partial \hat{x}_\alpha}(X_\sigma) = -\hat{\lambda}^\delta \hat{\rho}_\sigma (\hat{u}_\alpha - \hat{u}_{\sigma,\alpha}) \quad (7.24)$$

An expression linking the diffusion resistance to the relaxation frequency is now needed. The expression given by Chapman and Cowling (1970) for the continuum BGK equation is,

$$\hat{\lambda}^\delta = \frac{\hat{\rho} \hat{k} T}{\hat{n} \hat{m}_\sigma \hat{m}_\varsigma} \hat{B}_{\sigma\varsigma} = (X_\sigma (\hat{R}T)_\varsigma + X_\varsigma (\hat{R}T)_\sigma) \hat{B}_{\sigma\varsigma} \quad (7.25)$$

where k is the Boltzmann constant. Fortunately, this expression can be used without modification in the D2Q9 Lattice Boltzmann scheme. Substituting Equation (7.25) into Equation (7.24) results in,

$$(Y_\sigma - X_\sigma) \frac{\partial}{\partial \hat{x}_\alpha}(\hat{p}) - \hat{p} \frac{\partial}{\partial \hat{x}_\alpha}(X_\sigma) = \frac{\hat{k} T \hat{n}_\sigma \hat{n}_\varsigma \hat{B}_{\sigma\varsigma}}{\hat{n}} (\hat{u}_{\sigma,\alpha} - \hat{u}_{\varsigma,\alpha}) \quad (7.26)$$

Comparison between Equation (7.9) and a manipulated form of Equation (7.26) shows that the correct form for ordinary diffusion and pressure diffusion are exactly recovered.

The relaxation frequency related to viscosity is defined as it was in the single-component

case, Equation (4.50),

$$\tilde{\lambda}_\sigma^\nu = \frac{1}{3\tilde{\nu}} \quad (7.27)$$

7.5.2 Species Centred Equilibrium (SCE)

The second alternative equilibrium function is the Species Centred Equilibrium function, for which the higher moments are defined as,

$$\begin{bmatrix} \tilde{\Pi}_{\sigma,XX}^{eq} \\ \tilde{\Pi}_{\sigma,YY}^{eq} \\ \tilde{\Pi}_{\sigma,XY}^{eq} \\ \tilde{\Pi}_{\sigma,XYX}^{eq} \\ \tilde{\Pi}_{\sigma,XYX}^{eq} \\ \tilde{\Pi}_{\sigma,XXYY}^{eq} \end{bmatrix} = \begin{bmatrix} \epsilon_{Ma}^2 (\hat{p}_\sigma + \hat{\rho}_\sigma (\hat{u}_{\sigma,x})^2) \\ \epsilon_{Ma}^2 (\hat{p}_\sigma + \hat{\rho}_\sigma (\hat{u}_{\sigma,y})^2) \\ \epsilon_{Ma}^2 \hat{\rho}_\sigma \hat{u}_{\sigma,x} \hat{u}_{\sigma,y} \\ \epsilon_{Ma} \hat{\rho}_\sigma \hat{u}_{\sigma,x} / 3 \\ \epsilon_{Ma} \hat{\rho}_\sigma \hat{u}_{\sigma,y} / 3 \\ \epsilon_{Ma}^2 \frac{1}{3} (\hat{p}_\sigma + (\hat{\rho} \hat{u}_{\sigma,x})^2 + (\hat{\rho} \hat{u}_{\sigma,y})^2) \end{bmatrix} \quad (7.28)$$

Using this equilibrium function the equivalent to Equation (7.20) is,

$$\begin{aligned} \epsilon_{Ma} \epsilon_{Kn} \frac{\partial}{\partial \hat{t}} \begin{pmatrix} \epsilon_{Ma}^2 (\hat{p}_\sigma + \hat{\rho}_\sigma \hat{u}_{\sigma,x}^2) \\ \epsilon_{Ma}^2 (\hat{p}_\sigma + \hat{\rho}_\sigma \hat{u}_{\sigma,y}^2) \\ \epsilon_{Ma}^2 (\hat{\rho} \hat{u}_y \hat{u}_x) \end{pmatrix} + \epsilon_{Kn} \frac{\partial}{\partial \hat{x}} \begin{pmatrix} \epsilon_{Ma} \hat{\rho}_\sigma \hat{u}_x \\ \epsilon_{Ma} \frac{1}{3} \hat{\rho}_\sigma \hat{u}_{\sigma,x} \\ \epsilon_{Ma} \frac{1}{3} \hat{\rho}_\sigma \hat{u}_{\sigma,y} \end{pmatrix} + \epsilon_{Kn} \frac{\partial}{\partial \hat{y}} \begin{pmatrix} \epsilon_{Ma} \frac{1}{3} \hat{\rho}_\sigma \hat{u}_{\sigma,y} \\ \epsilon_{Ma} \hat{\rho}_\sigma \hat{u}_y \\ \epsilon_{Ma} \frac{1}{3} \hat{\rho}_\sigma \hat{u}_{\sigma,x} \end{pmatrix} \\ \approx \begin{pmatrix} \tilde{\lambda}^\nu (\epsilon_{Ma}^2 (\hat{p}_\sigma + \hat{\rho}_\sigma (\hat{u}_{\sigma,x})^2) - \tilde{\Pi}_{\sigma,XX}) \\ \tilde{\lambda}^\nu (\epsilon_{Ma}^2 (\hat{p}_\sigma + \hat{\rho}_\sigma (\hat{u}_{\sigma,y})^2) - \tilde{\Pi}_{\sigma,YY}) \\ \tilde{\lambda}^\nu (\epsilon_{Ma}^2 \hat{\rho}_\sigma \hat{u}_{\sigma,x} \hat{u}_{\sigma,y} - \tilde{\Pi}_{\sigma,XY}) \end{pmatrix} \end{aligned} \quad (7.29)$$

which can be rearranged as,

$$\begin{aligned}
\begin{pmatrix} \tilde{\Pi}_{\sigma,XX} \\ \tilde{\Pi}_{\sigma,YY} \\ \tilde{\Pi}_{\sigma,XY} \end{pmatrix} &\approx \begin{pmatrix} \epsilon_{Ma}^2(\hat{p}_\sigma + \hat{\rho}_\sigma \hat{u}_{\sigma,x}^2) \\ \epsilon_{Ma}^2(\hat{p}_\sigma + \hat{\rho}_\sigma \hat{u}_{\sigma,y}^2) \\ 0 \end{pmatrix} + \epsilon_{Kn} \epsilon_{Ma} \frac{1}{\tilde{\lambda}^\nu} \frac{\partial}{\partial \hat{x}} \begin{pmatrix} \hat{\rho}_\sigma(\hat{u}_x - (\tilde{RT})_\sigma \hat{u}_{\sigma,x}) \\ \hat{\rho}_\sigma(\frac{1}{3} - (\tilde{RT})_\sigma) \hat{u}_{\sigma,x} \\ \frac{1}{3} \hat{\rho}_\sigma \hat{u}_{\sigma,y} \end{pmatrix} \\
&+ \epsilon_{Kn} \epsilon_{Ma} \frac{1}{\tilde{\lambda}^\nu} \frac{\partial}{\partial \hat{y}} \begin{pmatrix} \hat{\rho}_\sigma(\frac{1}{3} - (\tilde{RT})_\sigma) \hat{u}_{\sigma,y} \\ \hat{\rho}_\sigma(\hat{u}_y - (\tilde{RT})_\sigma \hat{u}_{\sigma,y}) \\ \frac{1}{3} \hat{\rho}_\sigma \hat{u}_{\sigma,x} \end{pmatrix} \quad (7.30)
\end{aligned}$$

The momentum flux density tensor still contains both mixture and species velocities, and both the stability criteria $\tilde{RT}_\sigma \lesssim 1/3$ and $(\tilde{RT})_\sigma \tilde{u}_{\sigma,\alpha} \lesssim \tilde{u}_\alpha/3$ now apply. It is not clear if this is an advantage over the MCE or not. The species momentum equation is,

$$\begin{aligned}
\frac{\partial}{\partial \hat{t}} \begin{pmatrix} \hat{\rho}_\sigma \hat{u}_{\sigma,x} \\ \hat{\rho}_\sigma \hat{u}_{\sigma,y} \end{pmatrix} + \frac{\partial}{\partial \hat{x}} \begin{pmatrix} \hat{\rho}_\sigma \hat{u}_{\sigma,x}^2 \\ \hat{\rho}_\sigma \hat{u}_{\sigma,x} \hat{u}_{\sigma,y} \end{pmatrix} + \frac{\partial}{\partial \hat{y}} \begin{pmatrix} \hat{\rho}_\sigma \hat{u}_{\sigma,x} \hat{u}_{\sigma,y} \\ \hat{\rho}_\sigma \hat{u}_{\sigma,y}^2 \end{pmatrix} &= - \begin{pmatrix} \frac{\partial}{\partial \hat{x}}(\hat{p}_\sigma) \\ \frac{\partial}{\partial \hat{y}}(\hat{p}_\sigma) \end{pmatrix} \\
+ \frac{\partial}{\partial \hat{x}} \begin{pmatrix} \Pi_{\sigma,XX}^{(neq)} \\ \Pi_{\sigma,XY}^{(neq)} \end{pmatrix} + \frac{\partial}{\partial \hat{y}} \begin{pmatrix} \Pi_{\sigma,XY}^{(neq)} \\ \Pi_{\sigma,YY}^{(neq)} \end{pmatrix} + \begin{pmatrix} \hat{\lambda}^\delta \hat{\rho}_\sigma(\hat{u}_x - \hat{u}_{\sigma,x}) \\ \hat{\lambda}^\delta \hat{\rho}_\sigma(\hat{u}_y - \hat{u}_{\sigma,y}) \end{pmatrix} \quad (7.31)
\end{aligned}$$

and the momentum equation for the mixture is,

$$\begin{aligned}
\frac{\partial}{\partial \hat{t}} \begin{pmatrix} \hat{\rho} \hat{u}_x \\ \hat{\rho} \hat{u}_y \end{pmatrix} + \frac{\partial}{\partial \hat{x}} \begin{pmatrix} \sum_\sigma \hat{\rho}_\sigma \hat{u}_{\sigma,x}^2 \\ \sum_\sigma \hat{\rho}_\sigma \hat{u}_{\sigma,x} \hat{u}_{\sigma,y} \end{pmatrix} + \frac{\partial}{\partial \hat{y}} \begin{pmatrix} \sum_\sigma \hat{\rho}_\sigma \hat{u}_{\sigma,x} \hat{u}_{\sigma,y} \\ \sum_\sigma \hat{\rho}_\sigma \hat{u}_{\sigma,y}^2 \end{pmatrix} &= \\
- \begin{pmatrix} \frac{\partial}{\partial \hat{x}}(\hat{p}) \\ \frac{\partial}{\partial \hat{y}}(\hat{p}) \end{pmatrix} + \frac{\partial}{\partial \hat{x}} \begin{pmatrix} \Pi_{XX}^{(neq)} \\ \Pi_{XY}^{(neq)} \end{pmatrix} + \frac{\partial}{\partial \hat{y}} \begin{pmatrix} \Pi_{XY}^{(neq)} \\ \Pi_{YY}^{(neq)} \end{pmatrix} \quad (7.32)
\end{aligned}$$

The advection terms in this equation are not correct. This is a serious problem and the Corrected Species Centred Equilibrium (CSCE) is introduced to address this difficulty.

7.5.3 Corrected Species Centred Equilibrium (CSCE)

The Corrected Species Centred Equilibrium function consists of the SCE with a correction to the equilibrium momentum flux density tensor such that the equilibrium function becomes,

$$\begin{bmatrix} \tilde{\Pi}_{\sigma,XX}^{eq} \\ \tilde{\Pi}_{\sigma,YY}^{eq} \\ \tilde{\Pi}_{\sigma,XY}^{eq} \\ \tilde{\Pi}_{\sigma,XY}^{eq} \\ \tilde{\Pi}_{\sigma,XY}^{eq} \\ \tilde{\Pi}_{\sigma,XY}^{eq} \end{bmatrix} = \begin{bmatrix} \epsilon_{Ma}^2 (\hat{p}_\sigma + \hat{\rho}_\sigma \hat{u}_{\sigma,x} \hat{u}_x) \\ \epsilon_{Ma}^2 (\hat{p}_\sigma + \hat{\rho}_\sigma \hat{u}_{\sigma,y} \hat{u}_y) \\ \epsilon_{Ma}^2 \hat{\rho}_\sigma \frac{1}{2} (\hat{u}_{\sigma,x} \hat{u}_y + \hat{u}_{\sigma,y} \hat{u}_x) \\ \epsilon_{Ma} \hat{\rho}_\sigma \hat{u}_{\sigma,x} / 3 \\ \epsilon_{Ma} \hat{\rho}_\sigma \hat{u}_{\sigma,y} / 3 \\ \epsilon_{Ma}^2 \frac{1}{3} (\hat{p}_\sigma + (\hat{\rho} \hat{u}_{\sigma,x})^2 + (\hat{\rho} \hat{u}_{\sigma,y})^2) \end{bmatrix} \quad (7.33)$$

The non-equilibrium momentum flux density tensor (the viscous stress tensor) is the same as that recovered from the SCE, specifically

$$\begin{pmatrix} \tilde{\Pi}^{(neq)}_{\sigma,XX} \\ \tilde{\Pi}^{(neq)}_{\sigma,YY} \\ \tilde{\Pi}^{(neq)}_{\sigma,XY} \end{pmatrix} \approx \epsilon_{Kn} \epsilon_{Ma} \frac{1}{\tilde{\lambda}^\nu} \frac{\partial}{\partial \hat{x}} \begin{pmatrix} \hat{\rho}_\sigma (\hat{u}_x - (\tilde{RT})_\sigma \hat{u}_{\sigma,x}) \\ \hat{\rho}_\sigma (\frac{1}{3} - (\tilde{RT})_\sigma) \hat{u}_{\sigma,x} \\ \frac{1}{3} \hat{\rho}_\sigma \hat{u}_{\sigma,y} \end{pmatrix} + \epsilon_{Kn} \epsilon_{Ma} \frac{1}{\tilde{\lambda}^\nu} \frac{\partial}{\partial \hat{y}} \begin{pmatrix} \hat{\rho}_\sigma (\frac{1}{3} - (\tilde{RT})_\sigma) \hat{u}_{\sigma,y} \\ \hat{\rho}_\sigma (\hat{u}_y - (\tilde{RT})_\sigma \hat{u}_{\sigma,y}) \\ \frac{1}{3} \hat{\rho}_\sigma \hat{u}_{\sigma,x} \end{pmatrix} \quad (7.34)$$

This has the same stability criteria as the SCE. The species momentum equation is,

$$\begin{aligned} \frac{\partial}{\partial \hat{t}} \begin{pmatrix} \hat{\rho}_\sigma \hat{u}_{\sigma,x} \\ \hat{\rho}_\sigma \hat{u}_{\sigma,y} \end{pmatrix} + \frac{\partial}{\partial \hat{x}} \begin{pmatrix} \hat{\rho}_\sigma \hat{u}_{\sigma,x} \hat{u}_x \\ \hat{\rho}_\sigma \frac{1}{2} (\hat{u}_{\sigma,x} \hat{u}_y + \hat{u}_{\sigma,y} \hat{u}_x) \end{pmatrix} + \frac{\partial}{\partial \hat{y}} \begin{pmatrix} \hat{\rho}_\sigma \frac{1}{2} (\hat{u}_{\sigma,x} \hat{u}_y + \hat{u}_{\sigma,y} \hat{u}_x) \\ \hat{\rho}_\sigma \hat{u}_{\sigma,y} \hat{u}_y \end{pmatrix} = \\ - \begin{pmatrix} \frac{\partial}{\partial \hat{x}} (\hat{p}_\sigma) \\ \frac{\partial}{\partial \hat{y}} (\hat{p}_\sigma) \end{pmatrix} + \frac{\partial}{\partial \hat{x}} \begin{pmatrix} \Pi_{\sigma,XX}^{(neq)} \\ \Pi_{\sigma,XY}^{(neq)} \end{pmatrix} + \frac{\partial}{\partial \hat{y}} \begin{pmatrix} \Pi_{\sigma,XY}^{(neq)} \\ \Pi_{\sigma,YY}^{(neq)} \end{pmatrix} + \begin{pmatrix} \hat{\lambda}^\delta \hat{\rho}_\sigma (\hat{u}_x - \hat{u}_{\sigma,x}) \\ \hat{\lambda}^\delta \hat{\rho}_\sigma (\hat{u}_y - \hat{u}_{\sigma,y}) \end{pmatrix} \end{aligned} \quad (7.35)$$

The strange advection terms in the species momentum equation are the price paid for the correct advection terms in the mixture momentum equation. Summing over the species

gives the momentum equation for the mixture,

$$\begin{aligned} \frac{\partial}{\partial \hat{t}} \begin{pmatrix} \hat{\rho} \hat{u}_x \\ \hat{\rho} \hat{u}_y \end{pmatrix} + \frac{\partial}{\partial \hat{x}} \begin{pmatrix} \hat{\rho} \hat{u}_x^2 \\ \hat{\rho} \hat{u}_x \hat{u}_y \end{pmatrix} + \frac{\partial}{\partial \hat{y}} \begin{pmatrix} \hat{\rho} \hat{u}_x \hat{u}_y \\ \hat{\rho} \hat{u}_y^2 \end{pmatrix} = \\ - \begin{pmatrix} \frac{\partial}{\partial \hat{x}}(\hat{p}) \\ \frac{\partial}{\partial \hat{y}}(\hat{p}) \end{pmatrix} + \frac{\partial}{\partial \hat{x}} \begin{pmatrix} \Pi_{XX}^{(neq)} \\ \Pi_{XY}^{(neq)} \end{pmatrix} + \frac{\partial}{\partial \hat{y}} \begin{pmatrix} \Pi_{XY}^{(neq)} \\ \Pi_{YY}^{(neq)} \end{pmatrix} \end{aligned} \quad (7.36)$$

Multiplying Equation (7.36) by the mass fraction, Y_σ , and subtracting Equation (7.35) results in terms of the form $\rho_\sigma u(u - u_\sigma)$. Thus, the Stefan-Maxwell equation is not recovered at all times. However this is also true for continuum kinetic theory, where the Stefan-Maxwell equation is only recovered when all velocity gradients giving rise to viscous stresses are zero.

7.6 Expressions for diffusion slip

In Section 3.2.1, the Kramers and Kistemaker (1943) expression for diffusion slip was derived from simple kinetic theory.

$$\sum_{\sigma} \frac{\rho_{\sigma} u_{\sigma,x}}{\sqrt{M_{\sigma}}} = 0 \quad (7.37)$$

This expression is valid along a wall where the x direction is parallel to the wall. If the denominator of this expression is instead unity, a zero mixture velocity at the wall is obtained. It is important to note that this is not the same as the zero species velocity condition usually used in LB. In order to cover both possibilities a function of molecular weight, $S(M_\sigma)$, is introduced, where either $S(M_\sigma) = 1$ or $S(M_\sigma) = \sqrt{M_\sigma}$. Thus,

$$\sum_{\sigma} \frac{\rho_{\sigma} u_{\sigma,x}}{S(M_{\sigma})} = 0 \quad (7.38)$$

This expression relates one species velocity to the other, but the absolute value of either species velocity cannot be determined. A further condition is therefore required. As shown

in Equation (7.11) the species velocity is influenced by three terms. Across a channel the term containing the slip velocity and the diffusion term are both constant and only the viscous term varies. Therefore,

$$\frac{\partial u_x}{\partial y} = \frac{\partial u_{\sigma,x}}{\partial y} \quad (7.39)$$

Equation (7.38) and (7.39) prove to be sufficient conditions for the species velocities tangential to the wall to be determined. The velocity of each species normal to the wall is zero, $u_{\sigma,y} = 0$.

Kramers and Kistemaker derived an expression based on these equations, and the equipartition of energy, for a binary gas with $M_B > M_A$.

$$u_{x,slip} = \frac{\sqrt{M_B} - \sqrt{M_A}}{p_A\sqrt{M_A} + p_B\sqrt{M_B}} D_{AB} \frac{\partial p_A}{\partial x} \quad (7.40)$$

Clearly, the slip velocity will take the same sign as the gradient of the lighter gas concentration.

7.6.1 Implementing diffusion slip in the LB method

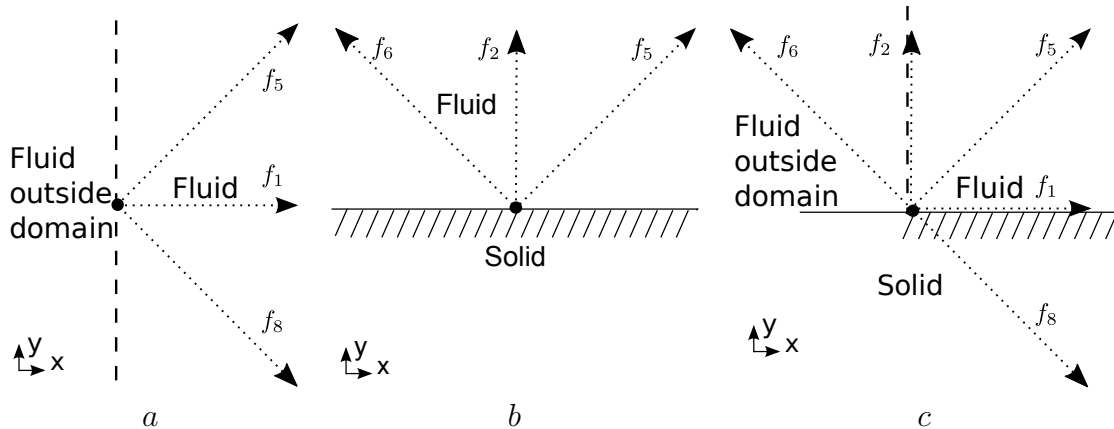


Figure 7.2: Summary of the geometry of boundary nodes repeated from Chapter 5. *a* is an open boundary, *b* is a wall, and *c* is a corner node.

In this section a diffusion slip condition will be implemented on a flat wall, with unknown f values f_2 , f_5 and f_6 as shown in Figure 7.2*b*. Equation (7.39) must be transformed into

a condition for the XY component of the momentum flux density tensor of each species. The viscous shear stress, in multicomponent channel flow, based on the SCE or CSCE models (see Equation (7.30)) is,

$$\tilde{\Pi}_{\sigma,XY} \approx -\epsilon_{Ma}^2 \hat{\nu} \hat{\rho}_\sigma \frac{\partial \hat{u}_{\sigma,x}}{\partial \hat{y}} \quad (7.41)$$

If the MCE (Equation (7.21)) is used the viscous shear stress is,

$$\tilde{\Pi}_{\sigma,XY} \approx -\epsilon_{Ma}^2 \hat{\nu} \hat{\rho}_\sigma \frac{\partial \hat{u}_x}{\partial \hat{y}} \quad (7.42)$$

In fact the analysis is the same whichever equilibrium function is used. Equation (7.39) becomes,

$$\frac{1}{\rho_A} (\Pi_{A,XY}) = \frac{1}{\rho_B} (\Pi_{B,XY}) \quad (7.43)$$

$$\frac{1}{\rho_A} (f_{5,A} - f_{6,A} + f_{7,A} - f_{8,A}) = \frac{1}{\rho_B} (f_{5,B} - f_{6,B} + f_{7,B} - f_{8,B}) \quad (7.44)$$

The species mass flux in the x direction is given by the equation,

$$f_{\sigma,5} - f_{\sigma,6} = \rho_\sigma u_{\sigma,x} - f_{\sigma,1} - f_{\sigma,8} + f_{\sigma,3} + f_{\sigma,7} \quad (7.45)$$

To eliminate the unknown f values in Equation (7.44), substitute in Equation (7.45) to give,

$$\frac{1}{\rho_A} (\rho_A u_{A,x} - f_{1,A} - 2f_{8,A} + f_{3,A} + 2f_{7,A}) = \frac{1}{\rho_B} (\rho_B u_{B,x} - f_{1,B} - 2f_{8,B} + f_{3,B} + 2f_{7,B}) \quad (7.46)$$

For convenience a new variable composed only of known f values is introduced, $\kappa_\sigma = -f_{1,\sigma} - 2f_{8,\sigma} + f_{3,\sigma} + 2f_{7,\sigma}$. The density at the wall is already known, and is given by,

$$\rho_\sigma = f_{\sigma,0} + f_{\sigma,1} + f_{\sigma,3} + 2(f_{\sigma,2} + f_{\sigma,6} + f_{\sigma,5}) \quad (7.47)$$

Substituting in the other boundary condition necessary for diffusion slip, Equation (7.38), gives,

$$\frac{1}{\rho_A}(\rho_A u_{A,x} + \kappa_A) = \frac{1}{\rho_B} \left(-\frac{S(M_B)}{S(M_A)}(\rho_A u_{A,x}) + \kappa_B \right) \quad (7.48)$$

which can be rearranged as

$$(\rho_A u_{A,x}) \left(\frac{1}{\rho_A} + \frac{S(M_B)}{\rho_B S(M_A)} \right) = \frac{1}{\rho_B}(\kappa_B) - \frac{1}{\rho_A}(\kappa_A) \quad (7.49)$$

This is an expression for the velocity to be set at the wall, and it can be used to set the unknown f values. There is a similar expression for species B, obtained by swapping the B and A subscripts.

The procedure described in Chapter 6 is then used for setting this velocity at the wall, with the other conditions being $\tilde{u}_{\sigma,y} = 0$ and $\tilde{\Pi}_{\sigma,XX} = \tilde{p}_\sigma + \tilde{\rho}_\sigma \tilde{u}_x^2$ (MCE), $\tilde{\Pi}_{\sigma,XX} = \tilde{p}_\sigma + \tilde{\rho}_\sigma \tilde{u}_{\sigma,x}^2$ (SCE) or $\tilde{\Pi}_{\sigma,XX} = \tilde{p}_\sigma + \tilde{\rho}_\sigma \tilde{u}_{\sigma,x} \tilde{u}_x$ (CSCE).

7.6.2 Intersections between walls and open boundaries

In a corner between an open boundary and a wall there are 5 unknowns, $f_{\sigma,1}$, $f_{\sigma,2}$, $f_{\sigma,5}$, $f_{\sigma,6}$ and $f_{\sigma,8}$, as shown in Figure 7.2c. The density is the same as at the open boundary and the velocity and viscous shear stress are determined by the conditions for a solid wall. The definitions of the moments, $\Pi_{\sigma,0}$, $\Pi_{\sigma,X}$, $\Pi_{\sigma,Y} = 0$ and $\Pi_{\sigma,YX} = \rho_\sigma(RT)_\sigma$ can be written with the unknown f_σ values on the left hand side,

$$f_{\sigma,1} + f_{\sigma,2} + f_{\sigma,5} + f_{\sigma,6} + f_{\sigma,8} = \rho - f_{\sigma,3} - f_{\sigma,4} - f_{\sigma,7} - f_{\sigma,0} \quad (7.50)$$

$$f_{\sigma,1} + f_{\sigma,5} + f_{\sigma,8} - f_{\sigma,6} = \rho_\sigma u_{\sigma,x} + f_{\sigma,3} + f_{\sigma,7} \quad (7.51)$$

$$f_{\sigma,2} + f_{\sigma,6} + f_{\sigma,5} - f_{\sigma,8} = f_{\sigma,7} + f_{\sigma,4} \quad (7.52)$$

$$f_{\sigma,5} + f_{\sigma,6} + f_{\sigma,2} + f_{\sigma,8} = \rho_\sigma(RT)_\sigma - f_{\sigma,7} - f_{\sigma,4} \quad (7.53)$$

Combining these expressions allows the elimination of the unknowns in the XY component of the species momentum flux density tensor, resulting in,

$$\Pi_{\sigma,XY} = (4f_{7,\sigma} + f_{0,\sigma} + 2f_{3,\sigma} + 2f_{4,\sigma} - \rho_{\sigma} + \rho_{\sigma}u_{x,\sigma}) \quad (7.54)$$

For the sake of convenience, a new variable is introduced, $\Theta_{\sigma} = 4f_{7,\sigma} + f_{0,\sigma} + 2f_{3,\sigma} + 2f_{4,\sigma}$, which is composed only of the known f values. Substituting Equation (7.54) into Equation (7.43) yields,

$$(\Theta_A - \rho_A + \rho_A u_{x,A}) \frac{1}{\rho_A} = (\Theta_B - \rho_B + \rho_B u_{x,B}) \frac{1}{\rho_B} \quad (7.55)$$

Finally using Equation (7.38),

$$(\Theta_A - \rho_A + \rho_A u_{x,A}) \frac{1}{\rho_A} = \left(\Theta_B - \rho_B - \rho_A u_{x,A} \frac{S(M_B)}{S(M_A)} \right) \frac{1}{\rho_B} \quad (7.56)$$

$$u_{x,A} \left(1 + \frac{\rho_A S(M_B)}{\rho_B S(M_A)} \right) = \frac{1}{\rho_B} (\Theta_B - \rho_B) - \frac{1}{\rho_A} (\Theta_A - \rho_A) \quad (7.57)$$

This x velocity is to be set at the corner and can be imposed using the equations described in Section 6.1.1.

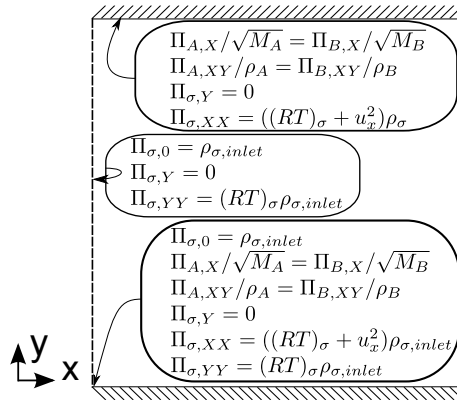


Figure 7.3: The boundary conditions at the wall, the open boundary and the intersection between the two for binary channel flow.

Figure 7.3 shows a summary of all the boundary conditions in the moment basis for the

binary channel flow problem.

7.7 Modified relaxation times

Following the approach of Section 5.2, a modified diffusion resistance is defined to take account of second order numerical effects. Taking the x direction as an example the equation that will be implemented is,

$$\tilde{\Pi}_X^+ - \tilde{\Pi}_X = \tilde{\lambda}^{\delta'} (\tilde{\Pi}_X^{(eq)} - \tilde{\Pi}_X) \quad (7.58)$$

Compare Equation (7.58) above with a similar one derived using central differencing,

$$(\tilde{\Pi}_X^+ - \tilde{\Pi}_X) = \frac{\tilde{\lambda}^\delta}{2} \left((\tilde{\Pi}_X^{(eq)} - \tilde{\Pi}_X) + (\tilde{\Pi}_X^{(eq)+} - \tilde{\Pi}_X^+) \right) \quad (7.59)$$

Again assume $\Pi_X^{(eq)+} = \Pi_X^{(eq)}$, leading to,

$$(\tilde{\Pi}_X^+ - \tilde{\Pi}_X) \left(1 + \frac{\tilde{\lambda}^\delta}{2} \right) = \tilde{\lambda}^\delta (\tilde{\Pi}_X^{(eq)} - \tilde{\Pi}_X) \quad (7.60)$$

For Equation (7.60) to be identical to Equation (7.58), the modified relaxation frequency must be,

$$\tilde{\lambda}^{\delta'} = \frac{\tilde{\lambda}^\delta}{\left(1 + \frac{\tilde{\lambda}^\delta}{2} \right)} \quad (7.61)$$

In all the simulations performed the higher relaxation times were $\lambda^{\delta'} = \lambda^{\gamma'} = \lambda^{\delta'}$ and $\lambda^{8'} = \lambda^{\nu'}$.

7.8 Self-diffusion test case

The simplest test for a multicomponent model is channel flow of a binary gas with both components having the same molar mass. This is called self-diffusion. The two species can be thought of as two colours or isotopes of the same gas, with a high concentration

of one colour at one end. Obviously, the mixture should behave in the same way as for a single-component gas with the same molar mass. However, if one considers the values of ϵ_{ma} for each species, they may well be higher than the mixture value, and so the error may be higher than for an equivalent single-component gas.

The wall boundary condition predicted by diffusion slip theory is zero mixture velocity. However, each species is allowed to slip at the wall.

Simulations were performed with zero total pressure drop at different values of ν and B , with the three different equilibrium functions. The average mixture velocity across the channel was recorded, and also the sum of the diffusion velocities, which is defined as $\sum_{\sigma} \rho_{\sigma} (u_{\sigma,x} - u_x)$. By definition the sum of the diffusion velocities should always be zero, but this was not observed exactly. The value of either ν or B should not affect the result, which should be one of zero mixture velocity everywhere. Figure 7.4 shows the mixture velocities recorded. As the value of B is increased, ϵ_{ma} (if defined using the species velocity) decreases, and the results become more accurate. The MCE is fairly accurate, but does not consistently improve with values of B above a certain limit. The SCE shows a comparable accuracy, but again does not behave in a predictable way. The CSCE is of comparable accuracy to the other two, and exhibits equally unpredictable behaviour. It should be noted that the range of stable values of B for the MCE is far greater than the other two. In fact, the method is still stable with the value of ϵ_{ma} in excess of 10! This is because the species velocity does not appear in the equilibrium function, and so the species velocity should not strictly be used in the definition of ϵ_{ma} . The MCE is still stable at higher values of B but the computational time increases dramatically.

Figure 7.5 shows the sum of the diffusion velocities. The results broadly reflect the conclusions reached from the results for the mixture velocity; at low values of B the results are less accurate. At this stage it is not clear which equilibrium function is superior, although the MCE has a much greater range of stable values.

Figure 7.6 and 7.7 show the same metrics but this time on a flow with a total pressure gradient. The value of ν is fixed, while B is varied. The fact that the SCE does not recover the correct mixture equation is obvious, and the error in mixture velocity is large. The

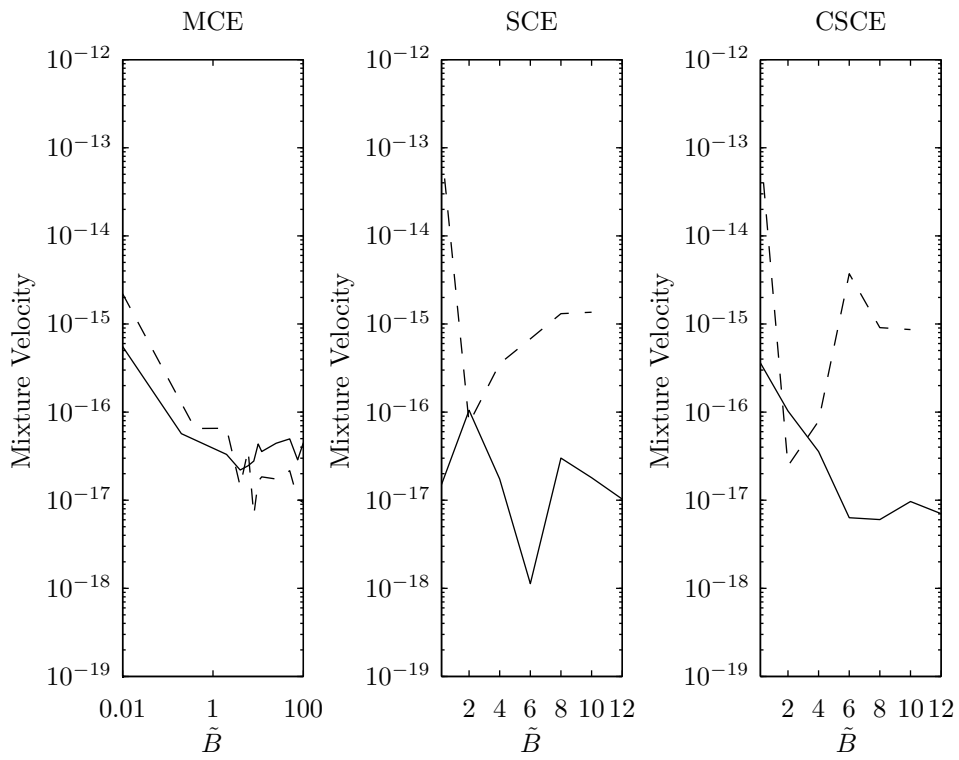


Figure 7.4: Mixture velocity recorded with different equilibrium functions and viscosities for self diffusion with no total pressure gradient. The dotted line is for $\tilde{\nu} = 25$ and the solid line is for $\tilde{\nu} = 1$.

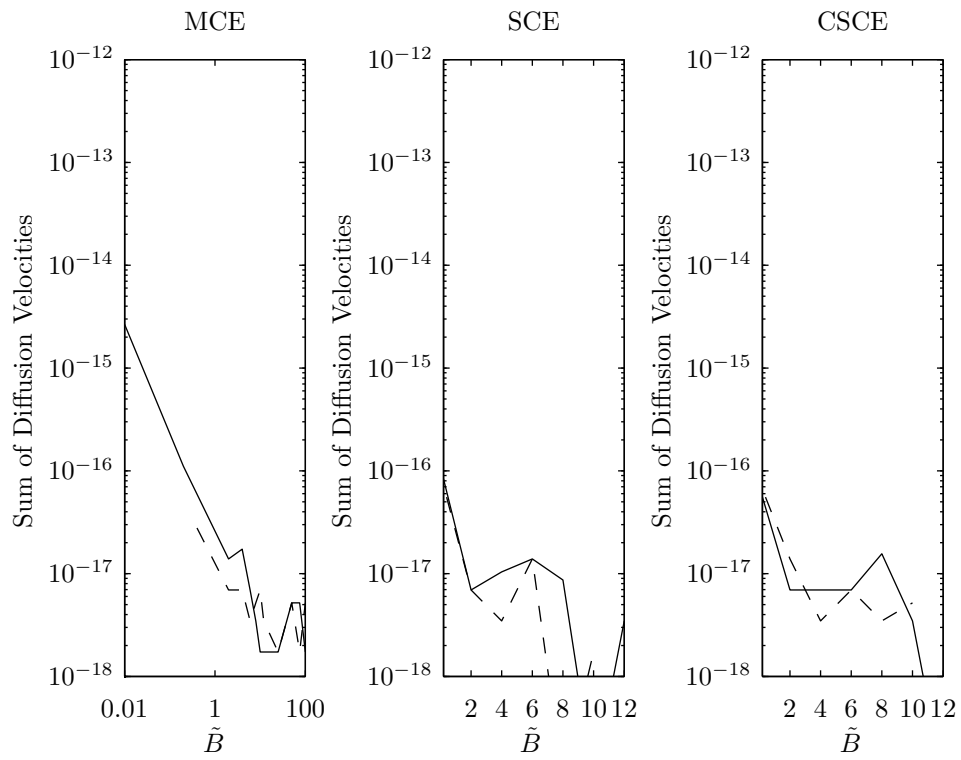


Figure 7.5: Sum of diffusion velocities recorded with different equilibrium functions and viscosities for self diffusion with no total pressure gradient. The dotted line is for $\tilde{\nu} = 25$ and the solid line is for $\tilde{\nu} = 1$.

corrections made in the CSCE function have helped slightly, and if the stability allowed for greater values of B it is possible the accuracy would improve, In practice, however, it does not. The MCE gives a considerably more accurate mixture velocity than the others.

In Figure 7.7 The sum of the diffusion velocities appears to show that the MCE is the least accurate but this is actually due to the extended range of stable values of B . For the same value of B all the equilibrium functions exhibit broadly comparable accuracy. Worryingly, the accuracy of this metric decreases with increasing B for the MCE, while the accuracy of the total mixture velocity increases.

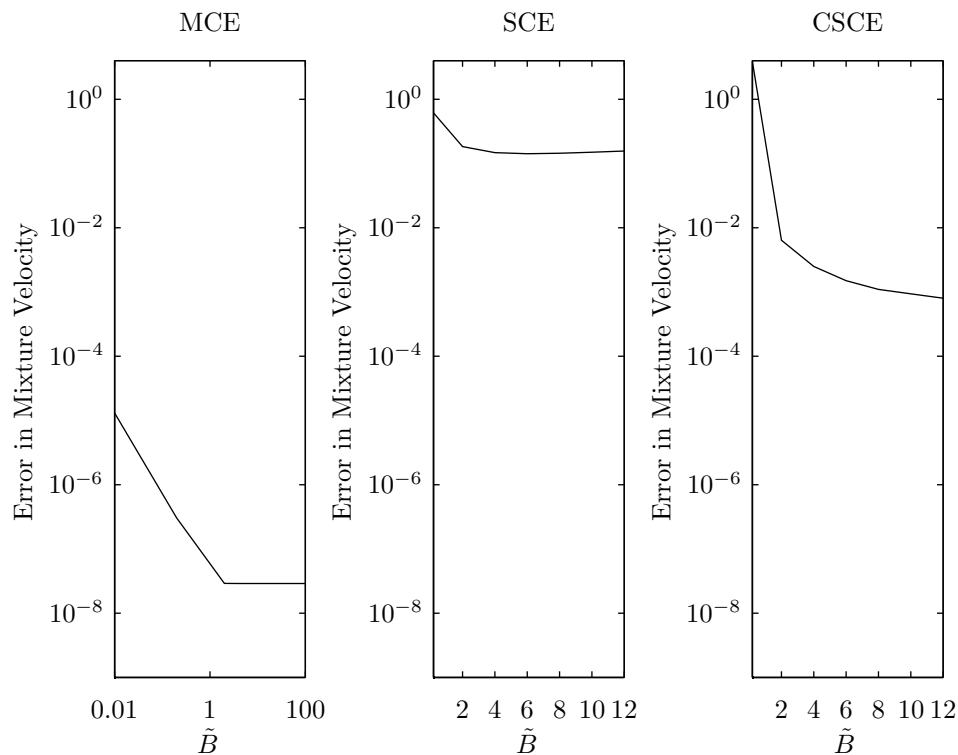


Figure 7.6: Mixture velocity recorded with different equilibrium functions for self diffusion with a total pressure drop of 10^{-4} .

Real problems do not allow the luxury of changing the values of B and ν independently, and it cannot be guaranteed that these values will fall in a regime of high accuracy. Also, with species of different molar masses, it may be impossible to ensure that both species will be in an accurate regime at the same time.

In conclusion, none of the equilibrium functions is entirely satisfactory. In the rest of this

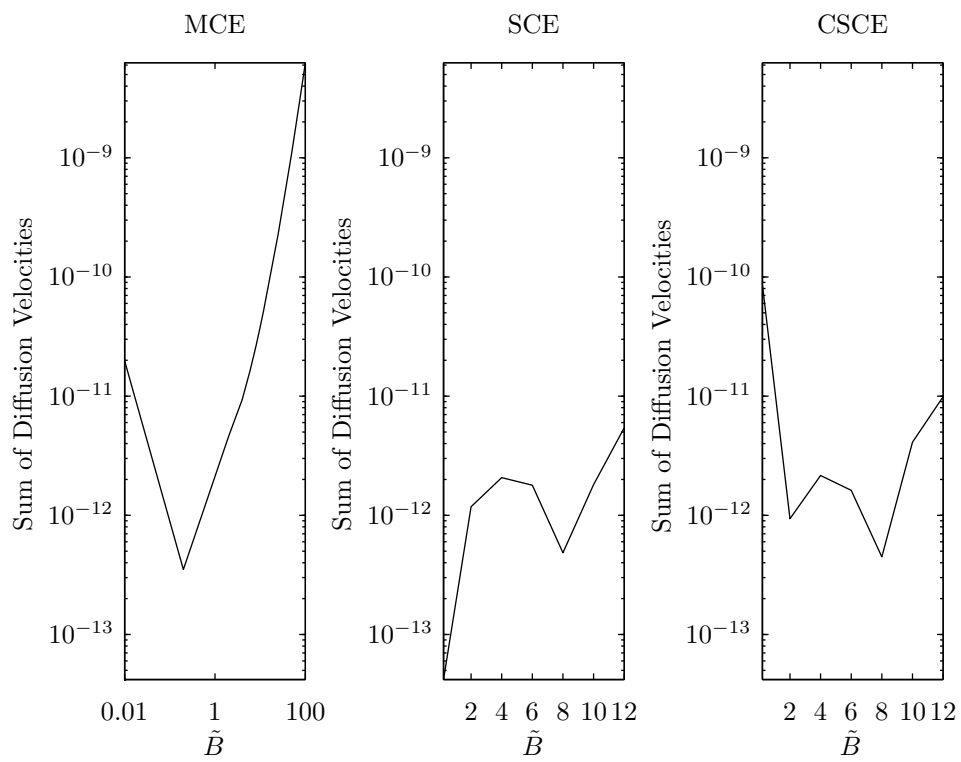


Figure 7.7: Sum of diffusion velocities recorded with different equilibrium functions for self diffusion with a total pressure drop of 10^{-4} .

work the MCE is used, because of the much greater stability range. There are also some simplifications which offer an advantage when the advanced implementation of Chapter 8 is used.

7.9 A dimensional test case

To understand the effect of scaling, it is important to consider a dimensional test case. Here the physical problem is fixed and then different scaling values are chosen to try to recover the correct solution. The problem to be investigated is diffusion of hydrogen and water vapour in a channel, involving both diffusion slip at the walls and a total pressure gradient along the channel. The physical data is given in Table 7.1.

Channel Length	1×10^{-5} m
Channel Height	1×10^{-5} m
Average Pressure	1×10^5 Pa
Total Pressure drop	10 Pa
Mole fraction Hydrogen at Inlet	0.55
Mole fraction Hydrogen at Outlet	0.45
Temperature	300 K
B_{H_2,H_2O}	1.0789×10^4 s m ⁻²
Viscosity of Hydrogen (at 25°C)	8.81×10^{-6} kg m ⁻¹ s ⁻¹
Viscosity of Water Vapour (at 25°C)	9.40×10^{-6} kg m ⁻¹ s ⁻¹

Table 7.1: Physical data for the example problem

The viscosity of the mixture is calculated using the method of Wilke and Fuller as described by Poling et al. (2000). Evaluating the size of the terms in Equation 7.9, the ordinary diffusion term is more than a thousand times larger than the pressure diffusion term for this problem. The Knudsen number is of the order of 0.01, which is small enough that there is no viscous slip at the wall. Therefore, the results obtained from the LB method can be compared with the numerical integration of the governing continuum fluid flow equations, performed by the method described by Young and Todd (2005), which neglects pressure diffusion. These results are shown in Table 7.2. Because both methods

are numerical in nature, exact agreement between the two is not expected.

Mixture Velocity	-1.3935 m/s
Hydrogen Velocity	1.9404 m/s
Water Vapour Velocity	-1.7672 m/s
Mixture Wall Slip Velocity	-0.55625 m/s

Table 7.2: Solution obtained by the numerical integration method of Young and Todd (2005) for the problem described in Table 7.1

The MCE equilibrium function was used for all calculations and the criteria for the convergence was based on the change between time steps of the total momentum within the domain becoming zero to machine accuracy. The values of \tilde{RT}_{H_2} for different values of c and N_x , the number of grid points forming one side of the square domain, are shown in Table 7.3. All the values in the table are less than one third, and so it is likely that a stable solution will be found for all cases considered.

c	N_x		
	30	60	90
2000	3.12×10^{-1}	3.12×10^{-1}	3.12×10^{-1}
8000	1.95×10^{-2}	1.95×10^{-2}	1.95×10^{-2}
32000	1.22×10^{-3}	1.22×10^{-3}	1.22×10^{-3}
128000	7.61×10^{-5}	7.61×10^{-5}	7.61×10^{-5}
512000	4.76×10^{-6}	4.76×10^{-6}	4.76×10^{-6}

Table 7.3: $(\tilde{RT})_{H_2}$ calculated at different values of c and N_x

c	N_x		
	30	60	90
2000	3.714	7.428	1.114
8000	0.929	0.186	2.786
32000	0.232	0.464	0.696
128000	0.058	0.116	0.174
512000	0.015	0.029	0.044

Table 7.4: $\tilde{\nu}$ calculated at different values of c and N_x

c	N_x		
	30	60	90
2000	0.072	0.036	0.024
8000	0.288	0.144	0.096
32000	1.151	0.575	0.384
128000	4.603	2.301	1.534
512000	18.412	9.206	6.137

Table 7.5: B_{H_2,H_2O} calculated at different values of c and N_x

The dimensionless viscosity and diffusion resistance are shown in Tables 7.4 and 7.5. A large value of \tilde{B} was shown to improve the accuracy of the method in Section 7.8. Increasing the number of grid points reduces the value of \tilde{B} , and increasing the value of c increases it.

c	Mixture Velocity			Hydrogen Velocity			Water velocity		
	N_x			N_x			N_x		
	30	60	90	30	60	90	30	60	90
2000	-1.7258	-1.5537	-1.4964	3.6520	2.8026	2.5190	-2.3360	-2.0451	-1.9485
8000	-1.4728	-1.4274	-1.4122	2.3661	2.1587	2.0894	-1.9089	-1.8322	-1.8066
32000	-1.4094	-1.3958	-1.3911	2.0454	1.9979	1.9821	-1.8020	-1.7789	-1.7712
128000	-1.3935	-1.3879	-1.3859	1.9653	1.9577	1.9553	-1.7753	-1.7656	-1.7623
256000	NS	-1.3865	-1.3850	NS	1.9510	1.9508	NS	-1.7634	-1.7608
384000	NS	-1.3861	-1.3847	NS	1.9488	1.9493	NS	-1.7626	-1.7603

Table 7.6: Average velocities [m/s] of the mixture and species for the problem described in Table 7.1 with diffusive slip boundary condition. NS means the solution was not stable.

The results of the simulations are shown in Table 7.6. The agreement with Table 7.2 is very poor with few grid points and low values of c but improves with higher values. The rate of convergence is first order. The highest stable value of c is a function of the number of grid points, and increases with number of grid points.

Also recorded was the number of site updates until the solution had converged. This was defined as the number of grid points multiplied by the number of iterations, and this is shown in Table 7.7. There is a disproportionate penalty to pay for a large number of grid points as more iterations are needed as well as there being more points. An accurate

c	N_x		
	30	60	90
2000	3.690×10^7	2.844×10^8	9.477×10^8
8000	1.413×10^8	1.062×10^9	3.507×10^9
32000	6.030×10^8	4.136×10^9	1.308×10^{10}
128000	2.428×10^9	1.756×10^{10}	5.318×10^{10}
256000	NS	3.585×10^{10}	1.100×10^{11}
384000	NS	5.350×10^{10}	1.678×10^{11}

Table 7.7: Total site updates to convergence

solution required at least 2.5×10^9 site updates, taking approximately an hour on a standard desktop computer, and the accurate solutions with finer grids took 100 times longer. Comparing this with the results for the single-component solution, which took a minimum of 1.9×10^7 site updates to reach an accurate solution, it is clear that the extension to multi-component mixtures has come at significant cost.

The maximum physical size of the grid spacing in these simulations was 300 nm, and this seems close to the maximum physical size of the grid spacing for any problem. This would certainly restrict the method to very small scale applications or very large computers.

7.9.1 Alternative boundary conditions

The test case was repeated with alternative boundary conditions of zero mixture slip velocity and zero species slip velocity. To obtain zero mixture slip $S(M_\sigma)$ was set to 1 in Equation (7.38). The results are shown in Table 7.8. The mixture velocity is nearly constant with c , while the species velocity requires a much higher value of c before it is consistent. This is because the boundary condition for the mixture does not depend on the species velocity, as the diffusive slip condition does. Separating the mixture and species velocity in this way makes it clear that the mixture velocity, and not the species velocity, demonstrates a second order convergence rate.

The boundary condition that is often used for multi-component simulations in the LB literature is that the species velocity at the wall is zero, leading to the mixture velocity

c	Mixture Velocity			Hydrogen Velocity			Water velocity		
	N_x			N_x			N_x		
	30	60	90	30	60	90	30	60	90
2000	-0.837	-0.835	-0.834	4.517	3.511	3.174	-1.447	-1.327	-1.287
8000	-0.837E	-0.835	-0.834	2.991	2.745	2.663	-1.273	-1.241	-1.230
32000	-0.837E	-0.835	-0.834	2.609	2.553	2.535	-1.229	-1.219	-1.215
128000	-0.8.37	-0.835	-0.834	2.514	2.505	2.503	-1.219	-1.213	-1.212
256000	NS	-0.835	-0.834	NS	2.498	2.497	NS	-1.213	-1.211
384000	NS	-0.835	-0.834	NS	2.495	2.496	NS	-1.212	-1.211

Table 7.8: Velocity [m/s] with zero mixture slip boundary condition

also being zero. This was obtained by setting the slip velocity to zero in the method described in Section 6.1.1. Results for this boundary condition are shown in Table 7.9. The mixture velocity is the same as the results from the zero mixture slip boundary, as would be expected. The species velocities are slightly different from the zero mixture slip case, the magnitude of this difference depending on the problem being considered. As with the previous calculations the rate of convergence of the mixture velocity is second order, while for the species velocity it is only first order. This means the source of the error is not due to the expression for the diffusion slip velocity at the wall.

c	Mixture Velocity			Hydrogen Velocity			Water velocity		
	N_x			N_x			N_x		
	30	60	90	30	60	90	30	60	90
2000	-0.837	-0.835	-0.834	4.410	3.425	3.094	-1.435	-1.317	-1.278
8000	-0.837	-0.835	-0.834	2.914	2.674	2.593	-1.264	-1.232	-1.222
32000	-0.837	-0.835	-0.834	2.540	2.486	2.467	-1.222	-1.211	-1.207
128000	-0.837	-0.835	-0.834	2.447	2.439	2.436	-1.211	-1.206	-1.204
256000	NS	-0.835	-0.834	NS	2.431	2.431	NS	-1.205	-1.203
384000	NS	-0.835	-0.834	NS	2.428	2.429	NS	-1.205	-1.203

Table 7.9: Velocity [m/s] with no species slip boundary condition

7.10 Conclusions

Three different equilibrium functions were considered for multi-component gases. The Mixture Centred Equilibrium (MCE) function had the widest stability range, and was selected as the preferred model. The Navier-Stokes equations for the mixture are recovered in terms of a mixture viscosity. The Stefan-Maxwell equation and the ‘pressure diffusion’ equation were recovered for the species velocities. An expression was developed for diffusive slip boundaries, using the moment-based boundary method.

Although the MCE scheme with diffusive boundaries gives results consistent with the work of Young and Todd (2005) for binary channel flow, the convergence of the species velocity is only first order. This does not make the scheme a feasible tool for real applications. In fact, the source of this error was the assumption that $\Pi_X^{(eq)+} = \Pi_X^{(eq)}$ made before Equation (7.60). Because the species momentum is not conserved during the collision this assumption is incorrect. The error term is proportional to the size of the time step, and so as the time step reduces the error reduces also. In the next chapter a second order numerical integration scheme will be used which eliminates this error. These results show that when the LB method is applied to a problem where the momentum is not conserved over a time step, the simple forward Euler integration is not sufficient to ensure second order accuracy.

Chapter 8

Improvements to Multi-component Methods

In Chapter 7 a continuous LB model was derived which recovered the steady-state macroscopic equations for a multi-component gas mixture. However, when this scheme was numerically integrated using the forward Euler scheme, it was found to be only first order accurate. In Chapter 6 the single-component scheme developed was second order accurate. However, for large time steps the scheme was unstable meaning that the computational time could not be reduced at the expense of spurious accuracy. In this chapter both these issues are addressed. Firstly, a second order accurate scheme is used to ensure the species velocity is second order convergent. Secondly, a pre-conditioning method is used to enable calculations to be performed with much larger time steps.

In this chapter all variables are in the computation scale, and for clarity the $\tilde{\cdot}$ is omitted.

8.1 Second order scheme

8.1.1 Crank-Nicolson integration

To avoid numerical errors, and obtain second order accuracy for the species velocity, He et al. (1998), Asinari (2006) and Dellar (2002b) propose the use of the Crank-Nicolson rule

to replace Equation (5.21),

$$\mathbf{f}_\sigma^+ = \mathbf{f}_\sigma + \frac{1}{2}\mathbf{A}(\mathbf{f}_\sigma^{(eq)} - \mathbf{f}_\sigma) + \frac{1}{2}\mathbf{A}^{(+)}(\mathbf{f}_\sigma^{(eq)+} - \mathbf{f}_\sigma^+) \quad (8.1)$$

where the + superscript is the post collision and streaming state, and $\mathbf{A} = \mathbf{M}^{-1}\mathbf{\Lambda}\mathbf{M}$. Equation (8.1) is an implicit expression for \mathbf{f}_σ^+ , and threatens to ruin the explicit nature of the LBM. Fortunately a transformation to a new variable \mathbf{g}_σ can be used,

$$\mathbf{g}_\sigma = \mathbf{f}_\sigma - \frac{1}{2}\mathbf{A}(\mathbf{f}_\sigma^{(eq)} - \mathbf{f}_\sigma) \quad (8.2)$$

Substituting Equation (8.2) into Equation (8.1),

$$\mathbf{g}_\sigma^+ = \mathbf{g}_\sigma - \mathbf{A}(\mathbf{I} + \frac{1}{2}\mathbf{A})^{-1}(\mathbf{f}_\sigma^{(eq)} - \mathbf{g}_\sigma) \quad (8.3)$$

where \mathbf{I} is the identity matrix. This equation may be used directly, or alternatively in the form,

$$\mathbf{g}_\sigma^+ = \mathbf{g}_\sigma - \mathbf{A}'(\mathbf{f}_\sigma^{(eq)} - \mathbf{g}_\sigma) \quad (8.4)$$

where \mathbf{A}' is a modified form of \mathbf{A} , such that each value of λ is replaced with $\lambda/(1 + \lambda/2)$. Therefore, in effect, the algorithm used so far is unchanged, except that the vector \mathbf{f}_σ is replaced by \mathbf{g}_σ . The following identities arise directly from Equation (8.2) when the MCE model is used, for simplicity $\lambda^\xi = \lambda^\nu$, so the matrix $\mathbf{\Lambda}$ is diagonal.

$$\sum_i g_{\sigma,i} = \sum_i f_{\sigma,i} = \rho_\sigma \quad (8.5)$$

The sum over i of $g_{\sigma,i}$ is equal to the sum over i of $f_{\sigma,i}$ as the species density is conserved during the collision. However momentum is not, and a new velocity $\ddot{u}_{\sigma,x}$, defined as $\rho_\sigma \ddot{u}_{\sigma,\alpha} = \sum_i e_{\alpha,i} g_{\sigma,i}$, is introduced. Using Equation (8.2) yields,

$$\rho_\sigma \ddot{u}_{\sigma,\alpha} = \rho_\sigma u_{\sigma,\alpha} - \frac{\lambda^\delta}{2} \rho_\sigma (u_\alpha - u_{\sigma,\alpha}) \quad (8.6)$$

Summing over all the species, momentum is conserved, and $\sum_{\sigma} \rho_{\sigma} \ddot{u}_{\sigma,\alpha} = \rho u_{\alpha}$. Using $\Phi_{\sigma,\alpha\beta}$ to represent the equivalent of the momentum flux density tensor calculated from \mathbf{g}_{σ} (i.e. $\sum_i e_{\alpha,i} e_{\beta,i} g_{\sigma,i} = \Phi_{\sigma,\alpha\beta}$),

$$\Phi_{\sigma,\alpha\beta} = \Pi_{\sigma,\alpha\beta} - \frac{\lambda^{\nu}}{2} (\Pi_{\sigma,\alpha\beta}^{(eq)} - \Pi_{\sigma,\alpha\beta}) \quad (8.7)$$

Only when $\Pi_{\sigma,\alpha\beta} = \Pi_{\sigma,\alpha\beta}^{(eq)}$ does $\Phi_{\sigma,\alpha\beta} = \Pi_{\sigma,\alpha\beta}$.

Once the calculation is complete ρ_{σ} can be calculated directly from the values of \mathbf{g}_{σ} , but u_{σ} must be calculated from \ddot{u}_{σ} using Equation (8.6). Aside from this calculation, which only needs to be performed once, there is no additional computational demand from the variable substitution method. However, the boundary conditions must be rewritten in terms of \mathbf{g}_{σ} , an exercise which is conceptually simple yet algebraically overwhelming.

8.1.2 Diffusion slip boundary

Unfortunately, the use of the variable transform method adds another layer of complexity to the treatment of boundaries. In general (when Λ cannot be expressed as a scalar multiplying the identity matrix, as in the single relaxation time model), Equation (8.2) cannot be used to convert from \mathbf{g}_{σ} to \mathbf{f}_{σ} if there are unknown values of \mathbf{f}_{σ} . Therefore, the boundary conditions must be reformulated in terms of \mathbf{g}_{σ} , instead of \mathbf{f}_{σ} .

For the wall boundary condition the approach of Section 7.6.1 is repeated in terms of \mathbf{g}_{σ} . Equation (8.6) becomes, using $\rho u = \rho_A \ddot{u}_A + \rho_B \ddot{u}_B$,

$$u_A = \ddot{u}_A + \left(\frac{\frac{\lambda^{\delta}}{2}}{1 + \frac{\lambda^{\delta}}{2}} \right) \frac{\rho_B}{\rho_A + \rho_B} (\ddot{u}_B - \ddot{u}_A) \quad (8.8)$$

$$u_B = \ddot{u}_B + \left(\frac{\frac{\lambda^{\delta}}{2}}{1 + \frac{\lambda^{\delta}}{2}} \right) \frac{\rho_A}{\rho_A + \rho_B} (\ddot{u}_A - \ddot{u}_B) \quad (8.9)$$

This may be substituted into the macroscopic boundary conditions from Section 7.6 , $\sum_{\sigma} (\rho_{\sigma} u_{\sigma,x} / S(M_{\sigma})) = 0$, to obtain a condition for \ddot{u}_{σ} ,

$$\ddot{u}_A = - \frac{\rho_B (\lambda^{\delta} (\rho_A S(M_B) + \rho_B S(M_A)) + 2(\rho_A + \rho_B) S(M_A))}{\rho_A (\lambda^{\delta} (\rho_A S(M_B) + \rho_B S(M_A)) + 2(\rho_A + \rho_B) S(M_B))} \ddot{u}_B \quad (8.10)$$

Equation (8.7) yields an expression for the XY momentum flux,

$$\Phi_{XY} = \Pi_{XY} - \frac{1}{2}\lambda^\nu(\Pi_{XY}^{(eq)} - \Pi_{XY}) \quad (8.11)$$

Which, when combined with the macroscopic boundary conditions from Section 7.6, $\Pi_{A,XY}/\rho_A = \Pi_{B,XY}/\rho_B$, becomes

$$\frac{1}{\rho_A}(\Phi_{A,XY} - \frac{1}{2}\lambda^\nu\Pi_{A,XY}^{(eq)}) = \frac{1}{\rho_B}(\Pi_{B,XY} - \frac{1}{2}\lambda^\nu\Pi_{B,XY}^{(eq)}) \quad (8.12)$$

If either the SCE or CSCE model were used it would lead to yet more complexity, as u_σ appears in the expression for $\Pi_{\sigma,XY}$. However in the MCE model $\Pi_{\sigma,XY}^{(eq)} = \rho_\sigma u_x u_y$, leading to a cancellation of the $\Pi_{\sigma,XY}^{(eq)}$ terms and Equation (8.12) becomes,

$$\frac{1}{\rho_A}(\Phi_{A,XY}) = \frac{1}{\rho_B}(\Phi_{B,XY}) \quad (8.13)$$

which may be written in terms of the elements of \mathbf{g}_A and \mathbf{g}_B ,

$$\frac{1}{\rho_A}(g_{A,5} - g_{A,6} + g_{A,7} - g_{A,8}) = \frac{1}{\rho_B}(g_{B,5} - g_{B,6} + g_{B,7} - g_{B,8}) \quad (8.14)$$

The \ddot{u} values are defined by,

$$g_{\sigma,5} - g_{\sigma,6} = \rho_\sigma \ddot{u}_{\sigma,x} - g_{\sigma,1} - g_{\sigma,8} + g_{\sigma,3} + g_{\sigma,7} \quad (8.15)$$

and substituting this into Equation (8.14) yields,

$$\frac{1}{\rho_A}(\rho_A \ddot{u}_{A,x} - g_{A,1} - 2g_{A,8} + g_{A,3} + 2g_{A,7}) = \frac{1}{\rho_B}(\rho_B \ddot{u}_{B,x} - g_{B,1} - 2g_{B,8} + g_{B,3} + 2g_{B,7}) \quad (8.16)$$

A new variable is introduced, $\ddot{\kappa}_\sigma = -g_{\sigma,1} - 2g_{\sigma,8} + g_{\sigma,3} + 2g_{\sigma,7}$ equivalent to the κ_σ defined in Section 7.6 in terms of f . Using Equation (8.10) to eliminate $\ddot{u}_{B,x}$ yields an expression

for $\ddot{u}_{A,x}$ purely in terms of known values,

$$\rho_A \ddot{u}_{A,x} \left(\frac{1}{\rho_A} + \frac{1}{\rho_B} \frac{(\lambda(\rho_A S(M_B) + \rho_B S(M_A)) + 2(\rho_A + \rho_B)S(M_B))}{(\lambda(\rho_A S(M_B) + \rho_B S(M_A)) + 2(\rho_A + \rho_B)S(M_A))} \right) = \frac{1}{\rho_B}(\kappa_B) - \frac{1}{\rho_A}(\kappa_A) \quad (8.17)$$

To impose this value of $\ddot{u}_{A,x}$ on the wall, the method discussed in Section 6.1.1 is used. Noting that if $u_{\sigma,y} = 0$, $\ddot{u}_{\sigma,y} = 0$ and if $\Pi_{\sigma,XX} = \Pi_{\sigma,XX}^{(eq)}$ then $\Phi_{\sigma,XX} = \Pi_{\sigma,XX}^{(eq)}$, the references to \mathbf{f}_σ in Equations (6.23) may be swapped for \mathbf{g}_σ .

8.1.3 Other boundaries

At an open boundary ρ_σ is set to a specific value, $u_{\sigma,y} = 0$ and $\Pi_{\sigma,YY} = \Pi_{\sigma,YY}^{(eq)}$, similar to the conditions used in Chapter 6. In terms of g these conditions are the same, specifically $\ddot{u}_{\sigma,y} = 0$ and $\Phi_{\sigma,YY} = \Pi_{\sigma,YY}^{(eq)}$. Therefore the same conditions already developed in Section 6.1.1 may be used, substituting \mathbf{g}_σ for \mathbf{f}_σ in Equation (6.24).

It may be desirable to set the mass flux, instead of the density, as a boundary condition. For given values of $\rho_\sigma \ddot{u}_{\sigma,x}$, the value of ρ_σ is not uniquely defined. If this value of ρ_σ can be determined it can be used in conjunction with the method from the previous paragraph.

In a corner of the type shown in Figure 5.2, $\rho_\sigma \ddot{u}_{\sigma,x}$ and ρ_σ are linked by the equations,

$$\rho_\sigma(1 + \ddot{u}_{\sigma,x}) = g_{\sigma,0} + g_{\sigma,2} + g_{\sigma,4} + 2(g_{\sigma,1} + g_{\sigma,5} + g_{\sigma,8}) = \Upsilon_\sigma \quad (8.18)$$

Where Υ_σ is a shorthand involving only the known values of \mathbf{g}_σ . The values of \ddot{u}_σ are given by,

$$\rho_A \ddot{u}_{A,x} = \rho_A u_{A,x} - \frac{\lambda^\delta}{2} \rho_A (u_x - u_{A,x}) \quad (8.19)$$

$$\rho_B \ddot{u}_{B,x} = \rho_B u_{B,x} - \frac{\lambda^\delta}{2} \rho_B (u_x - u_{B,x}) \quad (8.20)$$

Substituting Equation (8.18) into Equations (8.19) and (8.20) yields,

$$\Upsilon_A - \rho_A = \rho_A u_{A,x} - \frac{\lambda^\delta}{2} \rho_A (u_x - u_{A,x}) \quad (8.21)$$

$$\Upsilon_B - \rho_B = \rho_B u_{B,x} - \frac{\lambda^\delta}{2} \rho_B (u_x - u_{B,x}) \quad (8.22)$$

which can be summed over the species to give

$$\Upsilon_A + \Upsilon_B - \rho = \rho u_x \quad (8.23)$$

If Υ_σ and ρu_x are known, the value of ρ can be determined, which allows the known value of ρu_x to be split and u_x to be recovered. The only unknowns remaining in Equations (8.21) and (8.22) are the species densities. Rearranging Equation (8.23) gives,

$$\rho_A = \frac{\Upsilon_A - \rho_A u_{A,x} (1 + \frac{\lambda^\delta}{2})}{1 - \frac{\lambda^\delta}{2} u_x} \quad (8.24)$$

and a similar expression can be obtained for ρ_B . In fact, the situation is more complicated than it appears, as λ^δ is itself a function of the species densities through Equation (7.25). To circumvent this problem the species density from the same grid point at the previous time step is used. Although a proper solution could be found this would add additional complexity, and seems to give no corresponding benefit.

8.1.4 Intersection between a wall and another boundary

Open boundaries with known densities

Following the approach of Section 7.6.2, but in terms of \mathbf{g}_σ , the following conditions are true for the \mathbf{g}_σ values at a corner node at the intersection of an open boundary and a wall,

if the density at the open boundary is known.

$$g_{\sigma,1} + g_{\sigma,2} + g_{\sigma,5} + g_{\sigma,6} + g_{\sigma,8} = \rho_{\sigma} - g_{\sigma,3} - g_{\sigma,4} - g_{\sigma,7} - g_{\sigma,0} \quad (8.25)$$

$$g_{\sigma,1} + g_{\sigma,5} + g_{\sigma,8} - g_{\sigma,6} = \rho_{\sigma} \ddot{u}_{\sigma,x} + g_{\sigma,3} + g_{\sigma,7} \quad (8.26)$$

$$g_{\sigma,2} + g_{\sigma,6} + g_{\sigma,5} - g_{\sigma,8} = g_{\sigma,7} + g_{\sigma,4} \quad (8.27)$$

Introducing the new variable $\ddot{\Theta}_{\sigma} = 4g_{\sigma,7} + g_{\sigma,0} + 2g_{\sigma,3} + 2g_{\sigma,4}$, then the equivalent of Equation (7.55) is,

$$(\ddot{\Theta}_A - \rho_A + \rho_A \ddot{u}_{A,x}) \frac{1}{\rho_A} = (\ddot{\Theta}_B - \rho_B + \rho_B \ddot{u}_{B,x}) \frac{1}{\rho_B} \quad (8.28)$$

Substituting Equation (8.10) leaves an expression for the value of $\ddot{u}_{A,x}$ to be imposed at the corner node,

$$\ddot{u}_{A,x} \left(1 + \frac{\rho_A (\lambda^{\delta} (\rho_A S(M_B) + \rho_B S(M_A)) + 2(\rho_A + \rho_B) S(M_B))}{\rho_B (\lambda^{\delta} (\rho_A S(M_B) + \rho_B S(M_A)) + 2(\rho_A + \rho_B) S(M_A))} \right) = \frac{1}{\rho_B} (\ddot{\Theta}_B - \rho_B) - \frac{1}{\rho_A} (\ddot{\Theta}_A - \rho_A) \quad (8.29)$$

To impose this, the approach from Section 6.1.1, with $f_{\sigma,i}$ values swapped for $g_{\sigma,i}$ values, is used.

Open boundaries with known mass flux

If the open boundary that intersects the corner is specified by a mass flux rather than a density condition, the diffusion slip condition for these nodes cannot be applied. Therefore, the values of $\rho_{\sigma} u_{\sigma,x}$ are known, and $u_{\sigma,y} = 0$, $\Pi_{\sigma,Y Y} = \rho_{\sigma} (RT)_{\sigma}$ and $\Pi_{\sigma,X X} = \rho_{\sigma} (RT)_{\sigma} + \rho_{\sigma} u_x^2$. As there are five unknown g values there must be five constraints, the final condition being $\Pi_{\sigma,X Y} = 0$. Certainly, along the wall $\partial \rho_{\sigma} u_y / \partial x = 0$, however along the open boundary $\partial \rho_{\sigma} u_x / \partial y$ is only zero if the mass flux is constant. If a non-constant mass flux profile is to be used, a specific value of $\Pi_{\sigma,X Y} = 0$ must be supplied. At the corner, the density and

modified velocity are related by,

$$\rho_\sigma + \rho_\sigma \ddot{u}_{\sigma,x} = \ddot{\Theta}_\sigma \quad (8.30)$$

Following the approach of Section 8.1.3 the density can be found as,

$$\rho_A = \frac{\ddot{\Theta}_A - \rho_A u_{A,x} (1 + \frac{\lambda^\delta}{2})}{1 - \frac{\lambda^\delta}{2} u_x} \quad (8.31)$$

For example the \mathbf{g}_σ values to be imposed at a corner with $g_{\sigma,3}$ $g_{\sigma,4}$ and $g_{\sigma,7}$ known are,

$$g_{\sigma,1} = -g_{\sigma,0} - g_{\sigma,3} + (1 - (RT)_\sigma) \rho_\sigma \quad (8.32)$$

$$g_{\sigma,2} = -g_{\sigma,0} - g_{\sigma,4} - ((RT)_\sigma + u_x^2 - 1) \rho_\sigma \quad (8.33)$$

$$g_{\sigma,5} = \frac{1}{2} g_{\sigma,0} - g_{\sigma,7} + \left((RT)_\sigma + \frac{1}{2} (u_x^2 - 1) \right) \rho_\sigma \quad (8.34)$$

$$g_{\sigma,6} = \frac{1}{2} g_{\sigma,0} + g_{\sigma,4} + g_{\sigma,7} + \left(\frac{1}{2} (RT)_\sigma + u_x^2 - 1 \right) \rho_\sigma \quad (8.35)$$

$$g_{\sigma,8} = -g_{\sigma,4} - g_{\sigma,7} + \frac{1}{2} (RT)_\sigma \rho_\sigma \quad (8.36)$$

8.1.5 Binary channel flow results

The variable substitution method described above was used to solve the problem from Section 7.9. The impressive results are shown in Table 8.1. Once the value of c is high enough such that $\tilde{RT} < 1/3$, ϵ_{Ma} is so small that further reduction does not affect the results. This behaviour is similar to that obtained from the dimensional single-component Poiseuille flow. The use of the variable substitution method has led to a dramatic increase in accuracy, leading to lower computational times.

8.2 Pre-conditioning

The method that has been developed so far is not time accurate, unless $(\tilde{RT})_\sigma = 1/3$ which, for species of different molecular weights, is impossible. Although errors are introduced

c	Mixture Velocity			Hydrogen Velocity			Water velocity		
	30	N_x 60	90	30	N_x 60	90	30	N_x 60	90
1300	-1.720	-1.385	-1.384	1.130	1.944	1.946	-2.051	-1.761	-1.759
2000	-1.388	-1.385	-1.384	1.939	1.944	1.946	-1.766	-1.761	-1.759
3000	-1.388	-1.385	-1.384	1.939	1.944	1.946	-1.766	-1.761	-1.759
4000	-1.388	-1.385	-1.384	1.939	1.944	1.946	-1.766	-1.761	-1.759

Table 8.1: Velocity [m/s] with second order boundary integration. Results using the method of Young and Todd (2005) are Mixture velocity = -1.3935 m/s, Hydrogen Velocity = 1.9404 m/s and Water Vapour velocity = -1.7672 m/s

into the transient solution, the computation will proceed at a pace determined by the physics of the problem. It is desirable to completely sever this link with physical time, and thus produce the quickest possible convergence to the steady state. Verberg and Ladd (1999) suggest one method of doing this, another is a technique known as pre-conditioning, suggested for LBM by Guo et al. (2004) and further refined by Izquierdo and Fueyo (2009). The approach outlined here is a simplification of pre-conditioning, yet it is effective. To accomplish this pre-conditioning all the terms except the time derivative term in the species momentum equation for the MCE model, Equation (7.22), are multiplied by the non-dimensional quantity γ . Thus,

$$\begin{aligned}
\frac{\partial}{\partial t} \begin{pmatrix} \hat{\rho}_\sigma \hat{u}_{\sigma,x} \\ \hat{\rho}_\sigma \hat{u}_{\sigma,y} \end{pmatrix} + \gamma \frac{\partial}{\partial \hat{x}} \begin{pmatrix} \hat{\rho}_\sigma \hat{u}_x^2 \\ \hat{\rho}_\sigma \hat{u}_x \hat{u}_y \end{pmatrix} + \gamma \frac{\partial}{\partial \hat{y}} \begin{pmatrix} \hat{\rho}_\sigma \hat{u}_x \hat{u}_y \\ \hat{\rho}_\sigma \hat{u}_y^2 \end{pmatrix} = -\gamma \begin{pmatrix} \frac{\partial}{\partial \hat{x}} (\hat{p}_\sigma) \\ \frac{\partial}{\partial \hat{y}} (\hat{p}_\sigma) \end{pmatrix} \\
+ \gamma \frac{\partial}{\partial \hat{x}} \begin{pmatrix} \Pi_{\sigma,XX}^{(neq)} \\ \Pi_{\sigma,XY}^{(neq)} \end{pmatrix} + \gamma \frac{\partial}{\partial \hat{y}} \begin{pmatrix} \Pi_{\sigma,XY}^{(neq)} \\ \Pi_{\sigma,YY}^{(neq)} \end{pmatrix} + \gamma \begin{pmatrix} \hat{\lambda}^\delta \hat{\rho}_\sigma (\hat{u}_x - \hat{u}_{\sigma,x}) \\ \hat{\lambda}^\delta \hat{\rho}_\sigma (\hat{u}_y - \hat{u}_{\sigma,y}) \end{pmatrix} \quad (8.37)
\end{aligned}$$

In steady state conditions the time derivative term is zero and the correct momentum equation is recovered. To implement pre-conditioning, modifications must be made to the equilibrium function, (RT) and ν . The modified quantities are indicated with a super-

c	γ				
	0.015	0.030	0.06	0.12	0.24
250	4.72×10^5	2.39×10^5	NS	NS	NS
500	9.06×10^6	4.65×10^5	2.38×10^5	1.21×10^5	NS
750	1.31×10^6	6.76×10^5	3.48×10^5	1.79×10^5	$9.09\text{E} \times 10^4$
1000	1.70×10^6	8.76×10^5	4.54×10^5	2.36×10^5	$1.20\text{E} \times 10^5$

Table 8.2: Number of iterations needed to reach converged solution to the problem from Section 7.9 with different values of c and γ . The accuracy of all solutions were within 0.01% of each other. The diffusive slip boundary condition was used, and the variable transform method of Section 8.1. NS means no solution could be found.

script γ .

$$\Pi_{\sigma,XX}^{eq,\gamma} = p_\sigma + \gamma\rho_\sigma u_x^2 \quad (8.38)$$

$$\Pi_{\sigma,YY}^{eq,\gamma} = p_\sigma + \gamma\rho_\sigma u_y^2 \quad (8.39)$$

$$\Pi_{\sigma,XY}^{eq,\gamma} = \gamma\rho_\sigma u_x u_y \quad (8.40)$$

$$(RT)^\gamma = \gamma(RT) \quad (8.41)$$

$$\nu^\gamma = \gamma\nu \quad (8.42)$$

Both Guo et al. (2004) and Izquierdo and Fueyo (2009) suggest modifications to the Π_{XXYY} moment. However, as this moment does not influence the momentum equation such modifications seem unjustified.

The results shown in Table 8.2 show that the pre-conditioning can have a major impact on the convergence time of the results without reducing accuracy. Higher values of γ with a constant value of c produce quicker convergence. To minimise the convergence time a large value of c and the largest possible value of γ should be selected. However, it is not clear why this is the case.

8.3 Conclusions

In conclusion both the variable transformation method and the pre-conditioning method are highly successful in reducing the computational expense of the multi-component LB model. As such they should both be considered vital components of the model.

Using the variable transformation method requires careful handling of the boundary conditions. It is interesting to note that a bounce-back boundary condition is often used on the values of the new variable g , and this is not necessarily the same condition as bounce-back of the f values. The moment-based boundary conditions for the new variable are no more computationally expensive than the conditions used on the old variables and, crucially they are still local to each node. Implementing pre-conditioning is extremely simple, requiring only minimal changes.

Chapter 9

Calculations of Binary Flow

In this chapter some calculations are performed using the method developed in the previous chapters. These calculations will be loosely themed around fuel cell development and, as such, will involve hydrogen and water vapour diffusion. Some types of hydrogen fuel cell such as the SOFC consist of a reacting surface where oxygen ions, conducted through this surface, react with the hydrogen in the gas mixture to produce water. The hydrogen arrives at the surface by diffusing through a porous material and the water leaves through the same porous material. Each mole of hydrogen that is absorbed will produce one mole of H_2O , therefore at the surface $p_{H_2O}u_{H_2O} = -p_{H_2}u_{H_2}$, which may be written as,

$$\frac{\rho_{H_2}u_{H_2,x}}{\rho_{H_2O}u_{H_2O,x}} = -\frac{M_{H_2}}{M_{H_2O}} \quad (9.1)$$

where M_{H_2} and M_{H_2O} are the molar masses of hydrogen and water respectively. The quantity $\rho_{H_2}u_{H_2,x}/\rho_{H_2O}u_{H_2O,x}$ will be referred to as the species mass flux ratio, and $-M_{H_2}/M_{H_2O}$ is its stoichiometric value. Due to mass conservation of each species, the species mass flux ratio must be maintained *on average* throughout the gas diffusion path. It was shown in Section 7.6 that the diffusion slip boundary forced a different value of mass flux ratio, and so the bulk of the flow must compensate to maintain the average value at the stoichiometric ratio. For the rest of this section the species mass flux ratio is assumed to be averaged across the channel, and is indicated by an overbar such as $\overline{\rho_{H_2}u_{H_2,x}/\rho_{H_2O}u_{H_2O,x}}$.

The water is only considered in the gas phase, because SOFCs operate at high temperatures and pressures. Other types of fuel cell encounter condensation of water vapour, and this effect is beyond the scope of the present work.

9.1 Fully developed binary channel flow

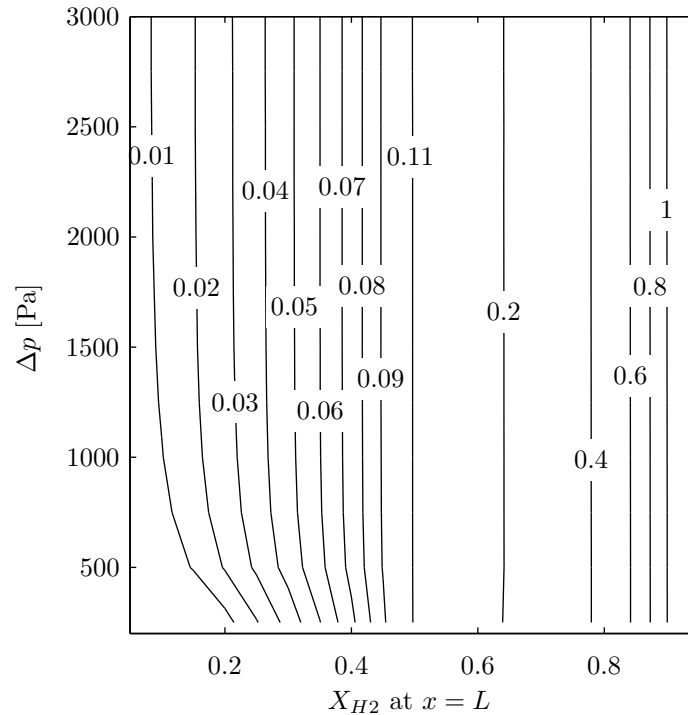


Figure 9.1: Contours of the average species mass flux ratio $(\overline{\rho_{H_2} u_{x,H_2}} / \overline{\rho_{H_2O} u_{x,H_2O}})$ for large values of Δp . For large values of Δp the species mass flux ratio is a function of concentration gradient only. The region between $\Delta p = 200$ and $\Delta p = -200$ is not plotted here, and details of this region may be found in Figure 9.2.

When the partial pressures of the species are set at each end of a channel, using the boundary conditions from Section 7.9, the solution obtained is the binary equivalent of fully-developed single-component flow. That is, the viscous boundary layer at the wall has formed and the velocity profile is parabolic (or, with no total pressure gradient, flat). There is no equivalent of the viscous boundary layer for diffusion.

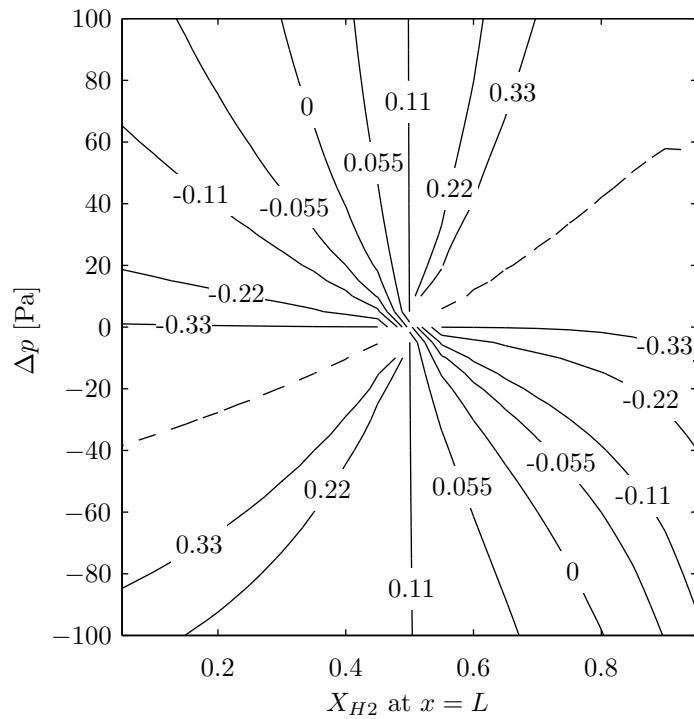


Figure 9.2: Contours of the average species mass flux ratio $(\overline{\rho_{H_2} u_{x,H_2}} / \overline{\rho_{H_2O} u_{x,H_2O}})$ for small values of Δp . The dashed line represents an infinite flux ratio, i.e. $\overline{\rho_{H_2O} u_{x,H_2O}} = 0$. At the central point, when $\Delta p = 0$ and $X_{H_2} = 0.5$, there is a singularity in the flux ratio as both species fluxes tend to zero. Note $\sqrt{M_{H_2}/M_{H_2O}} = 0.3333$ and $M_{H_2}/M_{H_2O} = 0.1111$.

A rectangular domain was considered, with a wall at $y = 0$ and $y = H$. The boundary conditions at $x = 0$ are fixed, with $p = 1$ bar and $X_{H_2} = 0.5$ unless otherwise stated. At $x = L$ different values of total pressure and X_{H_2} were applied. The change in total pressure is defined as $\Delta p = p_{x=L} - p_{x=0}$. The physical size of the domain is $10 \mu\text{m} \times 10 \mu\text{m}$ unless otherwise stated, a grid size of $N_x = 30$ and a grid speed of $c = 6000$ m/s was used.

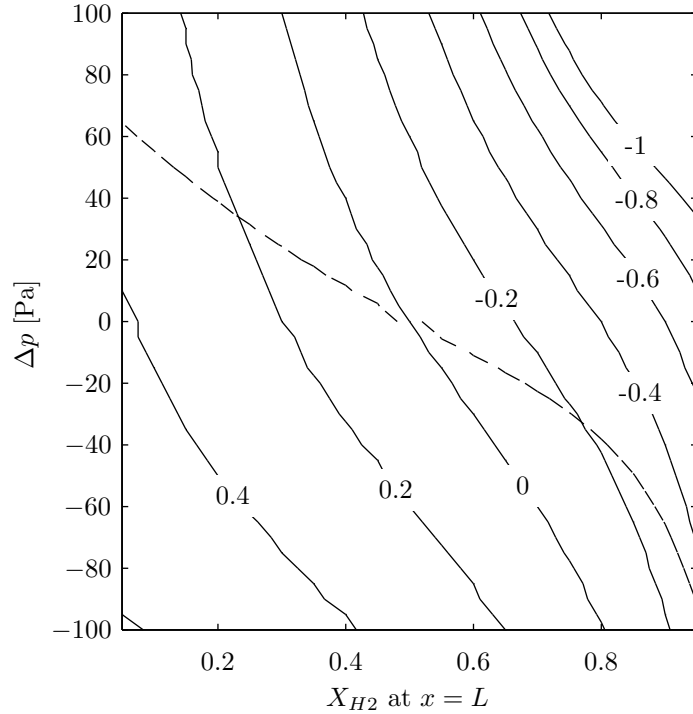


Figure 9.3: Contours of the average mass flux of hydrogen, $\overline{\rho_{H_2} u_{x,H_2}}$ [kg m⁻² s⁻¹], at different pressure and concentration gradients. Along the dashed line the mass flux ratio is stoichiometric.

If the magnitude of the change in total pressure is very large both species are carried in the same direction by the pressure gradient from high pressure to low pressure, and the species mass flux ratio is positive, as shown in Figure 9.1. However, for much smaller values of pressure drop the species concentration gradient begins to play a more important role, and it is possible to obtain negative values for the species mass flux ratio.

Figure 9.2 shows contours of the average species mass flux ratio for different concentration and pressure gradients. If there is zero total pressure gradient the species velocity is governed by the diffusion slip wall boundary condition, and the species mass flux ratio is

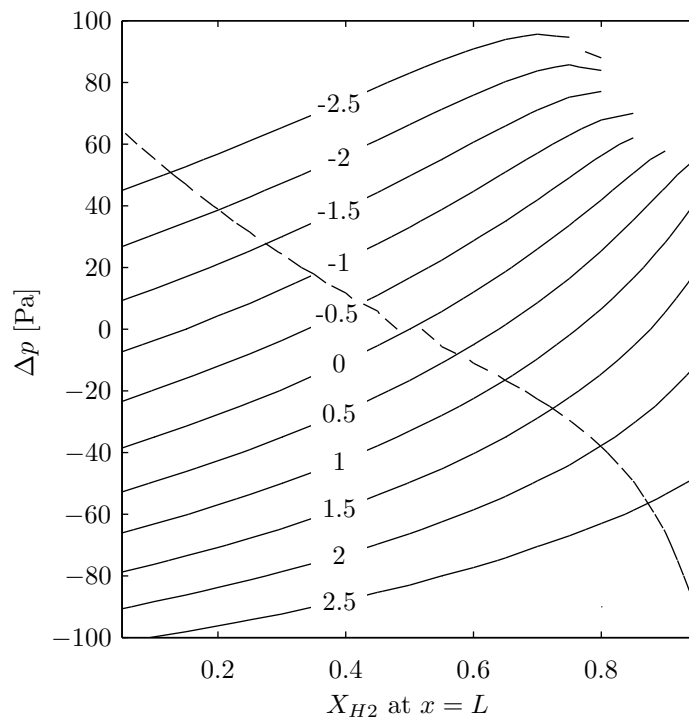


Figure 9.4: Contours of the average mass flux of water, $\overline{\rho_{H_2O} u_{x,H_2O}}$ [$\text{kg m}^{-2} \text{s}^{-1}$], at different pressure and concentration gradients. Along the dashed line the mass flux ratio is stoichiometric.

$-\sqrt{M_{H_2}/M_{H_2O}}$. If, instead, there is no concentration gradient then the species velocities are equal and the value of the mass flux ratio is $X_{H_2}M_{H_2}/X_{H_2O}M_{H_2O}$. If there is neither a species nor a concentration gradient then all velocities are zero and the species mass flux ratio is undefined. Aside from these simple cases the lines of constant species mass flux ratio form a radial pattern. When the hydrogen velocity is zero, as the convective and diffusive fluxes cancel, the species mass flux ratio is zero and likewise when the water velocity is zero the species mass flux ratio is infinite. Figure 9.3 and 9.4 show the mass

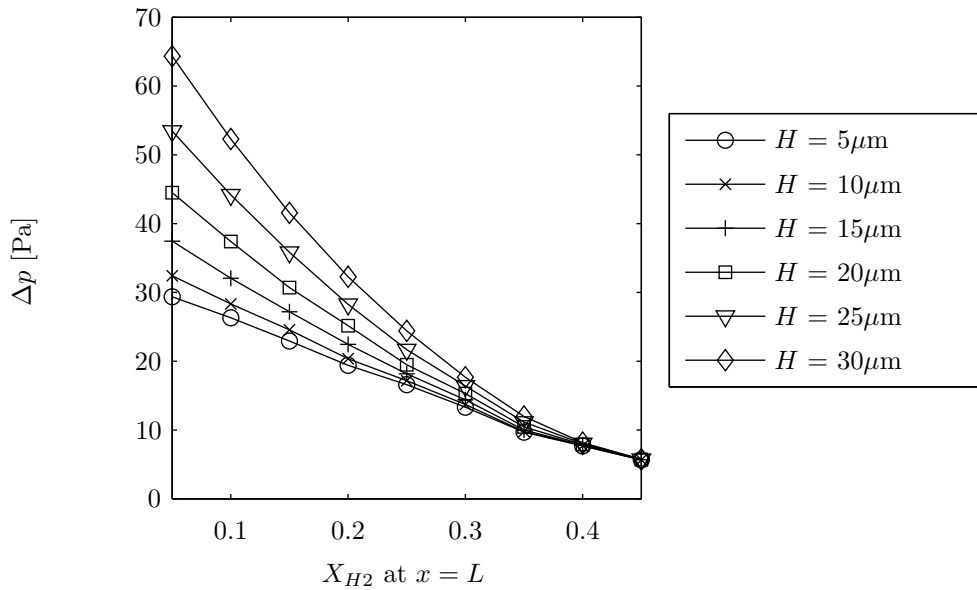


Figure 9.5: Pressure difference against X_{H_2} at the outlet for different channel widths. The results shown correspond to the mass flux ratio being stoichiometric. The pressure drop corresponding to a specific value of X_{H_2} depends on the channel width.

flux of hydrogen and water corresponding to Figure 9.2. For a positive flux of hydrogen it is not sufficient to ensure the concentration gradient is negative, one must also consider the pressure gradient. Likewise for a large enough total pressure drop it is possible for the mass flux of hydrogen to be positive despite the concentration gradient also being positive. However, if the species mass flux ratio is stoichiometric, a negative concentration gradient is required for a positive hydrogen mass flux.

Figure 9.5 shows the relationship between total pressure change and X_{H_2} at $x = L$ for

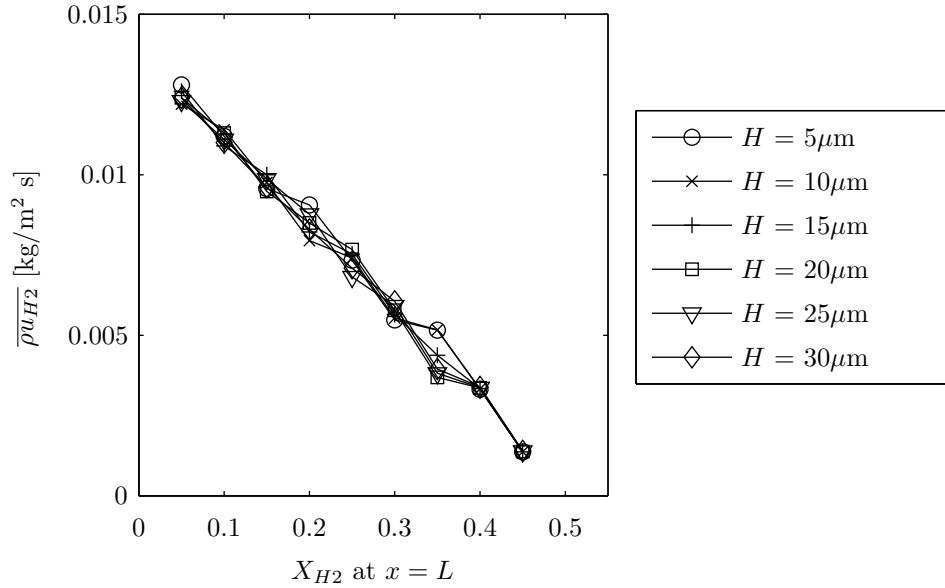


Figure 9.6: Average hydrogen mass flux against X_{H_2} at the outlet for different channel widths. The results shown correspond to the mass flux ratio being stoichiometric.

different channel widths, when the species mass flux ratio is stoichiometric. The length of the channel is constant at $5 \mu\text{m}$. Figure 9.6 shows the average mass flux of hydrogen which is nearly independent of channel width. If the hydrogen mole fractions at each end of the channel are maintained constant, increasing the channel width increases the pressure drop along the channel but does not affect the average mass flux through the channel. This is because the hydrogen is driven by diffusive rather than viscous forces.

If the mole fraction of hydrogen at $x = 0$ is 0.25, instead of 0.5, the species mass flux ratio for different pressure and concentration gradients are as shown in Figure 9.7. The features discussed previously are still observable, with the flux ratio at zero concentration gradient still being $X_{H_2}M_{H_2}/X_{H_2O}M_{H_2O}$.

Finally, a similar plot is obtained for the original problem ($X_{H_2} = 0.5$ at $x = 0$) with zero mixture slip at the walls. Figure 9.8 shows the results obtained. Note that for zero pressure drop the average mass flux ratio is now -1. For zero concentration gradient the flux ratio is the same as that obtained with the diffusive slip boundary condition as seen in Figure 9.2. Comparison between these two figures illustrates the importance of diffusion

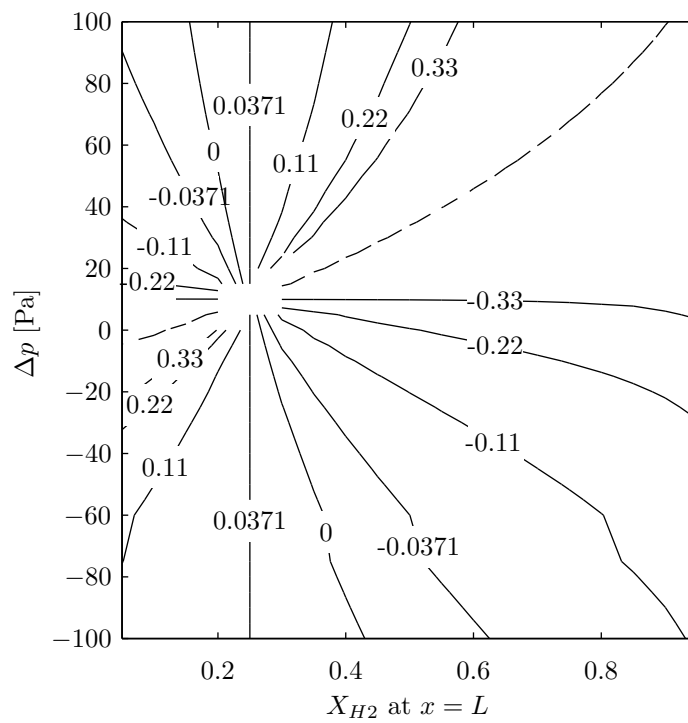


Figure 9.7: Contours of the species mass flux ratio for small values of Δp , similar to Figure 9.2, except that the mole fraction of hydrogen at $x = 0$ is 0.25. The dashed line represents an infinite flux ratio.

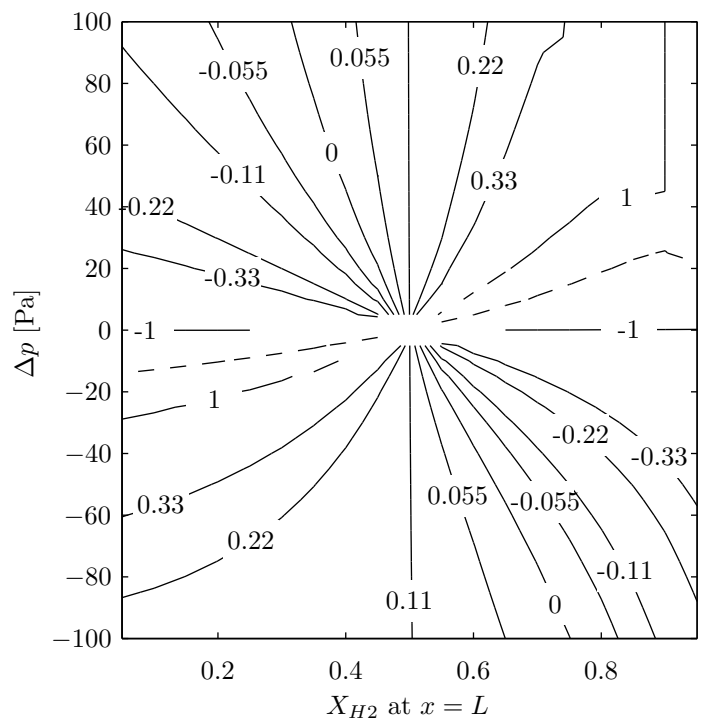


Figure 9.8: Contours of the species mass flux ratio for small values of Δp , similar to Figure 9.2, except that the wall boundary condition is zero mixture velocity. The dashed line represents an infinite flux ratio.

slip for problems dominated by diffusion. Conversely, for small concentration gradients the inclusion of diffusion slip at the walls has very little effect on the species mass flux ratio.

9.2 Binary flow with one inert component

9.2.1 The Stefan tube problem

The Stefan tube is a well known problem in the theory of gas diffusion. A tube is exposed to air at one end, and water (as a liquid) at the other end. The water evaporates from the liquid surface and diffuses through the tube into the air, while other gases in the air, mostly nitrogen, cannot pass through the end of the tube blocked by the water. It is common to reduce this to a binary problem, treating air as an inert ideal gas or sometimes as pure nitrogen. This helps to reduce the complexity of the analysis.

The Stefan tube is traditionally treated as a one-dimensional problem, see, for example, Eckert and Drake (1959) and Bird et al. (1960) who built their analysis on the 1874 paper by Stefan. The analysis hinges upon the assumption that the inert gas is stationary everywhere, because the average mass flow rate is zero. After this assumption is made, the analysis is straightforward and the result is that the mass flow rate of the water vapour, labelled A, is given by,

$$\rho_A u_A = - \frac{D_{AB}}{(RT)_A} \frac{p}{p - p_A} \frac{dp_A}{dx} \quad (9.2)$$

where x is the direction in which the diffusion is taking place. Equation (9.2) is known as Stefan's Law. The species partial pressures do not vary with y , subsequently the velocity of gas A is a function of x only, and the solution is one-dimensional. In fact, this approach is unsatisfactory because of the velocities it predicts at the wall, which agree with neither the zero mixture slip approximation nor the diffusion slip theory (nor even a zero species slip condition). Using the no-slip wall condition a two-dimensional solution, with circulation of the inert gas, was predicted by Meyer and Kostin (1975).

Salcedo-Diaz et al. (2008) used a model that includes diffusion slip to solve the Stefan tube problem. They found that the velocity of the inert gas was not zero, but at the wall it

flowed towards the end saturated with water, and in mid-channel it flowed in the opposite direction. On average the mass flux of the inert gas was zero, as required by the principle of conservation of mass. The flux of water vapour was close to that predicted by Equation (9.2), for a wide channel, but for a narrow channel it was not. This was also predicted by Whitaker (1991). Interestingly, it appears from the results of Salcedo-Diaz that in a narrow channel the flux of the diffusing gas is almost independent of the mole fraction at the bottom of the tube. However, the Salcedo-Diaz model includes non-continuum effects, and it is likely that this result is due to these. The lack of agreement with the continuum based Stefan's Law is then hardly surprising.

The calculations in the subsequent section are not of the Stefan tube problem, but a similar type of problem; binary flow through a channel with a reacting surface at one end. The two gases will be labelled the inert and reacting gas, and will be water vapour and hydrogen respectively. Therefore the water vapour is no longer the diffusing gas, and now becomes the inert gas.

9.2.2 A LB model of a Stefan tube type problem

Instead of studying the classical Stefan tube problem, in this section a LB model of a similar problem is investigated. This problem may be thought of as diffusion in a solid oxide fuel cell with particularly low chemical activity, such that the products of the reaction may be ignored. Two components, hydrogen and water vapour, are present in a channel closed at one end by a reacting surface. The water vapour does not react at this surface (at $x = L$), while the hydrogen is absorbed at a specific rate. At the other end of the channel the gas has a known composition and total pressure.

To model this problem, the boundary conditions described in Section 8.1.3 are used. At the boundary where $x = 0$ the conditions of 1 bar total pressure and $X_{H_2} = 0.5$ are set. A summary of this and the other boundary conditions is shown in Figure 9.9.

Unfortunately, the results obtained are not perfect. To illustrate this, an example calculation was performed with the mass flux of hydrogen at $x = L$ set to $0.1 \text{ kg m}^{-2} \text{ s}^{-1}$.

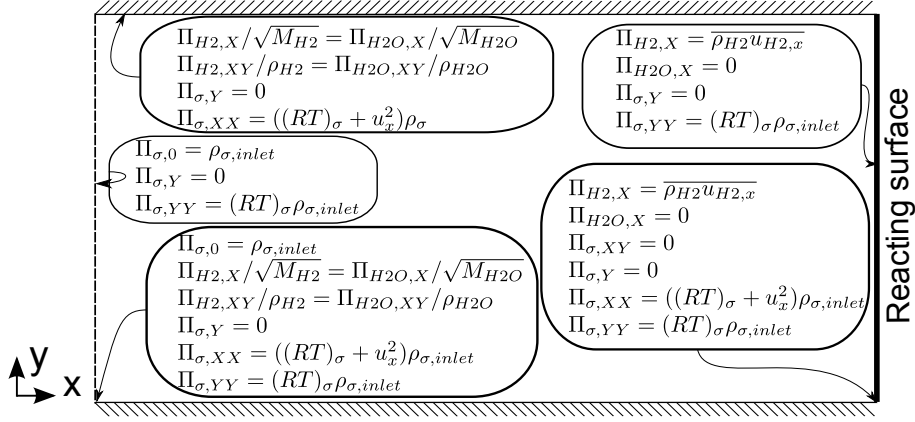


Figure 9.9: The boundary conditions at the wall, the open boundary, the reacting surface and the intersections between them for the Stefan tube type problem of Section 9.2.2.

The tube is 20 μm long and 10 μm wide and a 60×30 grid was used. Figures 9.10 and 9.11 show the x and y velocities of the species and the mixture. Figure 9.10 shows that the hydrogen has a positive x velocity throughout the domain, which is larger along the centreline than at the walls. The water vapour has a negative x velocity along the wall and a positive x velocity near the centre of the channel. The mixture x velocity has a similar pattern to that of the water, but the total mass flux in the x direction of the mixture is not zero. In Figure 9.11 the y velocities of the species and mixture show that significant circulation is taking place near the reacting surface at $x = 60$.

Figure 9.12 shows the total pressure of the mixture. Clearly, the corner nodes at the intersection between the reacting surface and the wall have unrealistic total pressures. This is because of the discontinuity between the mixture velocity along the wall, the diffusion slip velocity, and the set mass flux imposed at the corners. Therefore, $\partial u_x / \partial x$ is not zero. The boundary conditions include the condition that $\Pi_{XX} = \Pi_{XX}^{eq}$, equivalently $\Pi_{XX}^{neq} = 0$ and $\partial u_x / \partial x = 0$. There is thus an inconsistency between the boundary conditions, not an error with the implementation.

The error in the total pressure has a limited impact away from the affected corners. Figure 9.13 shows the cross-channel-averaged total pressure along the channel. The effect of the misbehaving corner nodes can be seen but only in the last ten grid points. Figure

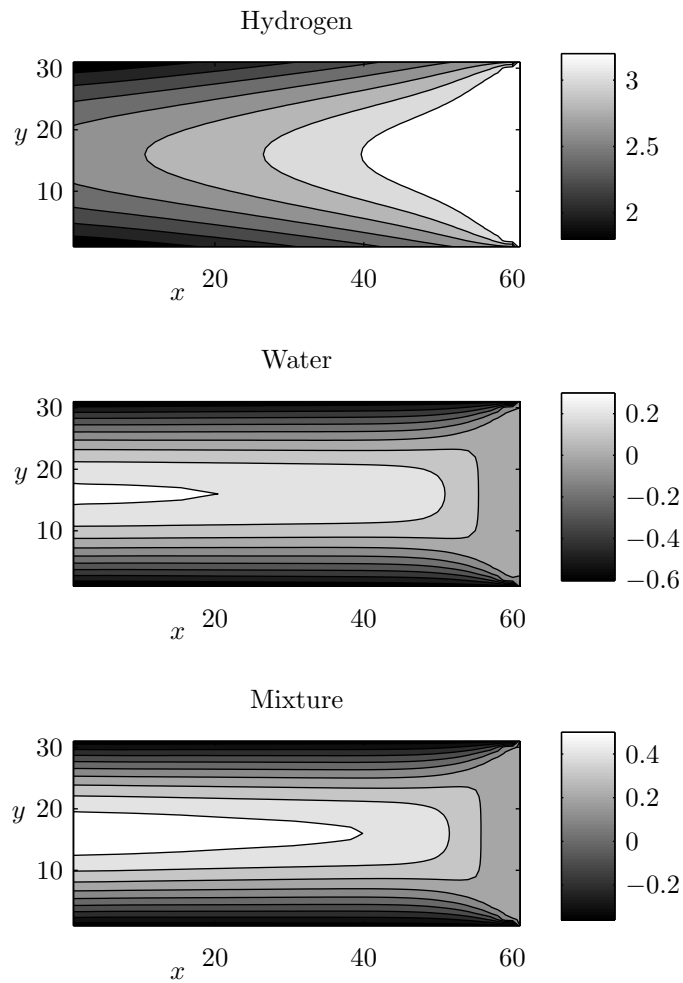


Figure 9.10: Contours of the x component of the species and mixture velocities [m/s] for the Stefan tube type problem. The x velocity of the water is zero at $x = 60$.

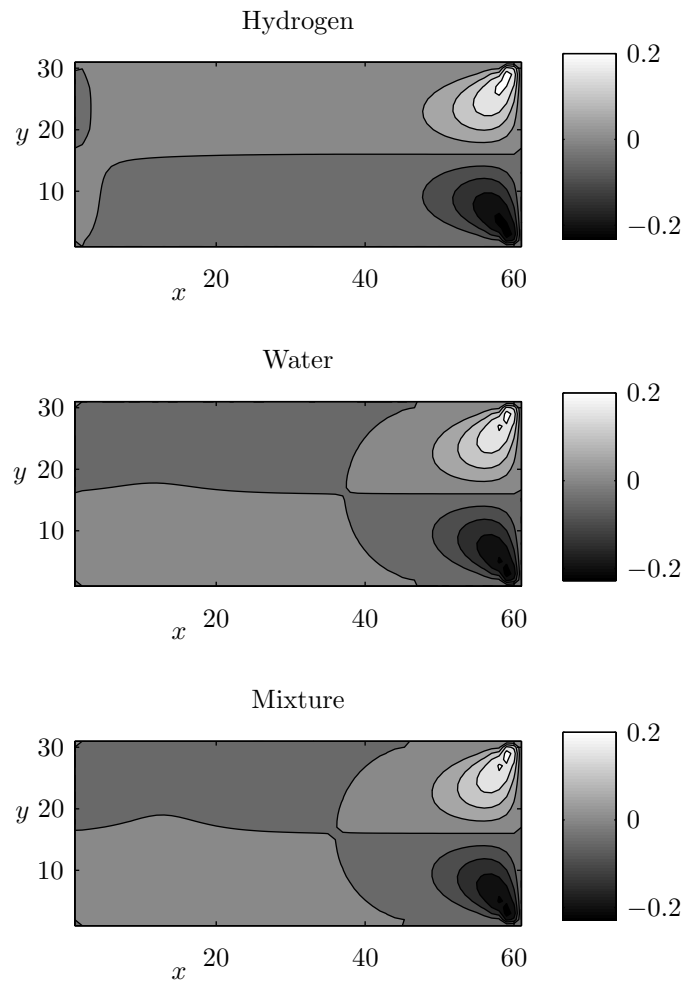


Figure 9.11: Contours of the y component of the species and mixture velocities [m/s] for the Stefan tube type problem. The y velocity of both species is zero at all the boundaries.

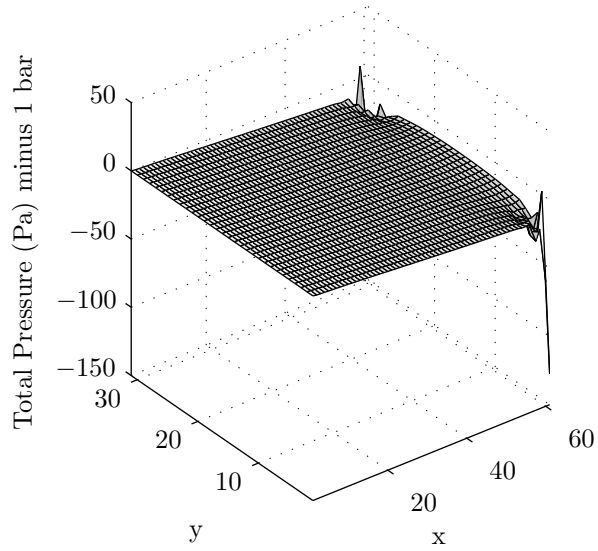


Figure 9.12: Total pressure minus 1 bar, showing the unrealistic effect at the corners. The reacting surface is located at $x = 60$.

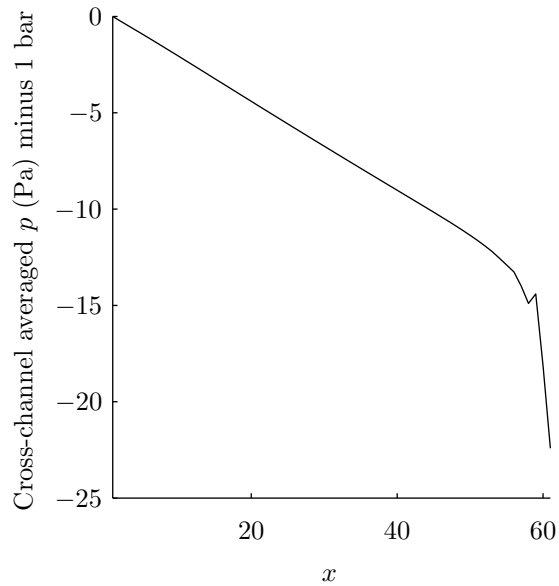


Figure 9.13: Cross-channel-averaged total pressure minus 1 bar at different distances along the channel. The disturbance in the pressure field caused by the corners is only evident near the reacting surface.

9.14 shows the mole fractions of the two gases along the centreline of the channel, and no obvious influence of the corner nodes can be observed.

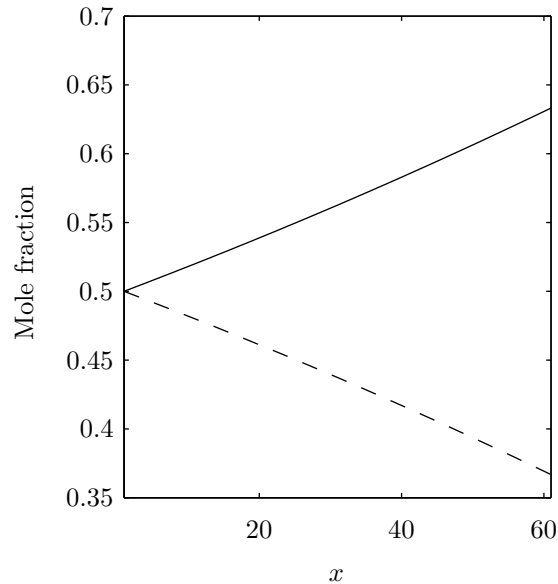


Figure 9.14: Mole fraction of hydrogen (dashed line) and water vapour (solid line) recorded along the centreline of the channel.

9.2.3 The effect of channel width

In this section, some results are presented for the problem described in Section 9.2.2 at different channel widths and lengths. To alleviate the strange behaviour of the total pressure at the corners where $x = L$, the pressures at $x = L$ were linearly extrapolated from the other half of the domain.

Figure 9.15 shows the relationship between the hydrogen pressure difference along the channel and the average hydrogen mass flux for a channel $10 \mu\text{m}$ long and of varying widths. Also plotted is the Stefan's Law result, from Equation (9.2), which is independent of channel width. Figure 9.16 shows the change in hydrogen mole fraction along the channel. Figures 9.17 and 9.18 show similar graphs for a channel $20 \mu\text{m}$ long. Clearly, the one-dimensional approximation of Stefan's Law does not lead to a realistic solution.

These results may be explained by considering the domain as two regions; the region

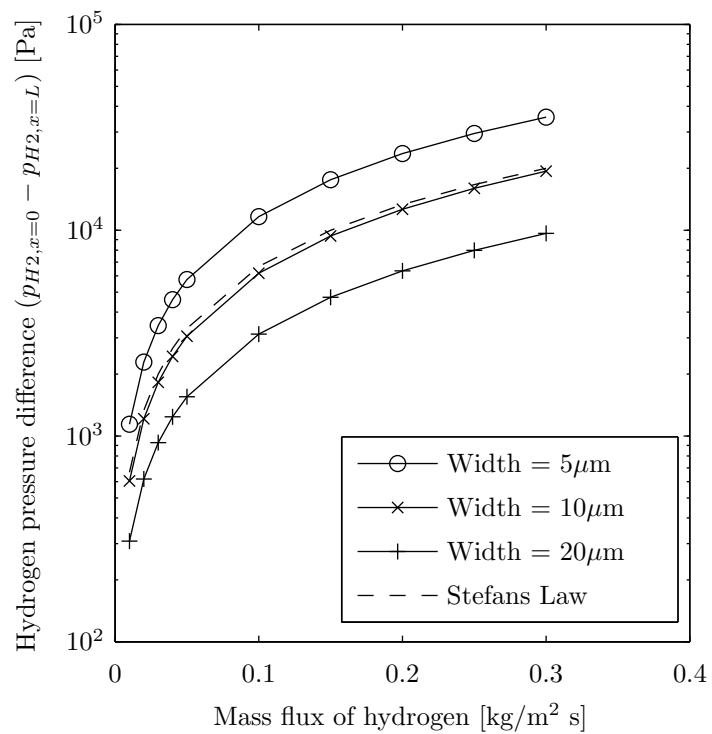


Figure 9.15: The change in hydrogen pressure drop along the channel for the Stefan tube type problem plotted against the average mass flux of hydrogen for different channel widths. Also plotted is the Stefan's Law one-dimensional solution.

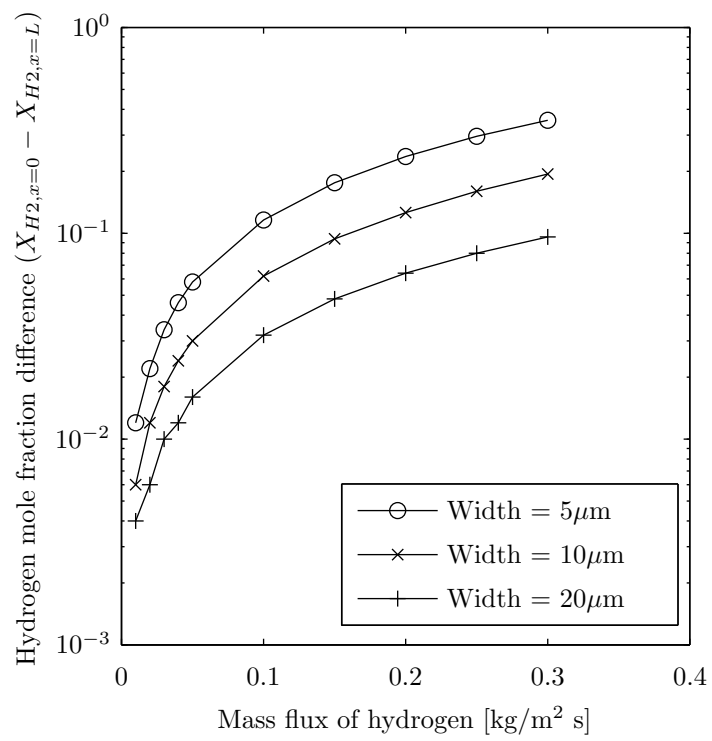


Figure 9.16: The change in hydrogen mole fraction along the Stefan tube problem plotted against the average mass flux of hydrogen at different channel widths.

close to the wall and the region in the middle of the channel. Close to the wall the effect of diffusion slip dominates so that, changes in the width of the channel have only a small effect on the hydrogen mole fraction gradient and the diffusion slip velocity (through Equation (7.40)). The mixture velocity is negative and acts to reduce the average mass flux of hydrogen. In the region near the centre of the channel the total pressure gradient dominates, causing the mixture velocity to be positive and the average mass flux of hydrogen to increase. Increasing the width of the channel increases the width of the central region, and to maintain the same average hydrogen mass flux the total pressure gradient must be reduced.

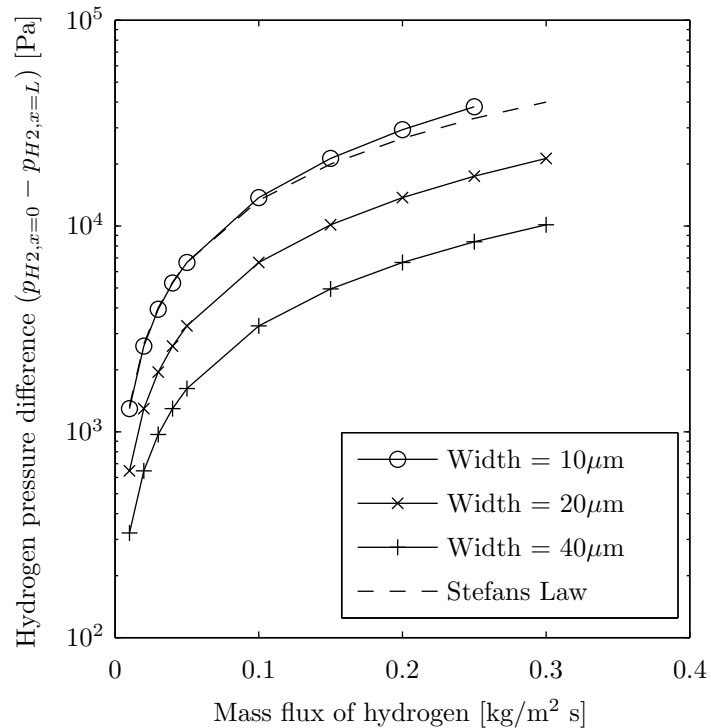


Figure 9.17: As Figure 9.15 but the channel length is $20\mu m$

9.3 Conclusions

The results of the two problems in this chapter are very relevant in the context of solid oxide fuel cells, although, on their own, they do not constitute a thorough examination of

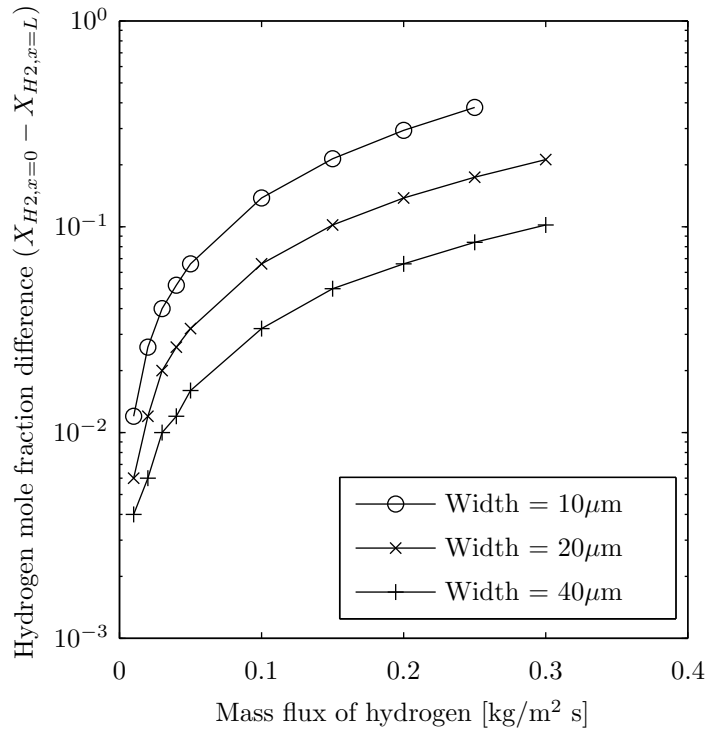


Figure 9.18: As Figure 9.16 but the channel length is $20\mu m$

the topic. The errors identified with the solution of the Stefan tube problem were related to the formulation of the problem, rather than the Lattice Boltzmann scheme. Further work is needed to identify exactly how a reacting surface behaves when intersected by a solid boundary, using continuum kinetic theory.

The fully-developed flow problem is applicable to a fuel cell with only products and reactants present, in which case the ratio of the species mass flux must take the stoichiometric value. This constraint is sufficient to ensure that the total pressure gradient is small, and the mass flux of hydrogen is driven by the concentration gradient and is independent of channel width.

The Stefan tube type problem represents a fuel cell with products and an inert (heavy) species present, while the reactants have been ignored. This problem turned out to be two-dimensional in nature, with recirculation of the inert gas. If the fuel cell maintains a constant hydrogen concentration at the reacting surface, then a wider channel will pass a higher hydrogen mass flux per unit area.

Chapter 10

Conclusions

This chapter presents a summary of the work contained in this thesis along with suggestions for future research. Overall, the work should be considered as proof of the viability of using LB methods for multi-component gases, although it does not yet constitute a comprehensive tool. Future work should follow the spirit of the current work in seeking a fundamental approach to the solution of problems using the Lattice Boltzmann method.

10.1 Summary of results from this work

A key theme of this work has been the two viewpoints from which LB can be approached, namely the ‘particle’ basis and the ‘moment’ basis. Exactly the same method can be described from these entirely different starting points, and this makes the LB literature needlessly complicated. This thesis hopefully adds to the growing number of voices which claim that using the moment basis is the most effective way to view the LB method.

The single-component one-dimensional scheme in Chapter 2 demonstrated the importance of having unique second order moments in order to recover the correct momentum equation. The D2Q9 scheme has this property but not all the third order moments are unique, and the D2Q9 scheme can be thought of as representing the truncated nine moment system as shown in Table 4.1. Upon further inspection, the second order moments are only

truly unique when a non-physical equation of state is used. Otherwise, a physical equation of state connects the density to the pressure, and hence the zero to the second order moments. It is this link which destabilises the scheme, as demonstrated by the expression for the momentum flux density tensor, Equation (4.44). A single-component model for the steady-state compressible Navier-Stokes equations was developed in Chapter 4 which has a physical equation of state.

Boundary conditions are commonly conceived and described in the particle basis, while specifying some conditions in the moment basis and others in the particle basis leads to a hybrid which is unsatisfactory. A new method of analysis, based entirely in the moment basis, was introduced in Chapter 5. The key result is that, although three moments must be given values at a straight boundary, the choice of which three moments to use is restricted. This analysis may be used to explore existing schemes, such as the ‘bounce-back’ scheme which introduces an unspecified slip velocity at the boundary.

The results for Poiseuille flow in Chapter 6, showed good agreement with the analytical solution. However, the use of a physical equation of state increases computational time by placing a lower limit on the size of the time step. The stability range for the bulk and shear viscosities is such that they must have comparable values. Finally, it was observed that the maximum physical grid spacing is small, for example for hydrogen it is around $3 \times 10^{-7}\text{m}$.

The best multi-component model examined in Chapter 7 was the Mixture Centred Equilibrium (MCE), where all the moments of the equilibrium function are centred on the mixture velocity. This provided the greatest range of stability compared with the other equilibrium functions described. The species momentum flux density tensor is a function of both the species and mixture velocities, but the momentum flux density tensor for the mixture is the same as that of a single component gas. The steady-state compressible Navier-Stokes equations are recovered for the mixture, with a viscosity defined for the mixture but not for the species. The diffusive behaviour is a result of the first order moments of the collision integral and can be controlled separately from the viscous behaviour. The Stefan-Maxwell diffusion equations are recovered, plus ‘pressure diffusion’ terms, however

pressure diffusion was small in all cases considered. Diffusive slip boundary conditions were devised using the moment based method for boundary conditions, and validated against a one-dimensional numerical solution of the traditional fluid dynamic equations.

For real applications the use of the variable transformation scheme of Chapter 8 is essential for reducing computational time and, in the example considered, did so by a factor of approximately fifty. This involved no changes to the model of Chapter 7, but required significant changes to the implementation. For equilibrium functions other than the MCE, the variable transformation would become even more complicated. Pre-conditioning shows promise for further reducing the computational time by changing the time derivative terms of the momentum equation. Further work is needed to optimise the pre-conditioning process.

Finally, in Chapter 9 the LB model was applied to two different diffusion problems, demonstrating the versatility of the model. The LB solution identified inconsistencies with the formulation of the Stefan tube type problem, and further work is needed in this area. The results are relevant to fuel cell design but are far from extensive. For binary channel flow, diffusion slip boundary conditions must be taken into account when the total pressure gradient is small.

10.2 Suggestions for future research

The principle obstacle, which must be overcome before LB methods are considered to be useful for multi-component gas modelling, is the limited grid size. It is with the greatest regret that the author must concede that the current work has barely scratched the surface of uncovering the causes of this limitation. Having a physically correct equation of state introduced the limitation on grid size. Therefore, one must assume that the instability is caused by the erroneous terms in the momentum flux density tensor which lead to changes in the effective bulk viscosity. This is not the only possible explanation; Dellar (2002b) identified an instability mode which was not visible in a long-wavelength analysis. The instability with large grid spacing could be similarly invisible. However, concluding that the instability is most likely caused by the bulk viscosity highlights the next failure of the

model, the inability to set the bulk viscosity to zero. For most engineering applications, the bulk viscosity does not play a role (see Stewartson (1964)), and the ability to remove bulk viscosity terms is desirable. The intention of the MRT collision operator used in this work was to separate bulk and shear viscosity terms. However, the model was not stable for values of bulk viscosity substantially different from those which correspond to a diagonal matrix Λ . A better method of controlling bulk viscosity is therefore needed.

Perhaps the simplest solution would be to make the third order moments independent, either by changing the structure of the D2Q9 model or by increasing the number of velocities. Many alternative velocity sets exist, but it is not clear which is preferable and additional velocities do increase computational requirements. It seems that nine velocities could be sufficient if they are different from the usual D2Q9 configuration. For example, if the ‘straight’ (f_1, f_2, f_3 and f_4) velocities have a magnitude of 2 while the ‘diagonal’ (f_5, f_6, f_7 and f_8) velocities remain the same, then $\tilde{\Pi}_X$ is no longer equal to $\tilde{\Pi}_{XXX}$ but instead $\tilde{\Pi}_{XXX} = 4\tilde{\Pi}_X - 3\tilde{\Pi}_{XYX}$. If an appropriate velocity set is found that has velocities which do not stream to the nearest neighbour, boundary conditions must be applied to nodes that are not directly on the boundary. Using the moment based method for boundary conditions sensible conditions for the additional nodes may be devised.

If a new velocity set cannot be utilised, it may be possible to modify the existing D2Q9 scheme to remove the erroneous bulk viscosity terms using a finite difference scheme, such as those proposed by Toelke (2006) and Prasianakis and Karlin (2008). The aim is to use a finite difference approximation to the velocity gradients to calculate the bulk viscosity terms and then to subtract them from the momentum flux density tensor during the collision step. This author’s attempts to reproduce this work have not succeeded, but it is a promising, if somewhat cumbersome, idea. However, this seems to be addressing the symptoms of the problem not the cause.

If, by whatever means, a scheme were developed which was stable at larger grid spacings, this would allow a re-examination of the multi-component scheme. The idea behind the MCE, SCE and CSCE equilibrium functions was that the mixture or species velocity would appear in the viscous terms. However, the expressions for the viscous stress tensor using

any of the equilibrium functions contained both mixture and species velocities, and all were unsatisfactory. Furthermore, it is not clear that the method used to derive the expressions for the species momentum flux density tensors was entirely appropriate. These are minor points however, as the correct macroscopic equation for the mixture was recovered for the MCE and CSCE.

Extending the model developed in this thesis to gases with more than two components is feasible. Once again, the mixture Navier-Stokes equations could be used along with the Stefan-Maxwell equation for the diffusion. All that is required is an extension to the collision terms.

Aside from the development of the model, this thesis has highlighted the fact that there is much that is not understood about gas mixtures. Chapter 9 was far from a comprehensive review of gas mixtures. Fuel cells rarely have only two gas species present and further inert species can influence the behaviour of the reacting species, as seen in the Stefan tube problem. The behaviour of a gas mixture immediately adjacent to a reacting surface has not been extensively studied, as was seen with the boundary conditions for the Stefan tube type problem. Within a mean free path distance from the surface, the gases do not behave as a continuum. Examining this layer would result in macroscopic conditions that could be applied to the LB model, in a similar manner as the macroscopic conditions for diffusion slip.

In summary, for those wishing to follow this work there is much for mathematicians, physicists and engineers to do.

References

- Ahrenholz, B., Toelke, J., and Krafczyk, M. (2006). Lattice-Boltzmann simulations in reconstructed parametrized porous media. *Int. J. Comput. Fluid Dyn.*, 20(6):369–377.
- Andries, P., Aoki, K., and Perthame, B. (2002). A consistent BGK-type model for gas mixtures. *J. Statist. Phys.*, 106(5-6):993–1018.
- Arcidiacono, S., Ansumali, S., Karlin, I. V., Mantzaras, J., and Boulouchos, K. B. (2006a). Entropic lattice Boltzmann method for simulation of binary mixtures. *Math. Comput. Simulat.*, 72(2-6):79–83.
- Arcidiacono, S., Karlin, I. V., Mantzaras, J., and Frouzakis, C. E. (2007). Lattice Boltzmann model for the simulation of multicomponent mixtures. *Phys. Rev. E*, 76(4, Part 2):046703.
- Arcidiacono, S., Mantzaras, J., Ansumali, S., Karlin, I. V., Frouzakis, C., and Boulouchos, K. B. (2006b). Simulation of binary mixtures with the lattice Boltzmann method. *Phys. Rev. E*, 74(5):056707.
- Asinari, P. (2005). Viscous coupling based lattice Boltzmann model for binary mixtures. *Phys. Fluids*, 17(6):067102.
- Asinari, P. (2006). Semi-implicit-linearized multiple-relaxation-time formulation of lattice Boltzmann schemes for mixture modeling. *Phys. Rev. E*, 73(5, Part 2):056705.
- Asinari, P. (2008). Multiple-relaxation-time lattice Boltzmann scheme for homogeneous mixture flows with external force. *Phys. Rev. E*, 77(5, Part 2):056706.

- Asinari, P. (2009). Lattice Boltzmann scheme for mixture modeling: Analysis of the continuum diffusion regimes recovering Maxwell-Stefan model and incompressible Navier-Stokes equations. *Phys. Rev. E*, 80(5, Part 2):056701.
- Asinari, P. and Ohwada, T. (2009). Connection between kinetic methods for fluid-dynamic equations and macroscopic finite-difference schemes. *Comput. Math. Appl.*, 58(5):841–861.
- Asinari, P., Quaglia, M. C., von Spakovsky, M. R., and Kasula, B. V. (2007). Direct numerical calculation of the kinematic tortuosity of reactive mixture flow in the anode layer of solid oxide fuel cells by the lattice Boltzmann method. *J. Power Sources*, 170(2):359–375.
- Baehr, H. D. and Stephan, K. (1998). *Heat and Mass-transfer*. Springer.
- Bennett, C. O. and Myers, J. E. (1982). *Momentum, Heat and Mass Transfer*. McGraw Hill Chemical Engineering Series.
- Bhatnagar, P., Gross, E., and Krook, M. (1954). A model for collision processes in gases 1: Small amplitude processes in charged and neutral one-component systems. *Phys. Rev.*, 94(3):511–525.
- Bird, III, R. B., Stewart, W. E., and Lightfoot, E. N. (1960). *Transport Phenomena*. John Wiley & Sons.
- Brush, S. G. (1976). *The Kind of Motion We Call Heat*, volume 2. North Holland.
- Cengel, Y. A. (1998). *Introduction To Thermodynamics and Heat Transfer*. McGraw-Hill Higher Education.
- Chapman, S. and Cowling, T. G. (1970). *The Mathematical Theory of Non-Uniform Gases*. Cambridge University Press.
- Chen, H. D., Chen, S. Y., and Matthaeus, W. H. (1992). Recovery of the Navier-Stokes equations using a lattice-gas Boltzmann method. *Phys. Rev. A*, 45(8):5339–5342.

- Chen, S. and Doolen, G. D. (1998). Lattice Boltzmann method for fluid flows. *Annu. Rev. Fluid Mech.*, 30:329–364.
- Chen, S. Y., Martinez, D., and Mei, R. W. (1999). On boundary conditions in lattice Boltzmann methods. *Phys. Fluids*, 8(9):2527–2536.
- Dellar, P. (2002a). Nonhydrodynamic modes and a priori construction of shallow water lattice Boltzmann equations. *Phys. Rev. E*, 65(3, Part 2B).
- Dellar, P. J. (2001). Bulk and shear viscosities in lattice Boltzmann equations. *Phys. Rev. E*, 64(3, Part 1):031203.
- Dellar, P. J. (2002b). Nonhydrodynamic modes and a priori construction of shallow water lattice Boltzmann equations. *Phys. Rev. E*, 65(3, Part 2B):036309.
- Dellar, P. J. (2003). Incompressible limits of lattice Boltzmann equations using multiple relaxation times. *J. Comput. Phys.*, 190(2):351–370.
- d’Humières, D. (1992). Generalized lattice-Boltzmann equations. In Shizgal, B. D. and Weaver, D. P., editors, *Rarefied Gas Dynamics: Theory and Simulations*, volume 159 of *Prog. Astronaut. Aeronaut.*, pages 450–458, Washington, D.C. AIAA.
- Dullien, F. A. L. and Scott, D. S. (1962). The flux-ratio for binary counterdiffusion of Ideal Gases. *Chem. Eng. Sci.*, 17(10):771–775.
- Eckert, E. R. G. and Drake, Jr, R. M. (1959). *Heat and Mass Transfer*. McGraw-Hill Book Company.
- Evans, III, R. B., Truitt, J., and Watson, G. M. (1961a). Interdiffusion of helium and argon in a large-pore graphite. *J. Chem. Eng. Data*, 6(4):522–525.
- Evans, III, R. B., Watson, G., and Mason, E. (1962a). Gaseous diffusion in porous media .2. effect of pressure gradients. *J. Chem. Phys.*, 36(7):1894–1902.

- Evans, III, R. B., Watson, G. M., and Mason, E. A. (1961b). Gaseous diffusion in porous media at uniform pressure. *J. Chem. Phys.*, 35(6):2076–2083.
- Evans, III, R. B., Watson, G. M., and Truitt, J. (1962b). Interdiffusion of gases in a low permeability graphite at uniform pressure. *J. Appl. Phys.*, 33(9):2682–2688.
- Evans, III, R. B., Watson, G. M., and Truitt, J. (1963). Interdiffusion of gases in a low-permeability graphite .2. influence of pressure gradients. *J. Appl. Phys.*, 34(7):2020–2026.
- Facin, P. C., Philippi, P. C., and dos Santos, L. O. E. (2004). A non-linear lattice-Boltzmann model for ideal miscible fluids. *Future Gener. Comp. Sy.*, 20(6):945–949.
- Geankoplis, C. J. (1993). *Transport Processes and Unit Operations*. PennWell Books.
- Ginzburg, I. and Adler, P. M. (1994). Boundary flow condition analysis for the 3-Dimensional lattice Boltzmann model. *J. Phys. II*, 4(2):191–214.
- Ginzburg, I. and d’Humières, D. (2003). Multireflection boundary conditions for lattice Boltzmann models. *Phys. Rev. E*, 68(6, Part 2):066614.
- Ginzburg, I., Verhaeghe, F., and d’Humières, D. (2008). Study of simple hydrodynamic solutions with the two-relaxation-times lattice Boltzmann scheme. *Commun. Comput. Phys.*, 3(3):519–581.
- Grad, H. (1963). Asymptotic theory of the boltzmann equation. *Phys. Fluids*, 6(2):147–181.
- Graham, T. (1876). *Chemical and Physical Researches*. [Printed by T. and A. Constable].
- Guo, Z., Asinari, P., and Zheng, C. (2009). Lattice boltzmann equation for microscale gas flows of binary mixtures. *Phys. Rev. E*, 79(2, Part 2):026702.
- Guo, Z., Zhao, T. S., and Shi, Y. (2004). Preconditioned lattice-Boltzmann method for steady flows. *Phys. Rev. E*, 70(6):066706.
- Guo, Z. L. and Zhao, T. S. (2003). Discrete velocity and lattice Boltzmann models for binary mixtures of nonideal fluids. *Phys. Rev. E*, 68(3, Part 2):035302.

- Hamel, B. B. (1966). Two-fluid hydrodynamic equations for a neutral disparate-mass binary mixture. *Phys. Fluids*, 9(1):12–22.
- He, X., Chen, S., and Doolen, G. D. (1998). A novel thermal model of the lattice Boltzmann method in incompressible limit. *J. Comput. Phys.*, 146:282–300.
- He, X. Y. and Luo, L. S. (1997a). Lattice Boltzmann model for the incompressible Navier-Stokes equation. *J. Statist. Phys.*, 88(3-4):927–944.
- He, X. Y. and Luo, L. S. (1997b). A priori derivation of the lattice Boltzmann equation. *Phys. Rev. E*, 55(6, Part A):6333–6336.
- He, X. Y. and Luo, L. S. (1997c). Theory of the lattice Boltzmann method: From the Boltzmann equation to the lattice Boltzmann equation. *Phys. Rev. E*, 56(6):6811–6817.
- He, X. Y., Zou, Q. S., Luo, L. S., and Dembo, M. (1997). Analytic solutions of simple flows and analysis of nonslip boundary conditions for the lattice Boltzmann BGK model. *J. Statist. Phys.*, 87(1-2):115–136.
- Higuera, F. J., Succi, S., and Benzi, R. (1989). Lattice gas-dynamics with enhanced collisions. *Europhys. Lett.*, 9(4):345–349.
- Hollis, A. P., Halliday, I., and Care, C. M. (2008). An accurate and versatile lattice closure scheme for lattice Boltzmann equation fluids under external forces. *J. Comput. Phys.*, 227(17):8065–8082.
- Holman, J. P. (1988). *Heat Transfer*. McGraw Hill Higher Education.
- Hoogschagen, J. (1955). Diffusion in porous catalysts and adsorbents. *Ind. Eng. Chem.*, 47(5):906–913.
- Ikenberry, E. and Truesdell, C. (1956). On the pressures and the flux of energy in a gas according to Maxwell’s kinetic theory, I. *J. Ratl. Mech. Anal.*, 5:1–54.

- Inamuro, T., Yoshino, M., and Ogino, F. (1995). Non-slip boundary-condition for lattice Boltzmann simulations. *Phys. Fluids*, 7(12):2928–2930.
- Incropera, F. P., DeWitt, D. P., Bergman, T. L., and Lavine, A. S. (2001). *Fundamentals of Heat and Mass Transfer*. John Wiley & Sons.
- Ivchenko, I. N., Loyalka, S. K., and Tompson, R. V. (2002). Boundary slip phenomena in a binary gas mixture. *Z. Angew. Math. Phys.*, 53(1):58–72.
- Izquierdo, S. and Fueyo, N. (2009). Optimal preconditioning of lattice Boltzmann methods. *J. Comput. Phys.*, 228(17):6479–6495.
- Jackson, R. (1977). *Transport in Porous Catalysts (Chemical engineering monographs)*. Elsevier Science Ltd.
- Joshi, A. S., Grew, K. N., Peracchio, A. A., and Chiu, W. K. S. (2007a). Lattice Boltzmann modeling of 2D gas transport in a solid oxide fuel cell anode. *J. Power Sources*, 164(2):631–638.
- Joshi, A. S., Peracchio, A. A., Grew, K. N., and Chiu, W. K. S. (2007b). Lattice Boltzmann method for multi-component, non-continuum mass diffusion. *J. Phys. D: Appl. Phys.*, 40(23):7593–7600.
- Junk, M. and Yang, Z. X. (2005). One-point boundary condition for the lattice Boltzmann method. *Phys. Rev. E*, 72(6, Part 2):066701.
- Kim, S. H., Pitsch, H., and Boyd, I. D. (2009). Lattice Boltzmann modeling of multicomponent diffusion in narrow channels. *Phys. Rev. E*, 79(1, Part 2):016702.
- Knaff, G. and Schlunder, E. U. (1985). Experimental confirmation of graham law of diffusion up to pore diameters of 2 μm . *Chem. Eng. Process.*, 19(3):167–173.
- Kramers, H. A. and Kistemaker, J. (1943). On the slip of a diffusing gas mixture along a wall. *Physica*, 10:699–713.

- Lallemand, P. and Luo, L. S. (2000). Theory of the lattice Boltzmann method: Dispersion, dissipation, isotropy, Galilean invariance, and stability. *Phys. Rev. E*, 61(6, Part A):6546–6562.
- Landau, L. D. and Lifshitz, E. M. (1959). *Fluid Mechanics*. Pergamon Press.
- Latt, J. and Chopard, B. (2006). Lattice Boltzmann method with regularized pre-collision distribution functions. *Math. Comput. Simulat.*, 72(2-6):165–168.
- Latt, J., Chopard, B., Malaspinas, O., Deville, M., and Michler, A. (2008). Straight velocity boundaries in the lattice Boltzmann method. *Phys. Rev. E*, 77(5, Part 2):056703.
- Lee, J. H., Heo, J. W., Lee, D. S., Kim, J., Kim, G. H., Lee, H. W., Song, H. S., and Moon, J. H. (2003). The impact of anode microstructure on the power generating characteristics of SOFC. *Solid State Ionics*, 158(3-4):225–232.
- Lee, J. H., Moon, H., Lee, H. W., Kim, J., Kim, J. D., and Yoon, K. H. (2002). Quantitative analysis of microstructure and its related electrical property of SOFC anode, Ni-YSZ cermet. *Solid State Ionics*, 148(1-2):15–26.
- Lee, K. R., Choi, S. H., Kim, J., Lee, H. W., and Lee, J. H. (2005). Viable image analyzing method to characterize the microstructure and the properties of the Ni/YSZ cermet anode of SOFC. *J. Power Sources*, 140(2):226–234.
- Loyalka, S. K. (1971). Velocity slip coefficient and the diffusion slip velocity for a multi-component gas mixture. *The Phys. Fluids*, 14(12):2599–2604.
- Luo, L. S. (2004). Comment on “Discrete Boltzmann equation for microfluidics”. *Phys. Rev. Letters*, 92(13):139401.
- Luo, L. S. and Girimaji, S. S. (2002). Lattice Boltzmann model for binary mixtures. *Phys. Rev. E*, 66(3, Part 2A):035301.
- Maier, R. S., Bernard, R. S., and Grunau, D. W. (1996). Boundary conditions for the lattice Boltzmann method. *Phys. Fluids*, 8(7):1788–1801.

- Mason, E. A. and Evans, III, R. B. (1969). Graham's laws: Simple demonstrations of gases in motion: Part I, Theory. *J. Chem. Educ.*, 46(6):358–364.
- Mason, E. A., Love, L. D., and Evans, III, R. B. (1969). Graham's laws: Simple demonstrations of gases in motion: Part II, Experiments. *J. Chem. Educ.*, 46(7):423–427.
- McCracken, M. E. and Abraham, J. (2005). Lattice Boltzmann methods for binary mixtures with different molecular weights. *Phys. Rev. E*, 71(4, Part 2):046704.
- McNamara, G. R., Garcia, A. L., and Alder, B. J. (1995). Stabilization of thermal lattice Boltzmann models. *J. Statist. Phys.*, 81(1-2):395–408.
- Meyer, J. P. and Kostin, M. D. (1975). Circulation phenomena in stefan diffusion. *Int. J. Heat Mass Transfer*, 18(11):1293–1297.
- Mills, A. F. (2003). On steady one-dimensional diffusion in binary ideal gas mixtures. *Int. J. Heat Mass Transfer*, 46(13):2495–2497.
- Mills, A. F. (2007). Diffusion creep. *Int. J. Heat Mass Transfer*, 50(25-26):5087–5098.
- Mo, G. and Rosenberger, F. (1991). Molecular-Dynamics simulations of flow with binary diffusion in a 2-Dimensional channel with atomically rough walls. *Phys. Rev. A*, 44(8):4978–4985.
- Noble, D. R., Chen, S. Y., Georgiadis, J. G., and Buckius, R. (1995a). A consistent hydrodynamic boundary-condition for the Lattice Boltzmann method. *Phys. Fluids*, 7(1):203–209.
- Noble, D. R., Georgiadis, J. G., and Buckius, R. O. (1995b). Direct assessment of lattice Boltzmann hydrodynamics and boundary-conditions for recirculating-flows. *J. Statist. Phys.*, 81(1-2):17–33.
- Noever, D. (1990a). A note on the no-slip condition applied to diffusing gases. *Phys. Lett. A*, 144(4-5):253–255.

- Noever, D. A. (1990b). The baroeffect and an appropriate momentum boundary-condition. *Phys. Fluids A-Fluid Dynamics*, 2(5):858–865.
- Noever, D. A. (1990c). Ternary baroeffect with a nondiffusing component. *Phys. Rev. Letters*, 65(13):1587–1596.
- Poling, B. E., Prausnitz, J. M., and O’Connell, J. (2000). *The Properties of Gases and Liquids*. McGraw-Hill Professional, 5th edition.
- Prasianakis, N. I. and Karlin, I. V. (2008). Lattice Boltzmann method for simulation of compressible flows on standard lattices. *Phys. Rev. E*, 78(1, Part 2):016704.
- Rama, P., Liu, Y., Chen, R., Ostadi, H., Jiang, K., Gao, Y., Zhang, X., Fisher, R., and Jeschke, M. (2010). Multiscale modeling of single-phase multicomponent transport in the cathode gas diffusion layer of a polymer electrolyte fuel cell. *Energy Fuels*, 24:3130–3143.
- Reis, T. and Phillips, T. N. (2008). Alternative approach to the solution of the dispersion relation for a generalized lattice Boltzmann equation. *Phys. Rev. E*, 77(2, Part 2):026702.
- Remick, R. R. and Geankoplis, C. J. (1973). Binary diffusion of gases in capillaries in transition region between Knudsen and molecular diffusion. *Ind. Eng. Chem. Fundam.*, 12(12):214–220.
- Salcedo-Diaz, R., Ruiz-Femenia, R., Kerkhof, P. J. A. M., and Peters, E. A. J. F. (2008). Velocity profiles and circulation in Stefan-diffusion. *Chem. Eng. Sci.*, 63(19):4685–4693.
- Sirovich, L. (1962). Kinetic modeling of gas mixtures. *Phys. Fluids*, 5(8):908–918.
- Skordos, P. A. (1993). Initial and boundary-conditions for the lattice Boltzmann method. *Phys. Rev. E*, 48(6):4823–4842.
- Sofonea, V. and Sekerka, R. (2005a). Boundary conditions for the upwind finite difference Lattice Boltzmann model: Evidence of slip velocity in micro-channel flow. *J. Comput. Phys.*, 207(2):639–659.

- Sofonea, V. and Sekerka, R. F. (2001). BGK models for diffusion in isothermal binary fluid systems. *Physica A*, 299(3-4):494–520.
- Sofonea, V. and Sekerka, R. F. (2005b). Diffusivity of two-component isothermal finite difference lattice Boltzmann models. *Int. J. Mod. Phys. C*, 16(7):1075–1090.
- Stewartson, K. (1964). *The Theory of Laminar Boundary Layers in Compressible Fluids*. Oxford University Press, Oxford.
- Succi, S., Benzi, R., and Higuera, F. (1991). The Lattice Boltzmann-Equation - A New Tool For Computational Fluid-Dynamics. *Physica D*, 47(1-2):219–230.
- Succi, S., Karlin, I. V., and Chen, H. (2002). Role of the H theorem in lattice Boltzmann hydrodynamic simulations. *Rev. Mod. Phys.*, 74:1203–1220.
- Toelke, J. (2006). A thermal model based on the lattice Boltzmann method for low Mach number compressible flows. *J. Comput. Theor. Nanosci.*, 3(4):579–587.
- Torrilhon, M. and Struchtrup, H. (2008). Boundary conditions for regularized 13-moment-equations for micro-channel-flows. *J. Comput. Phys.*, 227(3):1982–2011.
- VanKampen, N. G. (1987). Chapman-Enskog as an application of the method for eliminating fast variables. *J. Statist. Phys.*, 46:709–727.
- Verberg, R. and Ladd, A. J. C. (1999). Simulation of low-Reynolds-number flow via a time-independent lattice-Boltzmann method. *Phys. Rev. E*, 60:3366–3373.
- Verhaeghe, F., Luo, L.-S., and Blanpain, B. (2009). Lattice Boltzmann modeling of microchannel flow in slip flow regime. *J. Comput. Phys.*, 228(1):147–157.
- Vincenti, W. G. and Kruger, C. H. (1976). *Introduction to Physical Gas Dynamics*. Krieger Publishing Company.
- Wang, L. and Afsharpoya, B. (2006). Modeling fluid flow in fuel cells using the lattice-Boltzmann approach. *Math. Comput. Simulat.*, 72(2-6):242–248.

- Welty, J., Wicks, C. E., Rorrer, G. L., and Wilson, R. E. (1984). *Fundamentals of Momentum, Heat and Mass Transfer*. John Wiley & Sons.
- Whitaker, S. (1991). Role of the species momentum equation in the analysis of the Stefan diffusion tube. *Ind. Eng. Chem. Res.*, 30(5):978–983.
- White, F. M. (1988). *Heat and Mass Transfer*. Prentice Hall.
- Young, J. B. and Todd, B. (2005). Modelling of multi-component gas flows in capillaries and porous solids. *Int. J. Heat Mass Transfer*, 48(25-26):5338–5353.
- Yu, D. Z., Mei, R. W., and Shyy, W. (2005). Improved treatment of the open boundary in the method of lattice Boltzmann equation. *Prog. Comput. Fluid Dy.*, 5(1-2):3–12.
- Yu, H. and Zhao, K. (2000). Lattice Boltzmann method for compressible flows with high Mach numbers. *Phys. Rev. E*, 61:3867–3870.
- Ziegler, D. P. (1993). Boundary-conditions for lattice Boltzmann simulations. *J. Statist. Phys.*, 71(5-6):1171–1177.
- Zou, Q. S. and He, X. Y. (1997). On pressure and velocity boundary conditions for the lattice Boltzmann BGK model. *Phys. Fluids*, 9(6):1591–1598.